Dissertation

submitted to the
Combined Faculties for the Natural Sciences and for Mathematics
of the Ruperto-Carola University of Heidelberg, Germany
for the degree of
Doctor of Natural Sciences

presented by
Katharina Elisabeth Schneider
born in Darmstadt

Date of oral examination: 13.06.2012

Dynamics in charge transfer and ionization processes

in fast ion-helium collisions

Referees: **Dr. Daniel Fischer**
Prof. Dr. Thomas Stöhlker

Abstract

In the course of this work transfer ionization (TI), radiative electron capture (REC), and single ionization (SI) in fast ion-helium collisions have been studied. For this purpose, two experimental techniques, a 4π coincident ion-electron momentum spectrometer, namely a Reaction Microscope (REMI) and the heavy ion storage ring TSR, providing excellent beam properties, have been combined.
In TI, i.e. the ejection of one plus the capture of a second target electron, the role of electron-electron correlations is of particular interest. In order to unravel different correlated as well as uncorrelated mechanisms, differential data has been recorded for different perturbations (projectile charge to speed ratio). For the first time strong evidence of a recently proposed, correlated TI process was found experimentally.
In a second, pioneering experiment it has been attempted to perform the first kinematically complete measurement on REC. Here, an electron from the target is captured by the projectile simultaneously emitting a photon. In order to observe the emerging photons, a detector covering a large solid angle has been designed and implemented in the REMI. Although three particle coincidences have been recorded between recoil ions, projectile ions, and photons, experimental proof of the acquisition of REC coincidences was prevented due to limited statistics.
Finally, in studies on SI, the influence of the projectile beam coherence properties on the collision dynamics has been investigated. The pronounced differences to earlier data taken with a projectile beam with much smaller coherence length provide evidence for its influence on the ionization dynamics, which is generally neglected in theoretical calculations. These results could pave the way to a final resolution of the long standing question on the origin of the discrepancies between theory and experiment in fully differential cross sections.

Zusammenfassung

Im Rahmen dieser Arbeit wurden Transferionisation (TI), radiativer Elektroneneinfang (REC) und Einfachionisation (SI) in schnellen Ion-Atom Stößen untersucht. Dafür wurde ein Reaktionsmikroskop (REMI) in den Schwerionenspeicherring TSR implementiert, der exzellente Strahleigenschaften aufweist.
In TI, bei der ein Elektron in das Projektilion eingefangen und ein weiteres emittiert wird, ist die Rolle der Elektronenkorrelationen von besonderem Interesse. Um unterschiedliche korrelierte und unkorrelierte Mechanismen trennen zu können, wurden differentielle Daten für unterschiedliche Störungen (Verhältnis von Ladung zu Geschwindigkeit des Projektils) aufgenommen. Ein korrelierter TI-Prozess, der erst kürzlich vorhergesagt wurde, konnte damit experimentell bestätigt werden.

Ein weiteres Experiment hatte zum Ziel, den REC erstmalig kinematisch vollständig zu vermessen. In diesem Mechanismus wird der Einfang eines Elektrons in einen gebundenen Zustand des Projektils durch die Emission eines Photons ermöglicht. Um diese zu beobachten wurde zusätzlich ein Photonendetektor in das Reaktionsmikroskop implementiert. Dadurch konnten Dreifachkoinzidenzen zwischen Rückstoßionen, Projektilionen und Photonen aufgenommen werden, jedoch verhinderten die limitierte Strahlzeit und der hohe Untergrund die eindeutige Zuordnung der Photonen zum REC.
In den Messungen der SI wurde der Einfluss der Kohärenzeigenschaften des Projektilstrahls auf die Stoßdynamik untersucht. Deutliche Unterschiede zu früheren Daten, die mit einem Strahl mit viel kleinerer Kohärenzlänge aufgenommen wurden, weisen deren Einfluss auf die Dynamik des Stoßprozesses nach. In theoretischen Rechnungen wird dieser Einfluss generell vernachlässigt. Diese Ergebnisse sind ein Schritt zur Klärung der Diskrepanzen zwischen Theorie und Experiment in den vollständig differentiellen Wirkungsquerschnitten.

Contents

1 Introduction

The descriptions of the time-independent structure as well as the understanding of the time-dependent dynamics of atomic systems are fundamental goals of atomic physics. In both branches there is one underlying basic problem; neither the stationary nor the time-dependent Schrödinger equation is analytically solvable for more than two mutually interacting particles. For stationary systems, this problem can to a large extent be overcome using iterative methods, like e.g. the MCDF model [FFT12, Jö98]. With sufficient computational supply, wave functions and binding energies can be calculated with high accuracy. Here, the present research concentrates on a highly detailed analysis of atomic and molecular structure, such as QED effects [FIS05, IM91].

For the time-dependent few-body-problem, however, the available theoretical tools are not as successful as for stationary systems. Here, the description cannot be reduced to an effective single-center problem, making the theoretical modelling substantially more complex. Atomic collision experiments are an important tool to test theoretical models and to gain a better understanding of the dynamics of atomic systems.
In the case of electron or photon impact on a target atom, electronic transitions are possible either to other bound states of the target atom (target excitation), or to a continuum state (target ionization). After considerable efforts and with enormous computational power, non-perturbative methods were developed which could model these collision with a excellent accuracy for simple atomic or molecular targets (see e.g. [RBIM99, BFKS02, RBF$^+$11]). However, the description of collisions with ionic projectiles is more complex. On one hand, here a larger variety of processes is possible. If the projectile carries bound electrons, electronic transitions may also occur in the projectile (projectile excitation or ionization). Additionally, electron transfer from the target to the projectile (electron capture) can happen. On the other hand, due to the larger masses of the ions, the numerical methods which obtained good results for electron impact do not necessarily converge for ionic projectiles. Therefore, in many cases perturbative methods, such as the first Born approximation or continuum-distorted-wave calculations, have been employed, which were fairly successful to reproduce many features of the differential experimental data.

Experimentally, the study of ion-atom collisions is a challenging task, too. Due to the high mass, the momentum change of the projectiles can hardly be measured directly. A breakthrough has been achieved with the invention of Reaction Microscopes, which for the first time enabled to obtain fully-differential information on ionizing ion-atom collisions. Here, the momentum change of the projectile is not directly measured but can be obtained due to momentum conservation from the momenta of the collision fragments [DMJ+00, UMD+03].

Within this thesis, such a Reaction Microscope was successfully implemented in an ion storage ring, the TSR at the Max-Planck-Institut für Kernphysik in Heidelberg. In the storage ring, in contrast to single pass experiments, the ions pass the target region repeatedly, and very high luminosities are accessible. Thereby, it is possible to obtain good statistics in a reasonably short measuring time, even for processes with a small cross section like e.g. electron capture and transfer ionization. Furthermore, electron cooling in the storage ring drastically reduces the size of the stored ion beam and its momentum spread [BBF+88, SBB+90]. As a small momentum spread directly corresponds to a large coherence length of the projectiles, beams with a coherence length well above the typical size of an atom can be prepared in the TSR. Hence, the prepared ion beam is an excellent projectile beam for the investigation of ion-atom collisions. Three target-ionizing processes are studied in this work, transfer ionization, electron capture and single ionization.

The transfer ionization process (TI), where one target electron is captured and a second is emitted into the continuum, is of special interest because electron-electron correlation effects can play an important role in the collision dynamics, depending on the collision system. Its effect is negligible for high projectile charge and low velocities. In faster collisions, on the other hand, correlated processes dominate the transfer ionization. The earlier observation of electrons emitted in the backward direction [MDK+01] resulted in a long discussion on the nature of the electron-electron correlations, where especially the small non-s^2 contribution in the ground-state wave function was considered as a possible explanation [SBMD+03]. However, another plausible interpretation was suggested by Voitkiv et al. [Voi08, VNU08], who proposed a correlated process which has completely been overlooked before. Here, the excess energy of the captured electron is transferred to a second target electron, which is thus emitted backwards. Within this thesis, we investigated transfer ionization processes in different collision systems in order to obtain three dimensional angular distributions of electron emission in non-correlated as well as correlated transfer ionization processes and were able to provide experimental evidence for the newly proposed process.

In the radiative electron capture (REC), the electron couples to the electromagnetic field and a photon is emitted. Especially for capture into heavy ions, REC has been studied intensively (e.g. [SKM+95, SML+01]). The angular distribution of the emitted photons (e.g. [SLB+99]) as well as their polarization (see [SBF+04, SSB+07]) have been investigated before.
However, until now there is no kinematically complete data on REC. The photons are in most cases measured in coincidence with charge-changed projectiles, but the collision kinematics has never been recorded. With an additional photon detector implemented in the Reaction Microscope, we attempt to obtain for the first time triple coincidences of photons, recoil ions and projectile ions, and thereby measure kinematically complete data on electron capture.

The first kinematically complete data on target ionization processes were obtained when the invention of the Reaction Microscope permitted for the first time the detection of fully momentum-analysed recoiling target ions. Surprisingly, severe qualitative discrepancies between the data and the calculations were observed in the fully differential cross sections, even for relatively simple collision systems as 100 MeV/u C^{6+} impact on helium (see e.g. [SMF+03]).
The cause of these discrepancies has remained a puzzle for almost a decade, and several explanations were discussed, e.g. the experimental resolution [FOO06], which could be ruled out by Dürr et al. [DNS+07], or the dynamic screening of the target nuclear charge, which might not be described with sufficient accuracy [FPS+06]. It was even more surprising that the classical treatment of the nuclear-nuclear interaction turned out to provide a major improvement in the agreement with experiment [SDN+07]. A key to resolving this puzzle was provided by experimental studies of Egodapitiya et al. [ESH+11]. They showed that the finite transverse coherence length of a projectile ion beam has an effect on the double differential cross section of the ionization of a H_2 molecule, i.e. that the cross sections for coherent and incoherent beams differ. This observation suggests that also in ion-atom collisions the coherence length might affect the cross sections, and that the assumption of an infinite coherence length in quantum mechanical calculation might be an explanation for the disagreement with experimental data. In this work, we studied single ionization processes of an atomic target in the collisions of a coherent projectile beam and, in comparison to earlier data with an incoherent beam, investigated the effect of the transverse coherence length on the fully differential cross sections.

This thesis starts with an overview over ion-atom collisions in chapter 2, where the different collision processes are introduced. The experimental setup is described in chapter 3. Chapter 4 gives a short introduction to the theory of ion-atom collisions and introduces the theoretical approaches which found entrance into this work. The next three chapters (5-7) present the experimental data, and a conclusion and outlook is given in chapter 8.

2 Ion-atom collisions

2.1 Introduction

There are far more fragmentation channels available for atomic collisions with ions than compared to collisions with electrons or photons. In ion collisions, not only is it possible to excite or ionize the target atom, it is also possible to transfer a target electron to the projectile ion. Also, if the projectile ion carries one or more electrons then it too can undergo excitation or ionization during the collision with the target atom.
These basic processes can occur simultaneously in a single collision, leading to processes involving more than one active electron, e.g. double ionization of the target atom or mutual projectile and target ionization (e.g. [WSK$^+$11]). In a transfer ionization process, one target electron is captured by the projectile ion with the simultaneous emission of a second target electron. In a two-electron transition, the electrons can either act independently or be correlated in some way.
The relative importance of each process depends strongly on the collision system, i.e. on the target atom and on the charge state Z_P and velocity v_P of the incident projectile ion. In a 'soft' collision, the momentum transfer from the projectile ion to the target is small compared to its total momentum, and little energy is transferred (typically in the order of the binding energy of the active electron(s)). A collision is considered 'fast' if the projectile velocity exceeds the orbiting velocity of the bound target electron.
The influence of the projectiles Coulomb field on the target system increases with decreasing velocity and increasing charge state of the projectile ion. Therefore, an important parameter of the collision is the charge state to velocity ratio, the so called perturbation parameter $\eta = Z_P/v_P$. The strength of the perturbation determines the theoretical model in which the collision system can best be accessed (figure 2.1). For small perturbations, i.e. small projectile charges and high velocities, the first Born approximation can be applied. As the Born series does not converge for higher perturbations, a better model in that regime is the continuum distorted wave (CDW) calculation, which corresponds to an expansion in a parameter $\eta' = Z_P/v_P^2$ [CM83]. At projectile velocities much lower than the orbital velocity of the target electron, the system forms a transient molecular state, and an molecular orbital (MO) model can be used.

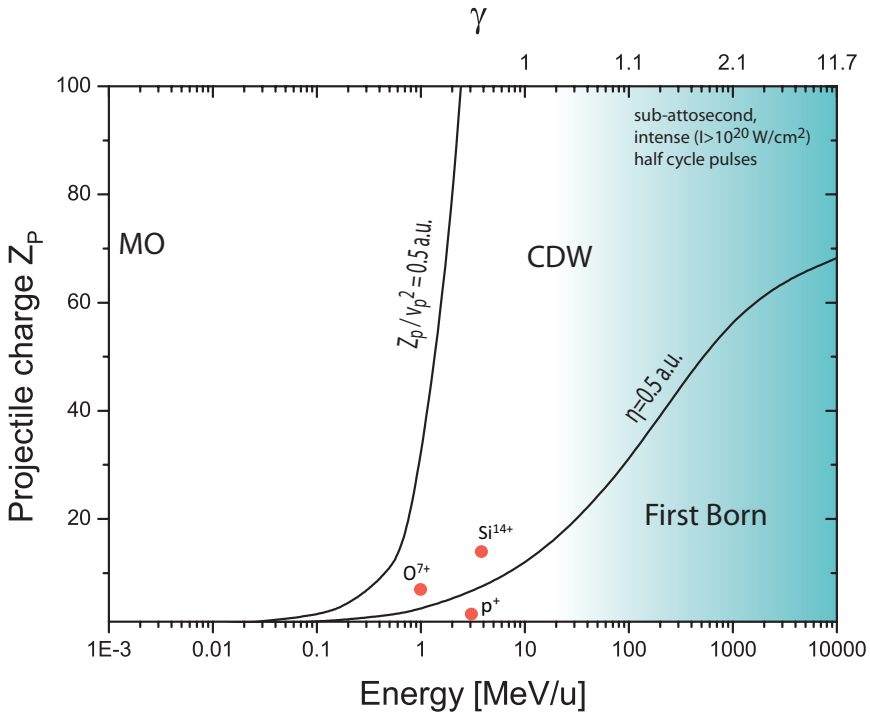

Figure 2.1: The charge state and the energy of the projectile ion determine the perturbation $\eta = Z_P/v_P$. For small perturbations, the system can be accessed in the first Born approximation. Larger perturbations require the consideration of the distortion effect in the initial and final state, which is included in the continuum distorted wave (CDW) calculations. At very low projectile velocities, the two nuclei form a quasi-molecular state, and molecular-orbital (MO) models are applied. The bluish shade indicates the importance of relativistic corrections.

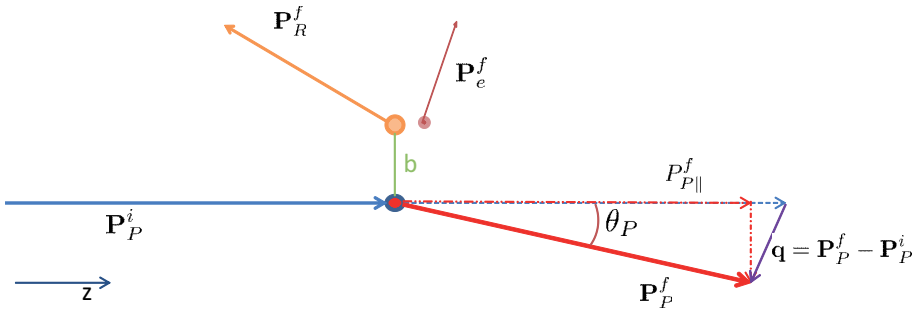

Figure 2.2: A schematic drawing of a fragmentation process in an ion-atom collision. In the target frame, the projectile ion initially moves with momentum $\mathbf{P}_P^i$. In the collision, the recoil ion and the electron gain momenta $\mathbf{P}_R^f$ and $\mathbf{P}_e^f$, respectively. The momentum transfer is $\mathbf{q} = \mathbf{P}_P^i - \mathbf{P}_P^f$, where $\mathbf{P}_P^f$ is the momentum of the projectile ion in the final state.

In the collision systems observed in this work, the perturbation parameter ranges from $\eta = 0.5 - 1.2$ and the validity of the first Born and the CDW calculation was tested for several reaction channels in detail.

Some notations

Generally speaking, a projectile ion X^{Z_P+} of charge state Z_P collides with a neutral atom A. If n_T is the number of ionized target electrons, n_P the number of ionized projectile atoms, and n_C the number of target electrons captured by the projectile ion, the reaction equation of the collision is given by

$$X^{Z_P+} + A \rightarrow X^{(Z_P+n_P-n_C)+} + A^{(n_T+n_C)+} + (n_P + n_T)e^- . \tag{2.1}$$

In this thesis, the collisions are in most cases considered in the rest frame of the target atom, i.e. the frame in which the target atom has zero initial momentum. A schematic drawing of the collision kinematics in that frame is shown in figure 2.2. The superscripts i and f in figure 2.2 and elsewhere label the initial and final states, respectively, whereas the collision fragments are denoted by the subscripts: P for projectile ion, R and e for the recoil ion and emitted electrons, respectively. The projectile ion of charge state Z_P moves with velocity $\mathbf{v}_P$ and momentum $\mathbf{P}_P^i$ in the target frame. The initial direction of projectile propagation defines the z-axis. The impact parameter b is the minimum distance between the projectile ion and the target nucleus along its trajectory. In the final state, the momentum vector of the projectile ion is $\mathbf{P}_P^f$, and the

momentum transfer is given by

$$\mathbf{q} = \mathbf{P}_P^i - \mathbf{P}_P^f \ . \tag{2.2}$$

The vectors $\mathbf{P}_P^i$ and $\mathbf{q}$ define the projectile scattering plane.
Due to the cylindrical symmetry of the collision system, the momentum vector of the collision fragments can be split into the longitudinal component parallel to the z-axis, $P_\parallel^f$, and the vertical component $\mathbf{P}_\perp^f$. Throughout this work, atomic units are used unless otherwise stated.

2.2 The kinematics of ion-atom collisions

2.2.1 Momentum conservation

Due to momentum conservation, the sum of momenta in the final state has to be equal to the sum of momenta in the initial state. The momentum balance reads

$$\mathbf{P}_P^i + \mathbf{P}_T^i = \mathbf{P}_P^f + \mathbf{P}_T^f + \sum_{j=1}^{n_P+n_T} \mathbf{P}_{e\,j}^f \ , \tag{2.3}$$

where $n_P + n_T$ is the number of projectile and target electrons emitted into the continuum.
In the target frame, the initial projectile momentum is only non-zero in the z-direction, $\mathbf{P}_P^i = (P_{P\parallel}^i, 0, 0)$, and the target atom is at rest,[1] i.e. $\mathbf{P}_T^i = 0$. The transversal momentum balance is

$$0 = \mathbf{P}_{P\perp}^f + \mathbf{P}_{R\perp}^f + \sum_{j=1}^{n_P+n_T} \mathbf{P}_{ej\perp}^f \ , \tag{2.4}$$

which can be transformed to

$$\mathbf{P}_{R\perp}^f = \mathbf{q}_\perp - \sum_{j=1}^{n_P+n_T} \mathbf{P}_{ej\perp}^f \ , \tag{2.5}$$

where $\mathbf{q}_\perp$ is the momentum transfer perpendicular to the initial direction of the projectile ion.

Momentum conservation in the longitudinal direction gives

$$P_{P\parallel}^i = P_{P\parallel}^f + P_{R\parallel}^f + \sum_{j=1}^{n_P+n_T} P_{ej\parallel}^f \tag{2.6}$$

[1] Due to the velocity of the atoms in the gas jet, they actually have a momentum in the laboratory frame. This is only resulting in a constant offset in the measured data which can be subtracted [US03].

and thereby

$$P^f_{R\|} = q_\| - \sum_{j=1}^{n_P+n_T} P^f_{ej\|}. \tag{2.7}$$

The longitudinal momentum change of the projectile ion is balanced by the longitudinal momenta of recoil ion and electrons in the final state.

2.2.2 Energy conservation

The energy conservation in ion-atom collisions reads

$$E^i_P + E^i_R + E^i_{bind} = E^f_P + E^f_R + E^f_{bind} + \sum_{j=1}^{N} E^f_{ej} \ . \tag{2.8}$$

The initial momentum E^i_R of the recoil ion is zero in the target frame, which gives

$$E^i_P = E^f_P + E^f_R + Q + \sum_{j=1}^{N} E^f_{ej} \ , \tag{2.9}$$

where the Q-value of the collision is the difference of binding energies in the initial and final state,

$$Q = E^f_{bind} - E^i_{bind} \ . \tag{2.10}$$

2.2.3 Fast collisions

High projectile velocities and soft collisions, where the initial kinetic energy of the projectile is much larger than the energy transfer to the target recoil ion,[2] allow for some simplifications. In the following, a non-relativistic regime is considered, i.e. the Lorentz factor

$$\gamma = \left(\sqrt{1 - \frac{v^{i2}_P}{c^2}} \right)^{-1} \tag{2.11}$$

does not significantly deviate from unity. The classical treatment is justified in the collision systems observed in this work, where $\gamma < 1.1$ (see figure 2.1).

[2] For example, a projectile ion with an energy of 1 MeV/u has a velocity of 6.3 a.u.. The momentum of a $^{12}C^{6+}$ ion with that velocity is about 139000 a.u.. This initial momentum of the projectile ion is by several orders of magnitude larger than the momentum transfer to the recoil ion, which is in the order of a few a.u..

The initial kinetic energy E_P^i of the projectile ion can be expressed by $\frac{P_P^{i2}}{2M_P}$, where M_P is the mass of the projectile ion in the initial state. If the projectile energy in the final state is expressed by $\frac{P_P^{f2}}{2M_P}$, the change in projectile mass during electron capture or loss has to be accounted for in a separate term in equation 2.8, which can be transformed to

$$\frac{P_P^{i2}}{2M_P} + E_{bind}^i = \frac{P_P^{f2}}{2M_P} + \frac{v_P^2}{2}(n_C - n_P) + E_{bind}^f + E_R^f + \sum_{j=1}^{n_P+n_T} E_{ej}^f \ . \tag{2.12}$$

The energy transfer to the target ion is typically $E_R^f \ll 1\,\mathrm{eV}$, which is negligible compared to the energies of fast projectile ions, and also compared to a typical energy transfer to the active electrons. This results in

$$\frac{P_P^{i2} - P_P^{f2}}{2M_P} = Q + \frac{v_P^2}{2}(n_C - n_P) + \sum_{j=1}^{n_P+n_T} E_{ej}^f \ . \tag{2.13}$$

The left side of the equation can be approximated by

$$\frac{P_P^{i2} - P_P^{f2}}{2M_P} = \frac{(\mathbf{P}_P^i + \mathbf{P}_P^f)\cdot(\mathbf{P}_P^i - \mathbf{P}_P^f)}{2M_P} \approx \frac{(2\mathbf{P}_P^i)(\Delta\mathbf{P}_P)}{2M_P} = \Delta\mathbf{P}_P \cdot \mathbf{v}_P \tag{2.14}$$

with $\Delta\mathbf{P}_P = \mathbf{P}_P^i - \mathbf{P}_P^f$. It is assumed that the momentum change is negligible compared to the sum $\mathbf{P}_P^i + \mathbf{P}_P^f$. As v_P only has a non-zero component in the longitudinal direction, the scalar product gives $\Delta\mathbf{P}_P \cdot \mathbf{v}_P = \Delta P_{P\|} v_P$, and equation 2.13 can be transformed to

$$\Delta P_{P\|} = \frac{Q}{v_P} + \frac{v_P}{2}(n_C - n_P) + \sum_{j=1}^{n_P+n_T} \frac{E_{ej}^f}{v_P}. \tag{2.15}$$

The longitudinal momentum conservation formula reads

$$\Delta P_{P\|} = P_{R\|}^f + \sum_{j=1}^{n_P+n_T} P_{ej\|}^f + v_P(n_C - n_P) \ , \tag{2.16}$$

where the momentum change of the electrons captured or lost by the projectile is not included in $\Delta P_{P\|}$ and therefore contributes in a separate term. The combination of equations (2.15) and

(2.16) gives:

$$P^f_{R\parallel} = \frac{Q}{v_P} + \underbrace{\frac{v_P}{2}(n_P - n_C)}_{\text{mass transfer term}} + \sum_{j=1}^{n_P+n_T}\left(\frac{E^f_{ej}}{v_P} - P^f_{ej\parallel}\right) \tag{2.17}$$

For small relative momentum transfers, i.e. small scattering angles, one has $P^f_{P\perp} \ll P^f_{P\parallel}$ and $\theta_P \approx \frac{P^f_{P\perp}}{P^f_{P\parallel}}$. With

$$P^f_{P\perp} \approx P^f_{P\parallel}\theta_P \approx M_P v_P \theta_P, \tag{2.18}$$

momentum conservation results in the transversal momentum of the recoil ion

$$P^f_{R\perp} = -P^f_{P\perp} - \sum_{j=1}^{N} P^f_{ej\perp} \approx -M_P v_P \theta_P - \sum_{j=1}^{N} P^f_{ej\perp}\ . \tag{2.19}$$

It can be seen that different informations are contained in the transverse and the longitudinal momentum of the recoil ion. The Q-value of the reaction appears only in the longitudinal momentum balance. Therefore, spectroscopic information can be obtained from the measurement of the longitudinal recoil ion momentum. The transversal momentum of the recoil ion contains information on the scattering angle θ_P, the dynamics, and also the impact parameter of the reaction.

2.3 Target ionization

The Coulomb interaction of the projectile ion with a target electron may lead to the emission of the electron to the continuum. The single ionization (SI) process is one of the most fundamental few body processes in atomic physics and has been studied in great detail. The double ionization (DI) process has also received a lot of attention, particularly in the light of electron-electron correlation effects [FMS$^+$03, FO04].

Most electrons emitted in an ionization process can be assigned to the 'target cusp', i.e. they have a low energy and longitudinal momentum in the final state [SMK$^+$99]. A much smaller number of electrons contributes to the 'projectile cusp'. These electrons move with a velocity close to the projectile velocity, but are not captured into a bound state. Generally even less electrons are emitted with a velocity of roughly half of the projectile velocity. These so called 'saddle-point' electrons are pulled from the target nucleus by the projectile ion, but then left in

the saddle region of the Coulomb fields of both nuclei [OGB+87, WO96].
The reaction equation for a target ionization process reads

$$X^{Z_P+} + A \rightarrow X^{Z_P+} + A^{n_T+} + n_T e^-, \tag{2.20}$$

where n_T is the number of ionized target electrons. With $n_P = n_C = 0$, momentum conservation gives

$$P^f_{R\parallel} = \frac{Q}{v_P} + \sum_{j=1}^{n_T} \left(\frac{E^f_{ej}}{v_P} - P^f_{e\parallel j} \right) = \sum_{j=1}^{n_T} \left(\frac{(E^f_{ej} - E_{I\,j})}{v_P} - P^f_{e\parallel j} \right) , \tag{2.21}$$

where E_I is the positive ionization potential of the electron.[3] For small binding energies and small kinetic energies of the electrons and for large projectile velocities, equation (2.21) simplifies to

$$P^f_{R\parallel} = - \sum_{j=1}^{n_T} P^f_{e\parallel j} \ . \tag{2.22}$$

The longitudinal momentum of the recoil ion reflects the sum of all longitudinal momenta transferred to the ionized electrons. Therefore, detailed information on the dynamics of ionization collisions can be obtained without a coincident measurement of all electrons [HLC98]. For fast and highly charged ion collisions that result was confirmed experimentally [MUU+94, UMU+95, MUU+96].
The three dimensional angular distribution of the ejected electrons forms a characteristics double lobe structure (figure 2.3). The electrons which interact with the projectile ion in a binary collision are ejected in the direction of the momentum transfer **q** and contribute to the so called 'binary peak'. Electrons which scatter off the target nucleus in a second interaction contribute to the so called 'recoil peak' in the direction opposite to **q**. The lobe structure is observed for ion [SMM+01] as well as for electron (in the so called (e,2e) experiments) projectiles [CMD94, LB02, MCH72]. In photoionization processes, the binary peak and the recoil peak are perfectly symmetric. In ion-atom collisions, that symmetry is approached for very small perturbations $\eta \rightarrow 0$. With increasing perturbations, the relative contribution of the binary peak increases, i.e. the forward emission of the electrons is strongly enhanced. A review of single ionization measurements can be found in [SDR10]. After the invention of the Reaction Microscope, the first experimental fully differential cross sections on single ionization [SMM+01, SMF+03] and double ionization [FMD+03] were obtained. Even though the single

[3] In the case of one or more additionally excited target electrons, the excitation energy has to be included in Q.

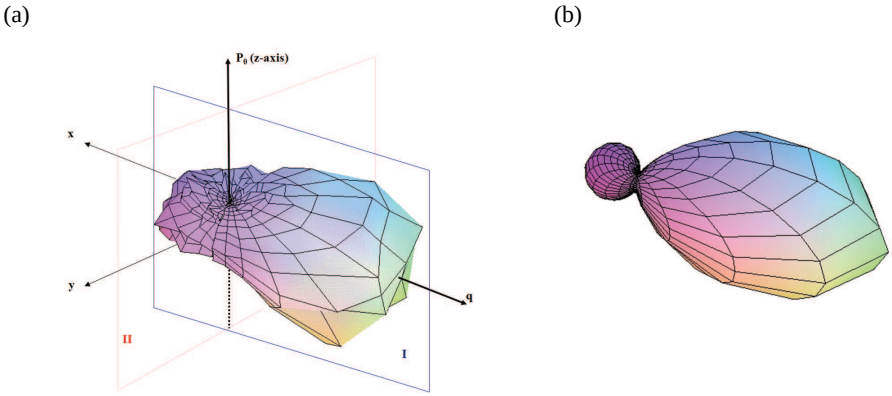

Figure 2.3: (a) The three dimensional distribution of electron emission angles measured in single ionization of a helium target in 100 MeV/u C^{6+} ion collisions. A double lobe structure is visible. The data is fully differential, $d^3\sigma/dE_e d\Omega_e dq$, and here $E_e = 6.5$ eV and $q = 0.75$ a.u.. (b) The angular distribution calculated fully quantum-mechanically (3DW). In the plane perpendicular to **q** (II), there are severe discrepancies between theory and experiment. From [SMF+03].

ionization process was believed to be theoretically well understood, discrepancies were found between the experimental cross sections and the predictions made by theory, especially at high perturbations [SMF+03, SFF+07] (see figure 2.3(b)).
At low perturbations, the ionization cross sections can be calculated in the first Born approximation. In that regime, very good agreement with experimental cross sections has been observed (see e.g. [MSJ+02]). However, at high projectile velocities v_P and charge states $Z_P \gtrsim v_P$, the Born approximation is invalid. For these conditions, Voitkiv and Koval [VK98] calculated the cross section for Single Ionization of hydrogen and helium targets to be

$$\sigma_{SI} = 12.289 \frac{Z_P^2}{v_P^2}\left[\ln\left(\frac{1.2v_P^2}{Z_P}\gamma\right) - \frac{v_P^2}{2c^2}\right], \tag{2.23}$$

where c is the speed of light and $\gamma = (1 - v^2/c^2)^{-1/2}$.

2.4 Single electron capture

In slow collisions, i.e. when the projectile velocity is smaller than the speed of the target electron, the electron capture cross section can be greater than the target ionization cross section [CDF+96]. The final state of the single electron capture process is rather simple, as there are no electrons in the continuum. Therefore, the process is a good test for theoretical models.
The understanding of single electron capture is important in many experimental fields, e.g.

in the investigation of fusion plasmas [VMS+91, WAW+93, Isl94], the development of x-ray lasers [Mat95], and also in astrophysics [Kal95]. Electron capture is also of large interest for the design of accelerators and storage rings, because the capture of electrons from the residual gas atoms is a major limitation factor of the lifetime of stored ion beams. A general scaling rule for the total cross section of electron capture processes by fast, highly charged projectiles was found empirically by Schlachter [SSG+83], and is given by

$$\sigma_C = 1.1 \cdot 10^{-8} \frac{Z_P^{3.9} Z_2^{4.2}}{E_P^{4.8}} \ , \tag{2.24}$$

where Z_2 is the atomic number of the target atom and E_P is the projectile energy in keV per nucleon.
There are different mechanisms leading to the capture of a target electron by the projectile ion. They are usually categorized into radiative electron capture (REC) or non-radiative electron capture (NRC) processes. These mechanisms will be described in the following sections.

2.4.1 Non-radiative capture

A non-radiative capture (NRC) process can be expressed by

$$X^{Z_P+} + A \rightarrow X^{(Z_P-1)+} + A^+ \ .$$

The active electron is initially bound to the target, and finally to the projectile ion. With $n_C = 1$ and $n_P = n_T = 0$ the longitudinal momentum balance is given by

$$P_{R\|}^f = \frac{Q}{v_P} - \frac{v_P}{2} \ , \tag{2.25}$$

i.e. the recoil longitudinal momentum corresponds directly to the Q-value of the reaction. Capture into different states of the projectile ion can be identified by measuring $P_{R\|}^f$. Capture into excited states leads to a characteristic photon emission during decay. Therefore, the electron capture process is a useful tool for spectroscopic investigations of highly charged ions (State selective measurements can be found in e.g. [MWW+97, KADJ95, CDF+96, ACK+97]).

Kinematic capture

Generally speaking, electron capture by the projectile is most likely to occur when the velocity of the electron matches the projectile velocity v_P. Oppenheimer, Brinkman, and Kramers [Opp28, BK30] described the kinematic capture (KC) process quantum-mechanically in an

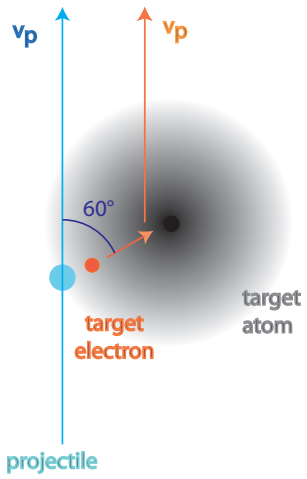

Figure 2.4: The Thomas Capture process in the target frame. The electron is first scattered by the projectile at an angle of 60° and obtains the speed v_P. In a second step it scatters on the target nucleus and is finally moving into the same direction as the projectile ion and is easily captured.

perturbative first order approach corresponding to the first Born approximation. The transition amplitude for kinematic capture has a significant amplitude only if the Compton profiles of the initial and final state overlap.[4] With higher projectile velocity, the overlap between the Compton profiles decreases. This behaviour corresponds to a strong v_P-dependence of the cross section of KC [Opp28, BK30],

$$\sigma_{KC} \propto \frac{Z_T^5 Z_P^5}{v^{12}} \,. \tag{2.26}$$

In the kinematic region of low to intermediate projectile velocities, kinematic capture is the dominant capture channel. At asymptotically high projectile velocities, the electron capture cross section is dominated by a second order process, the so called Thomas capture.

Thomas capture

The Thomas capture process (NET for Nucleus-Electron-Thomas) was first proposed 1927 by Thomas [Tho27] in a classical two-step model. In a collision with the projectile ion, an target electron is accelerated to the projectile speed. In a subsequent collision with the target nucleus, the direction of its propagation is changed, and the electron finally moves parallel to the projectile ion and can easily be captured (see e.g. [SS79]). The momentum transfer in each

[4] The final state profile is the Compton profile of a projectile bound state, shifted by the projectile velocity.

step is well defined, and the NET capture results in a projectile scattering angle of

$$\theta_P = \frac{\sqrt{3}}{2M_P} \ . \tag{2.27}$$

In experiment, the conditions are softened by the Compton profile of the electron, and by the initial momenta of electron and target ion. The signature of the NET capture process can be observed in differential measurements in the projectile scattering angle distribution (see [HPCS83] and also [VSJ+86, FSC+06]).

In quantum mechanical calculations, the NET capture first appears in second order perturbation theory [Dri55], and its cross section is given by [BT79]

$$\sigma_{NET} = \frac{2^7 \pi^2 Z_P^5 Z_{T_E}^5}{Z_P + Z_{T_E}} v^{-11} \ , \tag{2.28}$$

where Z_{T_E} is the effective charge of the target nucleus. This v_P-scaling differs from KC, which features a v_P^{-12}-dependence. NET thereby has more relative importance at higher velocities, whereas it can be neglected at lower energies.

2.4.2 Radiative electron capture

Radiative electron capture (REC) describes the capture of a target electron into a bound state of the projectile ion via the emission of a photon. If the electron is considered initially quasi-free, REC is the time inverse of a photoionization process [HWS+72, SKM+95]. The reaction equation is given by

$$X^{Z_P+} + A \rightarrow X^{(Z_P-1)+} + A^+ + \gamma \ .$$

The REC process can best be understood in the rest frame of the projectile ion, where the electron moves with a speed v_P. In order to be captured by the projectile, the electron has to dispose of its kinetic energy $\frac{1}{2}v_P^2$. By a coupling to the electromagnetic field, a photon is emitted with the energy

$$\hbar\omega = \frac{1}{2}v_P^2 + \epsilon_b \ , \tag{2.29}$$

where ϵ_b is the binding energy of the electron in the final state. The cross section of REC can be obtained over the cross section of the photoelectric effect (see [Sto30]), the cross section of

radiative capture into an empty K-shell is given by [EM95]

$$\sigma_{REC} = \frac{2^8\pi^2\alpha}{3}\lambda\!\!\!^{-2}_c\left(\frac{\nu^3}{1+\nu^2}\right)^2 \frac{e^{-4\nu\arctan 1/\nu}}{1-e^{-2\pi\nu}} \ , \tag{2.30}$$

where $\lambda\!\!\!^{-}_c = \hbar/m_e c$ is the electrons Compton wavelength and $\nu = Z_P e^2/\hbar v_P$ the Sommerfeld parameter. The v_P-dependence of REC is weak compared to kinematic or NET capture. Therefore, REC is the dominating electron capture process at very high projectile velocities [ES07].

In the non-relativistic limit, the photons are emitted preferentially perpendicular to the projectile beam direction [SML+01],

$$\frac{d\sigma_{REC}}{d\theta_\gamma} \propto \sin^2\theta_\gamma \ , \tag{2.31}$$

where θ_γ is the photon emission angle relative to the beam direction. This distribution does not change significantly for projectile energies less than 1 Gev/u [EM95].

2.4.3 More exotic capture processes

A variety of more exotic capture processes exists, which generally have a small cross section but are nevertheless discussed in the literature. One of these process is the resonant electron transfer with simultaneous projectile excitation (RTE), which is rather similar to the REC process. In the RTE, the excess energy in not transferred to a photon, but to an electron bound by the projectile. The electron is resonantly lifted to an excited state of the projectile. Experiments on RTE were performed by e.g. [MMB+03] and [EST09], a theoretical approach can be found in [GH92]. Also, electron capture with the simultaneous excitation of one or more target electrons may occur, see e.g. [STJN09].

In multiple electron capture processes, more than one target electron is transferred to the projectile ion. Different multiple capture channels are possible, e.g. two electrons might be captured kinematically, or via the emission of a single photon (which is labelled REEC, see [SWET10]). At very high projectile velocities, the bound-free pair production becomes possible, where an electron-positron pair is produced of which the electron is created in a bound state of the projectile ion.

It is also possible that an electron is captured into a continuum state of the projectile ion. This process is labelled ECC (Electron Capture to the Continuum) [RWL95]. The electron is free, but moves with the discrete projectile velocity v_P.

Due to their small cross sections, theses exotic processes will not be discussed here in further detail.

2.5 Transfer ionization

The transfer ionization (TI) process denotes the capture of one target electron to the projectile ion with simultaneous emission of a second target electron. The reaction equation is given by

$$X^{Z_P+} + A \rightarrow X^{(Z_P-1)+} + A^{2+} + e^- \ .$$

With $n_C = n_T = 1$ and $n_P = 0$, the longitudinal momentum balance (see equation 2.17) is given by

$$P^f_{R\parallel} = \frac{Q}{v_P} - \frac{v_P}{2} + \frac{E^f_e}{v_P} - P^f_{e\parallel} \ . \tag{2.32}$$

The TI process bears a high resemblance to the single ionization process, because in the final state there is only one electron in the continuum. There are different mechanisms leading to the transfer ionization of the target atom. In the independent process, the projectile ion captures one target electron and ionizes another target electron in two subsequent, independent interactions. In the correlated processes, only one interaction of the projectile ion with the target system occurs, and the TI is enabled by an electronic correlation.

2.5.1 Independent transfer ionization

As mentioned above, the independent transfer ionization process is the result of two subsequent, independent interactions between the projectile ion and the target system, where one target electron is captured and the other ionized.
Generally speaking, the capture process requires a closer collision (i.e. a smaller impact parameter) than an ionization process. Also the TI processes requires closer collisions, because a capture event is included, which results in larger scattering angles of the projectile ion in TI processes compared to SI.
At low projectile velocities, the interaction time $t_{int} \propto 1/v_P$ is long and the projectile is more likely to interact twice. The probability that two separate interactions will occur in a single collision decreases with increasing projectile velocity. At high velocities, the relative importance of the correlated TI processes, where only one interaction between projectile and target system is required, grows.

2.5.2 Correlated transfer ionization

In the correlated TI processes, the transfer of a target electron to the projectile ion is enabled by the ejection of a second target electron. The cross section of the correlated TI processes does not decrease as rapidly with increasing v_P as that of the independent TI process, and the correlated processes are of a higher relative importance at high projectile velocities.
To gain a better understanding of the correlated TI mechanisms, energy conservation is considered in the projectile frame. In the initial state, the projectile ion is at rest and the target atom moves with velocity v_P. The kinetic energy of each active target electron, $E^i_{e1,2}$, is $\frac{v_P^2}{2}$, and the kinetic energy of the target core is $E^i_T = \frac{M_T v_P^2}{2}$. In the final state, the captured electron has no kinetic energy in the projectile frame, and energy conservation gives

$$\frac{v_P^2}{2} + \frac{v_P^2}{2} + \frac{M_T v_P^2}{2} + E^i_{bind} = \frac{v_e^{f2}}{2} + \frac{M_T v_T^{f2}}{2} + E^f_{bind} \ , \tag{2.33}$$

where v_e^f and v_T^f are the final state velocities of the ejected electron and the recoil ion, respectively. In correlated TI processes, the recoil ion can be considered merely as a bystander, and its energy change is negligible. If also the change of binding energy is neglected,[5] equation (2.33) gives

$$v_e^f \approx \sqrt{2} v_P \tag{2.34}$$

in the projectile frame. The direction of the ejected electron is a signature of the different correlated TI mechanisms, which are introduced on the following pages.

Electron-electron transfer ionization

Only recently, a correlated transfer ionization process has been proposed by Voitkiv et al. [VNU08, Voi08], which had been overlooked during decades of research. This electron-electron transfer ionization (eeTI) process bears a close resemblance to REC, and like REC it can most easily be understood in the rest frame of the projectile ion.
In that frame, the target electron has a kinetic energy of $\frac{v_P^2}{2}$ in the initial state. When the electron is captured by the projectile, it transfers its kinetic energy to a second target electron. The kinetic energy of the second target electron after the transfer is equal to v_P^2, and it moves with the velocity $v_e^f = \sqrt{2} v_P$ in the direction of the target atom propagation. In the target frame, this

[5] Especially at high projectile velocities, and when the electron is captured into higher shells, the change of binding energy is small compared to the change of kinetic energy of the electron.

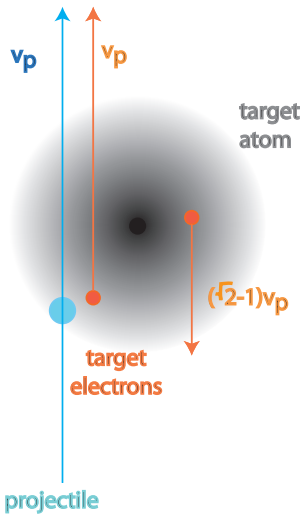

Figure 2.5: The electron-electron transfer ionization in the target frame. In order to be captured, a target electron transfers its kinetic energy to a second target electron. That electron is thereby emitted in the direction opposite to the projectile beam with a velocity of $(\sqrt{2}-1)v_P$.

results in a velocity of

$$v_e^f = (\sqrt{2}-1)v_P \ . \tag{2.35}$$

The electron emission is directed backwards, i.e. opposite to the projectile beam direction (see figure 2.5).
For high projectile velocities $v_P \gg Z_P, Z_T$, the cross section for eeTI is given by Voitkiv [VNU08] to be

$$\sigma_{eeTI} \propto \frac{Z_P^5 Z_T^3}{v_P^{12}}. \tag{2.36}$$

In the eeTI process, the target nucleus is mostly a spectator. Nevertheless, it receives a fraction of the energy transfer. The fraction is small compared to the energy of the ejected target electron in the final state, even though it increases with Z_T.

Thomas transfer ionization

The electron-electron Thomas transfer ionization process (also labelled EET for electron-electron Thomas) is closely related to the Thomas Capture process described in section 2.4.1. Also the Thomas TI process is a two-step process. An interaction with the projectile ion accelerates a

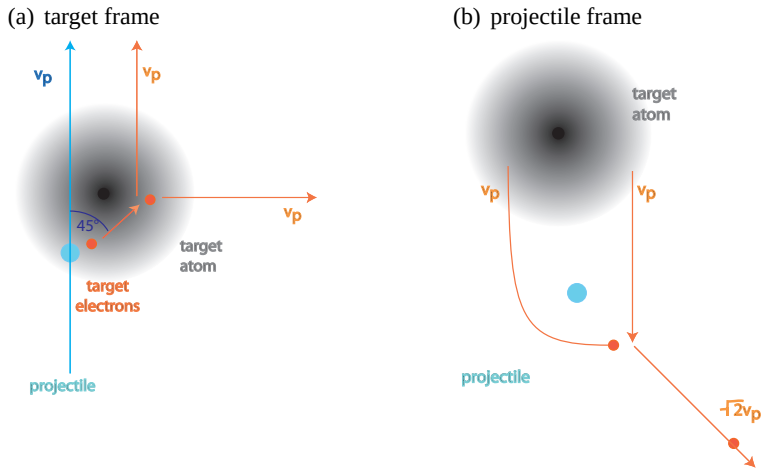

Figure 2.6: (a) The Thomas transfer ionization process in the target frame. Due to the interaction with the projectile ion, a target electron is accelerated to the speed $\sqrt{2}v_P$ at an angle of 45° relative to the projectile direction. In a second step, it is scattered by a second target electron. In the final state, the two electrons each move with a speed v_P. One electron moves in beam direction and is easily captured, the second electron is emitted perpendicular to the projectile beam direction. (b) The picture on the right displays the Thomas TI process in the projectile frame. In the final state, the captured electron is stopped in the projectile rest frame and the emitted electron moves with speed $\sqrt{2}v_P$.

target electron to a speed of $\sqrt{2}v_P$. The electron is scattered in a collision with a second target electron, and moves parallel to the projectile ion in the final state, where it is easily captured. The second electron emerges from the collision with the same speed v_P as the first electron, but in the direction perpendicular to the projectile beam (see figure 2.6(a)).

The kinematics of the Thomas TI process determine the scattering angle of the projectile ion, e.g. a proton is scattered in an angle of 0.54 mrad, independent of its velocity v_P.[6]
The Thomas TI can also be considered in the rest frame of the projectile ion. Here, the first target electron is stopped in the collision with the second electron, which is ejected with a speed of $v_e^f = \sqrt{2}v_P$ at an angle of 45° relative to the target motion in the projectile frame (see figure 2.6(b)). In quantum-mechanical calculations, the Thomas TI process appears in second order perturbation theory. The theoretical cross section in the second Born approximation was calculated by [BT79] to be

$$\sigma_{EET} = \frac{2^7\pi^2 Z_P^5 Z_T^3}{Z_P + \sqrt{2}Z_T} v_P^{-11} \text{ a.u. } . \tag{2.37}$$

[6] Except from being shifted, the shape of the projectile scattering angle distribution is essentially identical to the shape of the distribution measured in kinematic capture processes [GSM+09].

The v_P-dependence of the Thomas transfer ionization cross section could be confirmed experimentally, see e.g. [SFS+02].

There are clear differences between the final momenta of the electrons ejected in Thomas TI and eeTI processes. The Thomas TI process results in an emission directed transversal to the projectile beam. In contrast, the eeTI process emits the electron with a minimal transversal momentum, but with a rather high component in the backward direction.

The electron momentum distribution in the final state of the correlated TI is displayed in figure 2.7. The distributions are computed for the collision of different projectile ions with a velocity of $v_P = 16$ a.u. on a helium target atom. Two peaks can be identified at the expected electron momenta for Thomas TI and eeTI. With increasing charge state of the projectile ion, the relative importance of the Thomas TI decreases.

Shake-off and shake-over

If a target electron is captured by the projectile ion, there is a sudden change in the effective target potential, and there might be an overlap of the state of a second target electron with a continuum state. In the so called shake-off process, this electron suddenly finds itself in the continuum. Accordingly, there is only a minimal momentum transfer to the emitted electron [MBB+95].
There is also a process referred to as shake-over. Here, the interaction of the projectile with the target system leads to the ionization of a target electron, and the second electron finds itself in a bound projectile state [MDAS88]. Generally, the cross sections for shake-off and especially shake-over are very small, and the processes are neglected in most cases.

(a) proton projectile

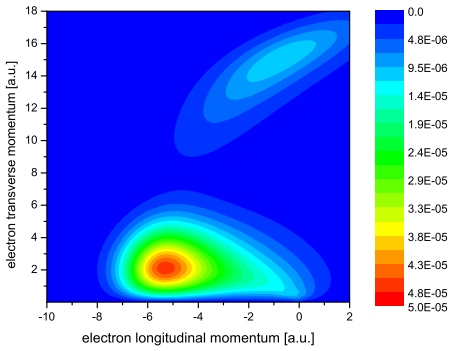

(b) He^{2+} projectile

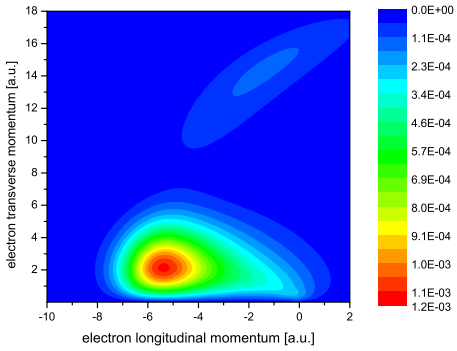

(c) Li^{3+} projectile

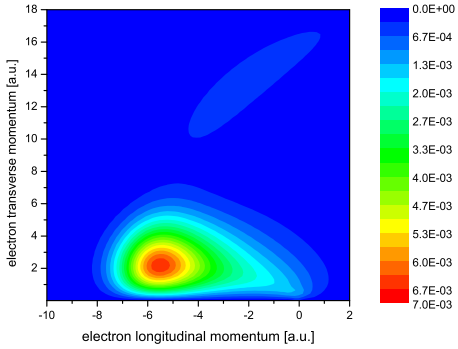

(d) Be^{5+} projectile

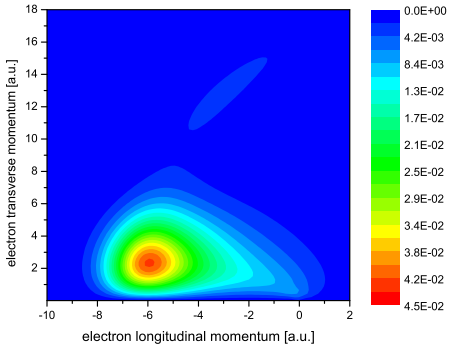

Figure 2.7: Panels (a)(b)(c) and (d) display the calculated electron momentum distribution in the final state of correlated transfer ionization by different projectile ions. In all calculations, the projectile velocity is $v_P = 16$ a.u., and the target is a helium atom. In (a), two separate peaks can be assigned to the Thomas TI and the eeTI, where the eeTI contribution to the total cross section is much stronger. With increasing projectile charge state, the Thomas TI contribution decreases relatively, and is hardly present in (c) and (d).

3 Experimental setup

In this chapter, the experimental techniques employed in this work will be described.
The final state momenta of the collision fragments are measured with a Reaction Microscope (section 3.1), which consists of a COLTRIM-spectrometer (Cold Target Recoil Ion Momentum Spectrometer) [UDL+91] combined with an electron spectrometer. Reaction Microscopes have been applied with great success in fragmentation studies by ion, electron and photon impact (see e.g.[UMD+97, UMD+03, DMJ+00]). In our work, an additional photon detector was implemented into the setup (section 3.2). It is dedicated to the detection of photons originating in radiative collision processes.
The Reaction Microscope is implemented into the heavy ion storage ring TSR (section 3.4). In the TSR, ion beams of extremely high quality, i.e. with a low emittance and momentum spread, can be prepared. Therefore, the initial state of the ion-atom collision is known with a high accuracy, and the combination of the devices (section 3.5) allows for the investigation of ion-atom collision processes with a very good resolution. High intensities of the stored ion beams result in high event rates, and good statistics can be obtained even for collision processes with small cross sections.

3.1 Reaction Microscope

In ion-atom collisions, a variety of processes may occur, e.g. single or double ionization, electron capture or electronic excitation, all differing in the final state of the collision system. To obtain kinematically complete data sets, it is necessary to measure $N - 4$ momentum components, if N is the number of collision fragments in the final state. The remaining four components can be calculated from energy and momentum conservation laws.
The final state momenta of the recoil ions and the electrons are measured with the Reaction Microscope. At the centre of the spectrometer of the Reaction Microscope, the projectile ion beam intersects with a target atom beam from a supersonic gas jet. Two time and position sensitive detectors are employed for the detection of recoil ions and electrons, respectively. As the solid angle acceptance of the recoil ions, and of the electrons over a wide energy range, is nearly

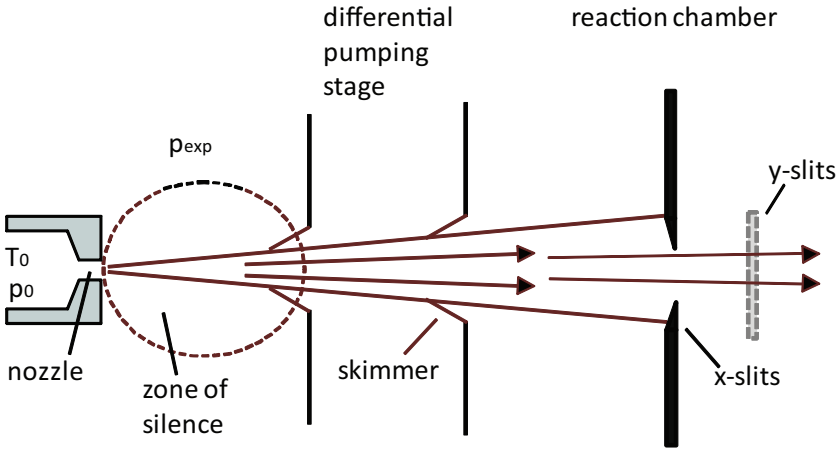

Figure 3.1: The supersonic gas jet.

4π, and as the electron detector is multi-hit capable,[1] kinematically complete multi coincidence studies are feasible. The momentum change of the projectile ions is not measured directly, but is accessed via momentum and energy conservation. Therefore, even small projectile scattering angles in the μrad range are observable, and the resolution is not limited by the projectile beam emittance or energy spread [USBK88]. A short overview over the components of the Reactions Microscope will be given on the following pages.

3.1.1 The supersonic gas jet

There are several demands on the atomic target in a Reaction Microscope. The momentum spread of the gas atoms has to be small in order to maintain a good resolution. At room temperature (300 K), the thermal momentum spread of helium gas is about 4 a.u.. But in order to achieve a resolution of 0.1 a.u. for the recoil ion momenta, the target temperature cannot exceed 150 mK (see [Fis03]). Also, the target should be well localized to produce a small overlap with the projectile beam. An effective pumping of the target gas is important, in order to maintain a background pressure in the ultra-high vacuum (UHV) range of about 10^{-10} mbar in the reaction chamber.

These demands are fulfilled by a supersonic gas target, which is based on the principle of adiabatic expansion. From a reservoir at a pressure p_0, the target gas of temperature T_0 is streaming through a small nozzle into an expansion chamber with lower pressure p_{exp}. If the pressure ratio $\frac{p_0}{p_{exp}}$ is about two or larger (more details in [Sco88]), in a region of several cm, the so called

[1] Multi-hit capability means that two or more electrons originating from the same collision are both detected, i.e. the dead time of the electron detector is very short.

zone of silence, the atoms expand adiabatically and move faster than the local speed of sound. The free enthalpy $H = \frac{5}{2}k_B T_0$ is converted to directed kinetic energy $p_{jet} = \sqrt{5k_B T_0 M}$, where M is the mass of the atoms, and k_B is the Boltzmann constant. This conversion is complete only for an ideal gas, in practice the gas atoms interact with each other and with atoms of the residual gas. The inertial temperature T of the gas after expansion depends on the gas species, on the product of pressure p_0 and nozzle diameter d and on the temperature T_0 prior to expansion. It is described by the speed ratio S, which is the ratio of directed velocity v_{jet} and thermal velocity v_{therm} of the gas jet, $S = \frac{v_{jet}}{v_{therm}} = \sqrt{\frac{5T_0}{2T}}$.
In the gas jet employed in this work, the nozzle diameter was $d = 30\,\mu$m, and a pressure $p_0 = 15$ bar results in a speed ratio of $S \approx 30$ for helium gas [Sco88]. A helium gas at room temperature has therefore a temperature of $T = 0.83$ K after expansion, resembling a momentum spread of $\Delta p \approx 0.24$ a.u.. The directed velocity v_{jet} of the helium gas jet is 5.9 a.u. [Fis03]. More detailed information on supersonic gas jets can be found in [Lan07, US03] and [Sco88].

When the jet is expanding in the zone of silence, only the part with the smallest transverse velocity passes through a skimmer into the next differential pumping stage (figure 3.1). After that stage, the beam passes a second skimmer, which again blocks the atoms with high transversal velocity. The diameter of the second skimmer is 0.6 mm, and it has a distance of about 3 cm to the nozzle. This jet geometry and the jet velocity result in a transverse momentum spread of the target beam of $\Delta p \approx 0.12$ a.u. after the second skimmer [Fis03]. In our work, the momentum spread was further decreased by the implementation of two collimator slits , which could be moved into the beam from all four transversal directions (see figure 3.1). Thereby, a cold and very well localized target beam was prepared.
The ultra high vacuum in the range of 10^{-10} mbar in the reaction chamber is maintained by differential pumping of the target beam. A typical pressure in the expansion chamber during experiments was $\approx 10^{-3}$ mbar, and about 10^{-6} mbar in the second stage. The pumping speed in the expansion chamber was 500 l/s, in the second stage 300 l/s, and the two additional pumping stages, in which the collimators are implemented, were pumped at a speed of 70 l/s each. After the reaction chamber, the target jet is pumped in the last differential pumping stages in order to prevent back-diffusion of gas into the collision region. The two differential pumping stages of the dump were pumped with a speed of 300 l/s each, and the pressure in the beam dump was typically in the range of 10^{-9} mbar.

(a) (b)

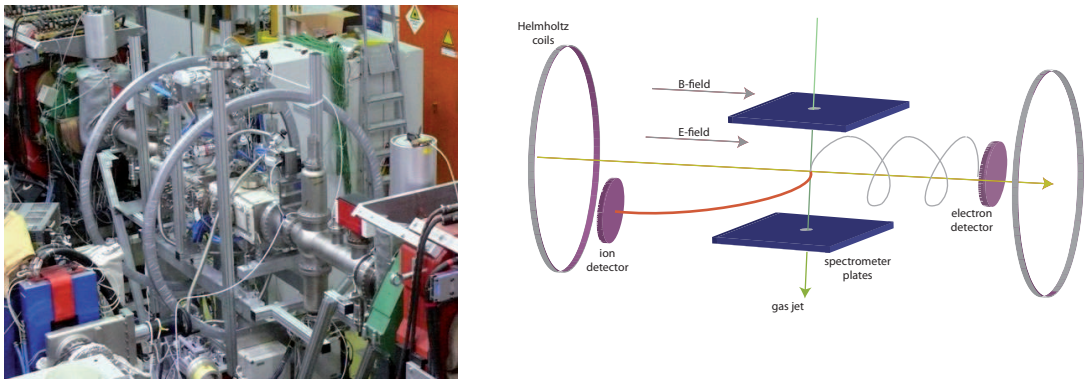

Figure 3.2: (a) A photograph of the Reaction Microscope implemented into the TSR. (b) A schematic drawing of the Reaction Microscope. In the reaction volume, the projectile ion beam is intersected with the atomic gas target. The charged collision fragments are accelerated in the electric extraction field and guided to the detectors. A magnetic field is forcing the electrons into a cyclotron motion.

3.1.2 The spectrometer

The working principle of a Reaction Microscope (figure 3.2) is as follows: In the interaction region in the middle of the spectrometer, the projectile ion beam is intersected with the gas target. The size of the overlap is small, as in our experiment the target beam has a diameter of about 3 mm in beam direction and the electron-cooled beam is only $\sim$ 1 mm in diameter. A weak electric field of typically a few V/cm is applied roughly parallel to the projectile beam direction to guide the recoil ions onto the surface of the ion detector. The same field is directing the electrons into the opposite direction.[2] A magnetic field forces the electrons onto a spiralling trajectory, so that even electrons with large transverse momentum reach the electron detector. The electric field is generated by two spectrometer plates of $20 \cdot 22$ cm, with a 1.5 cm hole in the middle for the target beam. They are ceramic plates with a high resistance coating. A voltage can be applied on each corner of the plates separately, allowing to optimize the orientation and strength of the extraction field. In same experiments in this work, circuit plates covered with 100 conducting metal stripes connected over 10 Ω resistors were used instead. This type of plates provides a somewhat more homogeneous electric field. They do not allow a separate potential on every corner, but the potentials on the first and last stripe can be adjusted independently, as well as the potentials of the lower and the upper plate.

[2] As the velocity of the projectile beam is high, the influence of the extraction field on the projectile ions is negligible.

The ions are accelerated in the acceleration region of length a between the spectrometer plates, and then pass a field free region. The purpose of the so called drift region is time focussing. As the interaction region has a small extension, not all ions are created at exactly the same distance to the detector surface. Ions with a higher distance take a longer time to pass the acceleration region, but gain a higher velocity and pass the drift region faster. When the length b of the drift region is two times the length of the acceleration region, $d = 2a$, the small variation of the starting position is compensated and the momentum resolution along the direction of extraction is essentially defined only by the temperature of the gas target. Therefore, in this direction the best resolution is achieved. The spectrometer described here has an acceleration region of $a = 11\,\text{cm}$ and a drift region of $d = 22\,\text{cm}$. As the longitudinal momentum transfer is of high importance in collision kinematics, the direction of extraction is chosen to be parallel to the projectile beam.
After passing the drift region, the recoil ions are monitored on a 2-dimensional position sensitive detector. To let the projectile beam pass above, the detector is mounted below the spectrometer axis. The offset of the detector with respect to the spectrometer axis is compensated by the directed velocity of the gas jet ($v_{jet} = 5.9\,\text{a.u.}$) and can be enhanced by the voltages applied to the spectrometer plates.
The ejected electrons have about the same momentum as the recoil ions, but due to their much smaller mass, their energy is much higher. The energy gained during acceleration by a recoil ion is by far larger than the energy obtained in the collision, which is not the case for electrons. The electric field is not sufficient to guide the electrons onto the electron detector. A magnetic field of usually $10 - 20\,\text{Gauss}$ is superimposed almost parallel to the projectile beam direction, forcing the electrons on a spiral trajectory towards the detector. The electron detector is mounted sideways of the projectile beam, and the magnetic field is tilted by some degrees with respect to the beam, in order to guide the electrons along the field lines from the interaction region to the centre of the electron detector.
The magnetic field is produced by an assembly of Helmholtz coils surrounding the spectrometer setup, with a diameter of $1.6\,\text{m}$ and a distance of $0.8\,\text{m}$. Also the recoil ions are affected by the magnetic field, being forced on a cyclotron motion as well. But due to their high masses, the effect is small and can easily be corrected in the data analysis.

The detectors

Three detectors are implemented in the spectrometer setup, detecting the time of flight and position of recoil ions, electrons and photons, respectively. Even though they are dedicated for different particles, the working principle is always the same. They consist of a pair of Micro

Channel Plates (MCPs) and a position sensitive anode. In the electron detector a stack of two 80 mm diameter MCPs and a Delay Line anode is employed. The recoil ion detector containing two 40 mm MCPs and a Wedge and Strip (W&S) anode was at some point exchanged by a detector of two 80 mm diameter MCPs and a Delay Line anode. The assembly and the characteristics of these detectors is in great detail described in [Sel10]. The photon detector contains a stack of two 40 mm diameter MCPs, and the front plate has a CsI coating for enhanced photon efficiency in the desired energy range (see section 3.2) and a Wedge and Strip anode.

Micro Channel Plates A Micro Channel Plate (MCP) is a thin plate consisting of small glass capillaries. The diameter of the capillaries is 25μm, resulting in an open area and thereby an efficiency of $\sim 60\,\%$. The particles are accelerated onto the detectors surface, the maximum efficiency is obtained for ions with a kinetic energy of 2 kV and for electrons with 200 – 300 eV [DMJ$^+$00].
When the charged particle hits the inner surface of a capillary, one or more electrons are released. As there is a voltage difference in the range of 1 kV applied between the front and back of the plate, each capillary works as an electron multiplier, and a multiplication factor $\sim 10^4$ can be obtained in one plate. Usually, a stack of two ("Chevron") or three ("Z-stack") MCPs is used to gain a higher multiplication factor. The capillaries are tilted about 13° relative to the plate's surface normal to prevent the particles from penetrating to deep into the plate before they hit the glass surface. The timing information is picked up on the front or the back side of the MCP stack, and time resolution is well below 1 ns. More details on microchannel plates can be found in [Wiz79].

Position Sensitive Anodes A cloud of $10^7 - 10^8$ electrons leaves the MCP stack and is accelerated over a short distance (a couple of cm) onto the position sensitive anode, where it has spread to a size of a few mm.
On a Wedge and Strip (W&S) anode, a high-resistive Ge-layer is evaporated on a thin (1.5 mm) ceramic or glass plate in three separate areas which form a wedge-and-strip structure. The electron cloud has to be extended sufficiently to cover a part of all three areas. The relative sizes of the areas layered by the wedges and stripes change linearly with the vertical and horizontal position, respectively. By analysing the relative charges of the electron cloud hitting all three areas, the position of the centre of the electron cloud can be calculated. The position resolution is mainly determined by the signal to noise ratio and can be as good as 0.05 mm [DMJ$^+$00].

In a Delay Line anode, a signal wire is wound around a suspending plate. The single windings have a distance of 0.5 – 1 mm, and the wire is on a positive potential. The electron cloud

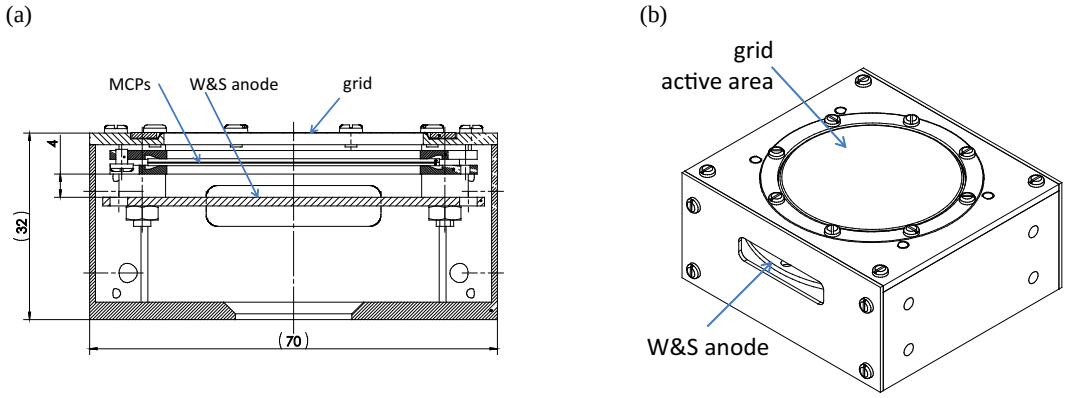

Figure 3.3: The microchannel plates and the W&S anode are mounted in a small box of stainless steel. The active area has a diameter of ~ 4 cm.

induces a signal in the wire, which is then propagating in both directions. The time difference of the signal arriving at both ends of the wire can be calculated back to an one-dimensional position information. A second signal wire wound perpendicular to the first one provides the information in the second dimension. To achieve a very good signal to noise ratio, each signal wire is paired with a second wire held on a lower potential. These wires therefore pick up not the signal electrons but only the noise, which then can be subtracted from the signal.
As the overall propagation time through the wires is known, the signals induced by different impacts in a short time can be assigned correctly. The multi hit capability and thereby the allowance for high count rates are the main advantages of the Delay Line anode. The dead time due to the used electronics is about 10 ns [Fis03], compared to few μs for W&S anodes, and the position resolution is typically better than 0.1 mm [DMJ+00]. For more details on Delay Line anodes see e.g. [SLRH91] or [CVB+05].

3.2 The photon spectrometer

For the investigation of radiative processes, a photon detector was added to the setup. The detector consists of a stack of two Micro Channel Plates, of which the front plate is coated with Caesium Iodide (CsI) to enhance the detection efficiency. Behind the MCPs, a Wedge and Strip anode is mounted. The MCPs and the anode are mounted in a small box of 70 mm · 64 mm · 32 mm, which fits between the two spectrometer plates of the Reaction Microscope. The front of the box is covered with a fine metal mesh (see figure 3.3).

As photons are neither influenced by the electric nor the magnetic field, the detector was mounted close to the interaction region, in order to cover a large solid angle. The photon de-

tector distorts the elctric field between the spectrometer plates, and is therefore equipped with six correction electrodes.
Photon detection is not necessary in every experiment. For that reason, the photon detector is mounted on a movable rod and can be completely moved out of the space between the spectrometer plates. The complete assembly is shown in figure 3.5.

3.2.1 Coated microchannel plates

A bare Micro Channel Plate has a low Quantum Detection Efficiency (QDE) for photons in the X-ray energy range. It varies with the exact photon energy and incident angle, but lies characteristically between 1 – 10%. A higher detection efficiency is achieved by coating the MCP with a photocathode material of higher photoelectric yield. The photocathode material is evaporated onto the MCP (for more details on the procedure see [CEM87]), building a surface layer of about 10000 $\mathring{A}$ and penetrating the channels. The layer must be sufficiently thick to stop the incident photons of energy E_γ. [3]
For a given photocathode material, the QDE strongly depends on the energy of the incident photons. A lot of photocathode materials were experimentally explored, for example KCl and Kbr [SES$^+$87, SLEV88, SEH$^+$88], and KI, NaBr and CsBr [MSS06]. A very popular photocathode material is Caesium Iodide (CsI), data on its QDE over different ranges of energy or wavelength can be found in e.g. [FBP$^+$84, CEM87, LFP$^+$96, FPL87].
Nevertheless, there are not so many data available for photon energies as high as 4.6 keV, which is the photon energy range we were interested in (see chapter 6). Chapell et al.[CEM87] measured a QDE of about 10 % for 4.51 keV photons for a CsI-coated MCP, with a maximum at a grazing angle of a few degrees (see e.g. [MSS06, FBP$^+$84, FPL87, CEM87]).
In [WPFB84] it is shown that an exposure of 8 hours to laboratory air does not significantly change the detection efficiency of the CsI coated MCP. Nevertheless, a serious effect was ob-

[3] The probability for the photon to be absorbed at a depth between z and $z+dz$ is $\mu \cdot \mathrm{cosec}\,\alpha' \cdot \exp(-\mu\, z\, \mathrm{cosec}\,\alpha')\, dz$, where μ is the linear absorption coefficient of the material [Fra83]. The released photo- and possibly Auger-electrons can either escape to the vacuum, or they produce secondary electrons of lower energy in the cathode material, which can than initiate the electron avalanche in the MCP which result in the detection of the photon hit.
The probability P_{esc} for a photoelectron to escape to the surface is given by [Fra83] to be

$$P_{esc} = \begin{cases} \frac{1}{2}(1 - z/R_e) & , z < R_e \\ 0 & , z > R_e \end{cases} \tag{3.1}$$

with the range R_e of the photoelectron in the material. The probability $P_s(z)$ of a secondary electron to escape is

$$P_s(z) = P_s(0)e^{-z/L_s}, \tag{3.2}$$

where L_s is the secondary electron escape length. For more details see [Fra83, FBP$^+$84].

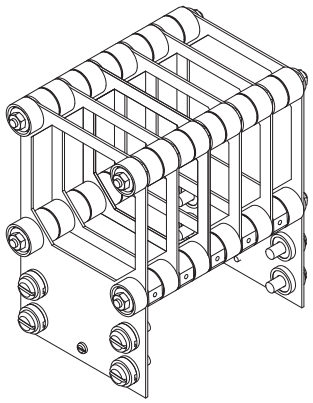

Figure 3.4: The shielding electrodes of the photon detector setup. Potentials can be applied to the front and the back electrode, and the voltage drops linearly over all six electrodes. The distance between two electrodes is 15 mm.

served for a long time storage in a vacuum of only 10^{-2} mbar, reducing the quantum detection efficiency by a factor of two after 40 days.

3.2.2 The shielding

In order to achieve a large solid angle, the photon detector was installed close to the interaction region, where it distorts the fields which guide the electrons and ions towards the detectors. The effect of the field distortion on the time of flight and position of the charged particles was simulated with the program SimIon. In a first simulation the photon detector chassis was put on ground potential and placed close to the reaction volume. The spectrometer voltages were chosen to change between 60 and -70 V from the electron side to the recoil ion side. The most serious effects were observed in the time of flight of the recoil ions. A shift of the starting point of the ion by ± 1 mm towards or away from the photon detector surface (x-coordinate) results in a time of flight difference of 24 ns, which corresponds to a longitudinal momentum uncertainty of ~ 1.1 a.u..

To reduce the distorting effect, shielding electrodes were installed in front of the photon detector (see figure 3.5). They consist of a row of $60\,\text{mm} \cdot 60\,\text{mm}$ metal rectangles with a $50\,\text{mm} \cdot 50\,\text{mm}$ hole through which the projectile beam and the recoil ions and electrons pass (see figure 3.4). Voltages can be applied to the first and the last shielding electrode, and the voltage changes linearly over the electrodes that are interconnected by a row of $100\,\Omega$ resistors.
A second simulation with implemented shielding electrodes showed that the shielding effect increases with shorter distances between the electrodes. But on the other hand, the electrodes

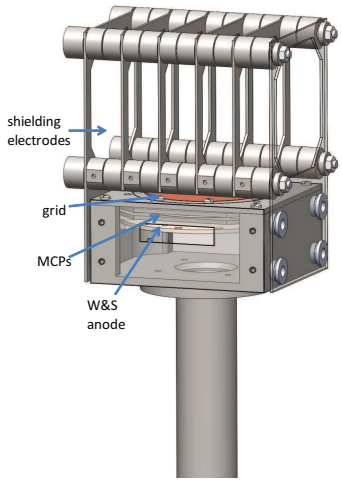

Figure 3.5: The complete setup of the photon detector, including the detector box and the shielding electrodes. The projectile ion beam and the charged collision fragments are passing through the centre of the holes in the electrodes. The target atom jet passes between the third and the forth electrode, so the reaction volume is placed in the middle of the shielding setup.

hinder the photons from reaching the detector surface. The best trade-off was reached in the simulation with 6 electrodes and 15 mm distance between them. With implemented shielding electrodes, the time of flight difference between recoil ions with ±1 mm differing x-coordinate was reduced to < 1 ns, the longitudinal momentum uncertainty thereby reduces to < 0.05 a.u..

3.3 Momentum reconstruction

In the spectrometer of the Reaction Microscope, the position of the particle impact onto the detector and the time of flight relative to a reference signal is measured. From these values, the three dimensional momenta of the collision fragments can be obtained. The longitudinal momentum along the initial projectile beam direction is directly related to the time of flight of the particle. The information of the transverse momentum is contained in the time of flight and the position on the detector surface, both for electrons and recoil ions. For a complete description in cylindrical coordinates, also the azimuthal angle ϕ in the plane perpendicular to the beam direction has to be obtained. The momentum reconstruction will be explained on the

following pages.

3.3.1 Longitudinal momenta

The longitudinal energy of a charged collision fragment after the collision is $E_{\parallel} = \frac{P_{\parallel}^2}{2m}$, where m is the mass of the particle. In the acceleration region of length a, the particle gains the kinetic energy $q \cdot U$, where U is the extraction potential and q the charge state of the particle. The movement through the drift region of length d is force-free. The movement through both regions adds to a total time of flight of

$$t_{\pm} = f\sqrt{m}\left[\frac{2a}{\sqrt{E_{\parallel}+qU} \pm \sqrt{E_{\parallel}}} + \frac{d}{\sqrt{E_{\parallel}+qU}}\right] , \tag{3.3}$$

where

$$f = 16.861\frac{ns}{cm}\sqrt{\frac{eV}{a.u.}} = 719.9 \cdot \frac{\text{ns}}{\text{cm}}\sqrt{\frac{\text{eV}}{\text{amu}}} . \tag{3.4}$$

The two different solutions, using the + or - in the calculation, correspond to initial momenta towards the detector (+) or in the opposite direction (-), respectively. As the inverse of equation (3.3) can not be calculated analytically, it can not be directly applied to derive the momentum. Additionally, the exact time of the collision is not measured directly. Instead of the absolute time of flight, only the relative time to a reference signal, for example the timing signal of a bunched beam or the detection of a charge changed projectile, is experimentally accessible.

As the mass of the recoil ion is high, the energy $E_{R\parallel}^{f}$ transferred in the collision is small compared to the energy $q \cdot U$ obtained during acceleration. Therefore, the time of flight difference Δt_R between an ions with $E_{R\parallel} = 0$ and with $E_{R\parallel} \neq 0$ can be approximated by

$$\Delta t_R = t(E_{R\parallel}) - t(E_{R\parallel} = 0) \approx \left[\frac{dt(E_{R\parallel})}{E_{R\parallel}}\frac{E_{R\parallel}}{dP_{P\parallel}}\right]_{P_{P\parallel}=0} \cdot P_{P\parallel} , \tag{3.5}$$

which results in

$$P_{R\parallel} = \left(8.04 \cdot 10^{-3}\frac{cm \cdot \text{a.u.}}{\text{eVns}}\right)\frac{qU}{a}\Delta t_R . \tag{3.6}$$

In case of high projectile velocities the time of flight distribution of the recoil ions is rather symmetric with a peak at $t_R(E_{R\parallel} = 0)$, which can be used as reference. As ions of different charge states q gain a different kinetic energy $q \cdot U$ in the acceleration region, the resulting time

of flight difference is large compared to the difference due to the energy $E_{R\|}$ transferred during the collision. Therefore, the charge states are well separated on the time axis and a separate time reference can be assigned to each.

For electrons, the longitudinal energy $E_{e\|}$ transferred in the collision and the kinetic energy $e \cdot U$ gained in the acceleration field are of the same order of magnitude and approximation (3.5) is not valid. Instead, the numerical Newton-method is employed, an iteration method where the solution of the non-linear equation is approximated until convergence is reached. In the Newton-method, the absolute time of flight of the electrons must be known. One method of obtaining the zero point on the electron time scale is taking advantage of the wiggle structure (which is described in section 3.3.2). Electrons with a time of flight of $t_e = 0$ would arrive at the detector in the moment of the collision, and their longitudinal momentum would be $P_{e\|} = \infty$. These electrons are not distracted by the magnetic field, as their angle in the cyclotron motion is $\alpha = \omega t_e = 0$. Accordingly, they hit the detector in one of the wiggle positions, which are equidistant in time. The measured wiggle positions can be extrapolated back until the zero point is reached.[4]

3.3.2 Transverse momenta

The measured position of the particle impact on the detector and time of flight contain the information about the transverse momentum component. For the recoil ions, the calculation of $P_{R\perp}$ is very straightforward, as their movement is barely influenced by the magnetic field. Also, the electric field has no effect on the momentum component transversal to the field lines. Recoil ions with $P_{R\perp} = 0$ reach the symmetry point of the detector. The offset of the recoil ion position on the detector to that symmetry point, given by the coordinate R_R, is directly proportional to the time of flight and to the transverse momentum of the ion:

$$R_R = \left(1.2 \cdot 10^3 \frac{\text{mm amu}}{\text{ns a.u.}}\right) \frac{P_{R\perp} t_R}{m_R} \tag{3.7}$$

The time of flight depends on the longitudinal momentum of the recoil ion. But as this time of flight difference is around three orders of magnitude smaller than the total time of flight,

[4] This method is not necessarily unambiguous. To certify that the right zero point is selected, it is employed that the longitudinal momentum transfer $q_\|$ is determined by energy conservation, $q_\| = \frac{Q+E_e}{v_P}$, and momentum conservation, $q_\| = P^f_{R\|} + P^f_{e\|}$. A correct selection results in $\frac{Q+E_e}{v_P} - (P^f_{R\|} + P^f_{e\|}) = 0$. For details, see [Fis03].

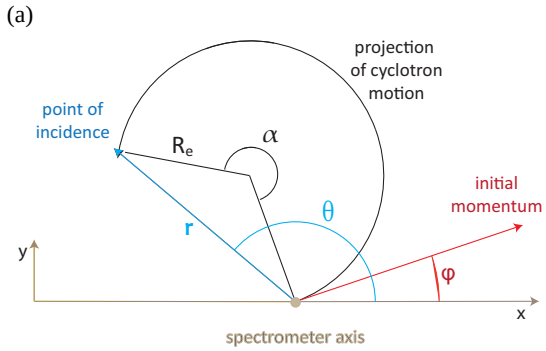

Figure 3.6: When the time of flight of the electrons is known, the transverse momenta can be extracted from the position spectrum.

equation (3.4) can be applied, and the transverse momentum in atomic units writes

$$P_{R\perp} = \left(11.6 \frac{\text{a.u.}}{\sqrt{\text{amu eV}}}\right) \frac{R_R}{2a+d} \sqrt{qU \cdot m_R} \ . \tag{3.8}$$

Due to their larger mass, the cyclotron motion of the recoil ions in the magnetic field does not cover a full circle, but only a few degrees. Considering this tilt, the azimuthal angle ϕ_R can be extracted directly from the recoil ion position on the detector.

The electron trajectories usually include a few cyclotron spirals during the time of flight t_e. Projected onto the azimuthal plane, the electrons move on circles of radius r (see figure 3.6). That radius is proportional to the transverse momentum of the electrons $P_{e\perp}$,

$$P_{e\perp} = r\, e\, B \ , \tag{3.9}$$

whereas the cyclotron frequency ω is independent of it. For a given charge to mass ratio, ω only depends on the magnetic field strength B; $\omega = \frac{e\,B}{m_e}$. The cyclotron frequency determines the angle α which the electron covers in the time of flight t_e, with $\alpha = \omega t_e$. The offset of the electron position on the detector from the symmetry point can be extracted from the electron position spectrum (figure 3.6). With the time of flight and the cyclotron frequency, the cyclotron radius r is determined over

$$r = \frac{R_e}{2|\sin\frac{\alpha}{2}|} = \frac{R_e}{2|\sin\frac{\omega t_e}{2}|} \ , \tag{3.10}$$

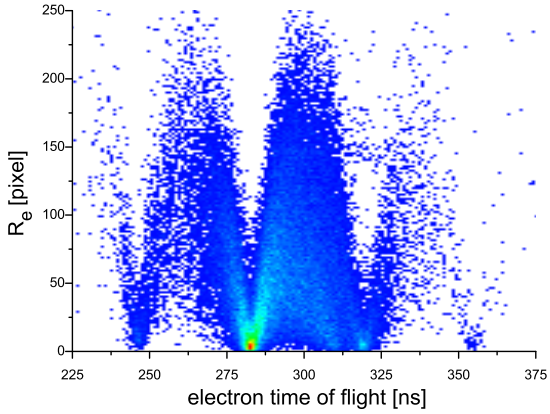

Figure 3.7: The distribution of electrons on the electron detector depending on their time of flight displays the characteristic wiggle structure. The electrons emitted in a 1 Mev/u O^{7+} on helium collision perform a cyclotron motion in the magnetic field. At the times when that motion covers a full circle, the electrons arrive at the detector at the point of symmetry where $R_e = 0$.

and applying equation (3.9) gives the transverse momentum in atomic units:

$$P_{e\perp} = \left(8.04 \cdot 10^{-3} \frac{\text{a.u.}}{\text{mm G}}\right) \frac{R_e B}{2|\sin\frac{\omega t_e}{2}|} \tag{3.11}$$

The azimuthal angle ϕ_e can be obtained from the angle θ in the electron position spectrum (see figure 3.6), as

$$\phi_e = \theta - \frac{\omega t}{2} \ . \tag{3.12}$$

An exact knowledge of the cyclotron frequency ω is essential in the determination of $P_{e\perp}$ and ϕ_e. In principle, ω can be calculated from the measured magnetic field strength B. But as the field strength inside the spectrometer is not measured with high accuracy, this calculation would result in an uncertainty of ω and thereby α. Instead, ω can be obtained using the 'wiggle' structure (figure 3.7). At certain times of flight the cyclotron motion of all electrons, regardless of their momenta, covers a full circle. At these times, the electrons hit the detector at the symmetry point and $R_e = 0$. In figure 3.7, where R_e is displayed over the electron time of flight, the so called wiggle structure is visible. At the position of a wiggle, there is no transverse momentum resolution. The time distance Δt_e between two wiggles gives the time of one circulation and thereby the angular frequency $\omega = \frac{2\pi}{\Delta t_e}$ can be obtained in great detail. The time difference of

≈ 35 ns in figure 3.7 corresponds to a magnetic field strength of ~ 10 a.u..

3.3.3 Resolution and acceptance

The momentum resolution of the Reaction Microscope is determined by the temperature of the gas target and the accuracy of the time of flight and position measurement, where the position resolution depends on the spatial resolution of the detectors, and on the extension of the reaction volume. The accuracy of the time of flight determination depends on the time resolution of the detectors, on field inhomogeneities in the spectrometer and also, in case the reference signal is posed by the bunches of the projectile beam, on the length of the ion bunch.
A detailed analysis of the resolution and acceptance of the spectrometer was performed by Fischer [Fis03]. The momentum resolution for the recoil ions is typically 0.1-0.2 a.u. in longitudinal direction, and a factor of 2 to 3 higher in transverse direction.
The acceptance of recoil ion transverse momenta is determined by the size of the detector and the acceleration voltage. It can be deduced directly from equation (3.8) by inserting the maximal possible offset $R_{R\,max}$ of the recoil ion position from the symmetry point on the detector.
Due to their cyclotron motion in the magnetic field, the momentum resolution of the electrons depends on the time of flight. Generally, the longitudinal resolution is $\Delta P_{e\|} \ll 0.1$ a.u. over a wide range of longitudinal electron momenta. At the position of a wiggle, there is no transverse momentum resolution for the electrons. In the middle between two wiggles, the best resolution for $P_{e\perp}$ and ϕ_e is reached, with typical values of $\Delta P_{e\perp} < 0.1$ a.u. and $\Delta\phi \approx 10^\circ$ [Fis03].
The longitudinal momentum acceptance for the electrons is determined by the extraction voltage, because electrons moving away from the detector with an energy higher than $e \cdot U$ leave the extraction volume on the opposite side. Therefore, the condition on the longitudinal electron momentum reads

$$P_{e\|} > -\sqrt{\frac{e \cdot U}{13.6}}\,\frac{\text{a.u.}}{\sqrt{\text{eV}}}\ . \tag{3.13}$$

The transversal momentum acceptance can be derived from equation (3.11). When $R_{e\,max}$ is the maximal possible offset to the point of symmetry on the detector, and when the time of flight of the electron is exactly between two wiggles, the condition for transversal acceptance reads

$$P_{e\perp} < \left(4.02 \cdot 10^{-3}\frac{\text{a.u.}}{\text{mm G}}\right) \cdot BR_{e\,max}\ . \tag{3.14}$$

In our experiments, a typical longitudinal acceptance is $P_{e\|} > -2$ a.u., and the electrons are detected with a transversal momentum of $P_{e\perp} < 2$ a.u..

3.4 The heavy ion cooler storage ring TSR

Especially in the fields of atomic and molecular physics, ion storage rings are a valuable experimental tool. When the last obstacles were overcome - providing a ultra high vacuum at moderate cost and the handling of phase cooling - a number of small ion storage rings were build in the late eighties and in the nineties of the last century. The Test Storage Ring (TSR) at the Max-Planck-Institut für Kernphysik in Heidelberg is one of these rings, it started operation in 1988 [BBF+88]. In the TSR, ion beams can be stored with high intensity over a wide range of charge states and energy. By electron cooling, a small emittance and momentum spread of the stored ion beams is obtained. Due to its properties, the stored ion beam in the TSR is an excellent projectile beam for the investigation of ion atom collisions with a Reaction Microscope.

3.4.1 The lattice of the TSR

A photograph of the ring is shown in figure 3.8, and a schematic drawing in figure 3.9. The TSR has a circumference of 55.4 m, containing four straight sections, each 9.5 m long. The first straight section is devoted to the injection and extraction of the ion beam. In the second section, the electron cooler is located, whereas the next straight section is dedicated for experimental equipment. In this section, the Reaction Microscope is implemented. The last section is occupied by the radio frequency generator and the beam diagnostics system.
The bending of the ion beam is performed by eight 45° dipole magnets, two placed in each corner of the TSR. The maximum field of the magnets is $B_{max} = 1.3\,\mathrm{T}$, and the ion beam has to be bent in a radius of about $\rho = 1.15\,\mathrm{m}$. Thereby the maximal rigidity of the stored ion beams is given, which is the maximal momentum to charge ratio, $R_{max} = \frac{P_{P,max}}{Q_P} = B_{max} \cdot \rho = 1.5\,\mathrm{Tm}$.[5] Ions with a typical charge state to mass ratio of 0.5 can be stored up to kinetic energies of about $E_{proj} = 30\,\mathrm{MeV/u}$. The minimal rigidity is about $R_{min} = 0.25\,\mathrm{Tm}$.

Focussing of the ion beam is achieved by five families of four quadrupole magnets. The quadrupole magnets are either horizontally or vertically focussing, and in figure 3.9 they are labelled with QF and QD, respectively. A horizontally focussing quadrupole between two dipole magnets is the centre of one focussing period, which extends over a pair of quadrupoles and half a straight section on each side. As the lattice of the ring consists of four of these focussing periods, it has a fourfold symmetry. In the main operation mode (or standard mode) of the TSR, adjacent focussing periods are anti-symmetric, resulting in the ring's super-periodicity of two.

[5] This equation is obtained by equalling the Lorentz force $F_L = Q_P(v_P \times B)$ with the centrifugal force $F_C = M_P v_P^2/\rho$

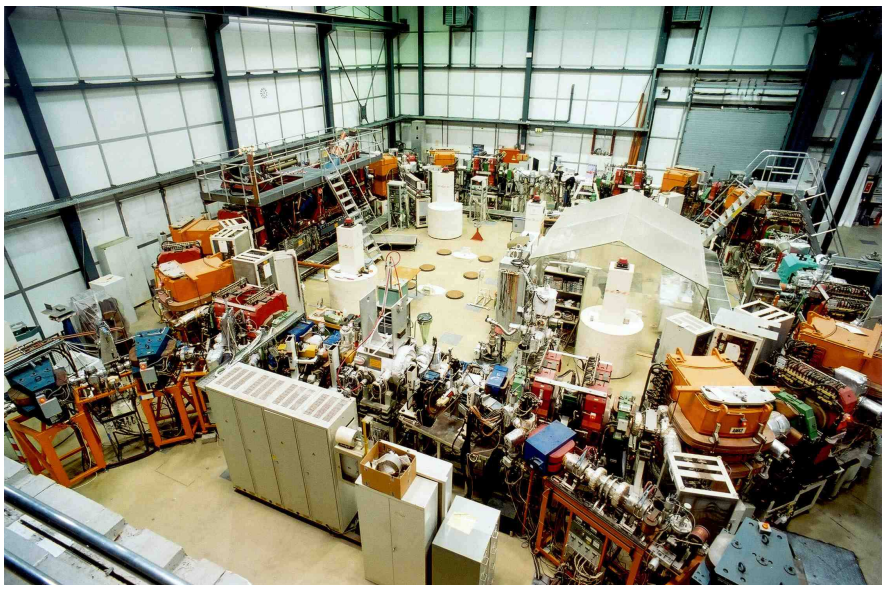

Figure 3.8: A photograph of the heavy ion cooler storage ring TSR. The ions are injected from the beamline visible in the lower right corner. The dipole magnets can be recognized by their orange colour.

Emittance and acceptance

The central orbit, sometimes also called closed orbit, is the trajectory of a stored projectile ion with a certain longitudinal momentum P_P. The longitudinal position of the ion circulating in the storage ring is denoted by s, where $s = 0$ marks the centre of the beam diagnostics section. The experimental section is located at around $s = 42\,\mathrm{m}$. If the ion has a transverse momentum component, it leaves the central orbit and would be lost without the focussing quadrupole magnets. They exert a counteracting force on the ion which is proportional to its displacement x from the central orbit. Therefore, the ion performs a so called betatron oscillation motion around the central orbit, with a tune of ≈ 2.8 oscillations per turn in the standard mode.[6] After injection, the betatron oscillation amplitude can be as big as 2 cm in the centre of the experimental straight section. The slope of an ion orbit with transverse velocity v_x and momentum P_x is defined by $x' = \frac{dx(s)}{ds} = \frac{v_x}{v_P} = \frac{P_x}{P_P}$. In the phase space defined by x and x', the ion moves on an ellipse (see figure 3.10) when it circulates in the storage ring. The area A of that ellipse is a constant for the movement of every ion, and the emittance ϵ_{1x} of a single ion is defined by $\epsilon_{1x} = \frac{A}{\pi}$. The largest possible emittance of a stored ion is a characteristic of the storage ring, called acceptance. It is about 100 mm mrad in the horizontal direction.

[6] With a typical circulation frequency of $\approx 0.5\,\mathrm{MHz}$, the betatron frequency is in the order of $\approx 1\,\mathrm{MHz}$

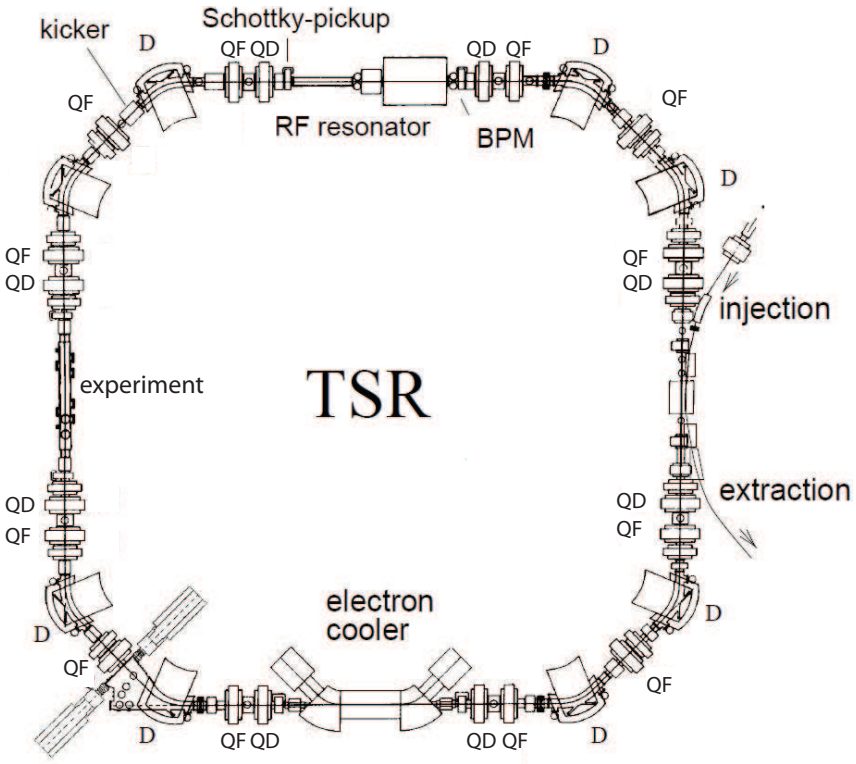

Figure 3.9: A schematic drawing of the TSR. The circumference of the storage ring is 55.4 m. The focussing and defocussing quadrupole magnets are labelled by QF and QD, respectively. Schematic drawing from [Beu00].

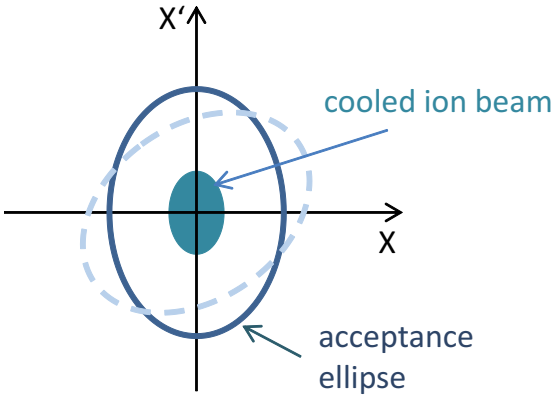

Figure 3.10: The emittance of the stored ion beam is an ellipse in the phase space. The largest possible emittance of a stored ion is determined by the acceptance of the storage ring. The acceptance ellipse has the same area at all positions in the ring, but might be tilted and distorted. Electron cooling reduces the emittance of the stored ion beam.

The emittance of not a single ion but of the ion beam is defined over the spatial profile of the ion beam. An electron-cooled ion beam is Gaussian shaped with a standard deviation σ_x (see figure 3.13), and the beam emittance ϵ_x is defined as the emittance of an ion at $x = \sigma_x$. [7] A typical emittance of a cooled ion beam is $\approx 0.05\,\text{mm mrad}$. It is reduced by electron cooling until an equilibrium with intra-beam scattering is reached (see below) then it is a constant characteristic of the ion beam, i.e. the area of the ellipse in phase space does not change. Still, as the ion beam circulates in the ring, the values of $x(s)$ and $x'(s)$ change, which results in a different beam size at different positions in the ring.

β- and dispersion functions

The size of the ion beam is expressed by the standard deviation $\sigma_{x,y}$ of its Gaussian distribution. Two β-functions $\beta_{x,y}(s)$ are employed to describe the variation of the beam size through the ring, $\sigma_{x,y}(s) = \sqrt{\epsilon_{x,y}\beta_{x,y}(s)}$. The β-functions $\beta_{x,y}(s)$, and thereby the beam size variations, are determined by the settings of the quadrupole magnets. The β-functions are calculated by the MAD8 program [GIKN89], and with the measured value of σ_x and σ_y, the vertical and horizontal beam emittance can be obtained. In the straight sections for injection and experiment, the values of the β-function are $\beta_x = 6\,\text{m}$ and $\beta_y = 2.5\,\text{m}$. Whereas at the electron cooler and diagnostics sections, the beam is slightly smaller in x-direction, and the values are $\beta_x = 3.3\,\text{m}$ and $\beta_y = 1\,\text{m}$ (see figure 3.11).

[7] Sometimes also a definition with $x = 2\sigma_x$ can be found.

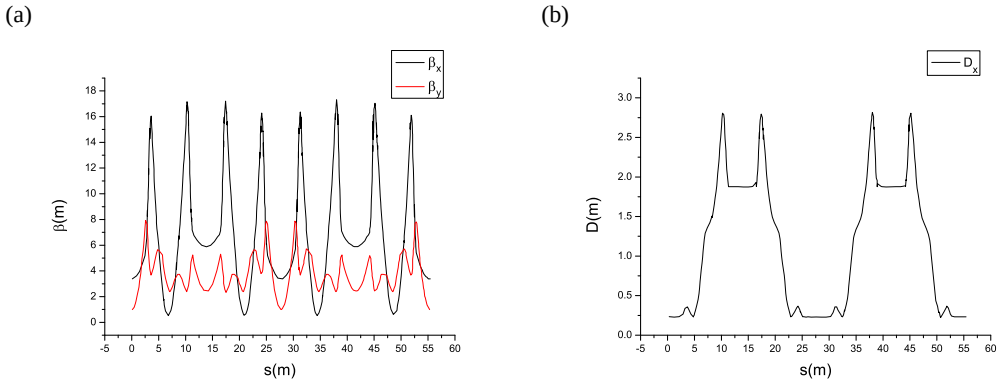

Figure 3.11: (a) The β_x- and β_y-functions of the TSR in main operation mode. (b) The dispersion function D_x. The functions are calculated by the program MAD8 [GIKN89].

Also defined by the settings of the quadrupole magnets is the dispersion $D(s)$ of the storage ring. The dispersion describes the location of the closed orbit of an ion with a certain momentum P_P circulating the ring. The dispersion determines the shift x_c of the closed orbit which results from a variation of the ion momentum by ΔP_P with $x_c(s) = D(s) \cdot \frac{\Delta P_P}{P_P}$. In the straight sections of electron cooling and diagnostics systems, the horizontal dispersion D_x is set to the low value of $\approx 0.25\,\mathrm{m}$, whereas in the sections of injection and experimental equipment, it is $\approx 2\,\mathrm{m}$. The $\beta_{x,y}$-functions as well as the dispersion function are displayed in figure 3.11. Due to the super-periodicity of 2, the values are repeated after half a circulation in the storage ring.

3.4.2 Beam injection

The ions which are to be injected have to be created in the desired charge state. They are extracted as singly-charged negative ions from a MIS-source and accelerated in a tandem Van de Graaff [RGHH74] with a terminal voltage of up to 12 MV. A foil strips the ions electrons from the ions at the point of highest voltage U_a in the accelerator, so if q is the charge state after stripping, the energy transferred to the ions is $(1 + q)\,U_A$. In order to produce highly charged ions, a second or even a third stripper foil can be placed behind the accelerator. Hereby, highly charged ions up to $^{197}\mathrm{Au}^{51+}$ can be created.

In the first straight section in the TSR, two magnetic septa and one electrostatic septum inject the ions into the ring. In order to overlap with the trajectory of the injected ions, the closed orbit must be distorted. This is accomplished by four bumper magnets and four additional magnets. The intensity of the stored ion beam can be increased significantly by multi-turn injection,

where several injections are made in succession. During multi-turn injection, the magnetic field of the bumper magnets is rapidly reduced to zero, thereby increasing the distance of the injected ions to the central orbit, until the horizontal acceptance of the storage ring is filled. For a typical acceptance of 100 mm mrad, a multiplication factor of 40 is reached.

3.4.3 Electron cooling

After injection, the beam has a horizontal width of about 40 mm, which can be converted into a temperature of approximately $5 \cdot 10^6$ °C for a $^{12}C^{6+}$ ion beam of $E_P = 73.3$ MeV. In order to decrease the beam temperature, an electron cooler is implemented in the second straight section of the TSR (see figure 3.12). The electron beam is extracted from the cathode by a high voltage and, guided by magnetic fields, it is overlapped with the ion beam in an interaction region of about 1.2 m length and finally carried to the collector.
Electron cooling is based on the Coulomb interaction of the ions and electrons in the interaction region. To cool the ion beam, the temperature of the electron beam has to be very small. The longitudinal momentum spread of the electrons is reduced by the acceleration in the high voltage field. The transverse temperature is lowered by adiabatic expansion of the electron beam in a decreasing longitudinal magnetic field. For an electron density of $n_e = 10^7\,\mathrm{cm}^{-3}$ and a velocity of $3 \cdot 10^5$ m/s, the longitudinal temperature is about 64μeV, and the transverse temperature can be reduced from 120 to 4 meV for beam radii of $4.8 - 26$ mm [Beu00].
When passing through the constantly renewed cold electron bath, the ion beam is cooled by transferring energy to the electrons. The cooling force depends on the relative velocity of ion and electron beam [Bet30]. On the other side, the ion beam is constantly heated by intra-beam scattering, resulting in an equilibrium emittance and momentum spread $\frac{\Delta P_P}{P_P}$ in longitudinal direction after around 500.000 circulations of the ion beam through the ring.
By damping the betatron amplitude, the ion beam is cooled down to a typical size of only a couple of mm (see picture 3.13) and a longitudinal momentum spread as small as $\frac{\Delta P_P}{P_P} \approx 10^{-4}$. Because of the intra-beam scattering, both values depend on the number of particles N, and thereby the beam intensity I_P. The beam size $\sigma_{x,y}$ is roughly proportional to $I_P^{0.2}$. The cooling time T_c depends on the ions' mass M_P and charge state Z_P as $T_C \propto \frac{M_P}{Z_P^2}$ and is usually in the range of $1 - 3$ s. More details on electron cooling can be found in [Beu00] and [BGN+03].

ECOOL stacking

The cooled ion beam is occupying a much smaller area in transverse phase space. The newly available phase space can now repeatedly be filled by the next multi-turn injection, and the beam can be cooled again. This process is called electron-cooling stacking (or ECOOL stacking). The

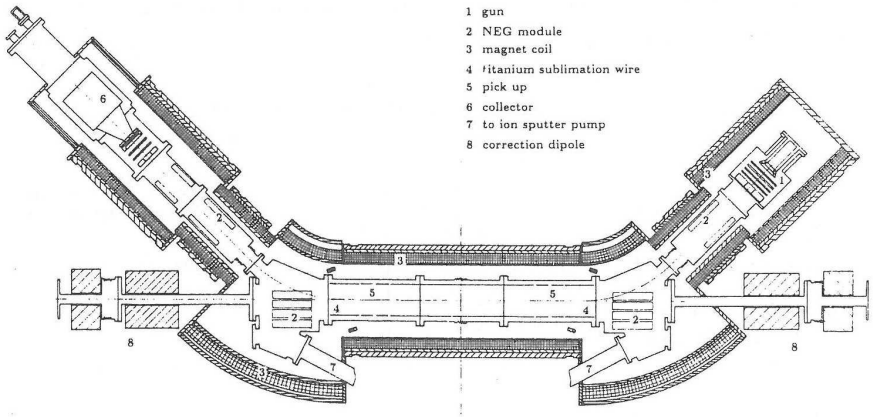

Figure 3.12: A schematic drawing of the electron cooler of the TSR. The stored ion beam passes from the right and is superimposed with the electron beam in the straight section in the middle. From [SBB+90]

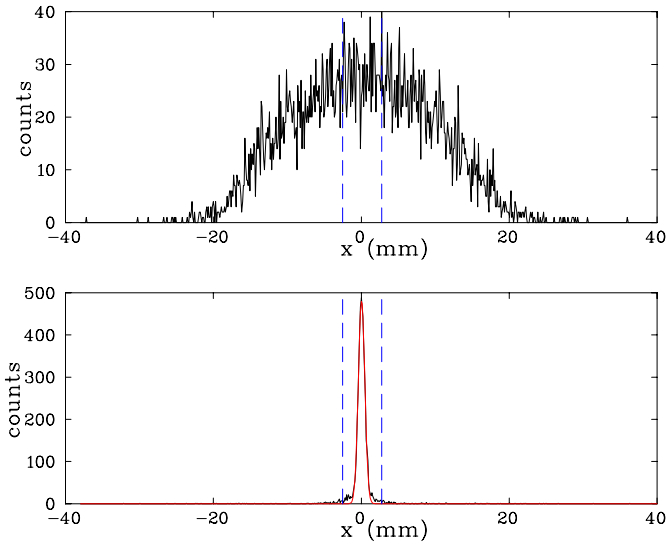

Figure 3.13: The upper picture shows the profile of an C^{6+}-beam after injection measured with the horizontal beam profile monitor (BPM). The lower picture shows the beam profile after electron-cooling. The time difference between the profiles is 2s. The profile of the electron-cooled ion beam is fitted by a Gaussian function with a standard deviation of $\sigma_{fit} \approx 0.4\,\text{mm}$. A correction for the resolution of the BPM results in a horizontal width of the C^{6+}-beam of $\sigma_{C6+} \approx 0.3\,\text{mm}$.

Ion	Energy [MeV]	Life time [s]	Intensity [μA]
p	21	220000	1000
$^{16}O^{8+}$	98		750
$^{12}C^{6+}$	73	1700	1000
$^{32}S^{16+}$	195	450	1500
$^{35}Cl^{17+}$	293	318	1000
$^{45}Sc^{18+}$	178		380
$^{56}Fe^{22+}$	250	77	70
$^{56}Fe^{23+}$	260	74	128
$^{58}Ni^{25+}$	342	60	600
$^{63}Cu^{25+}$	290	49	280
$^{63}Cu^{26+}$	510	122	100
$^{74}Ge^{28+}$	365	45	110
$^{80}Se^{25+}$	480	204	100
$^{80}Se^{31+}$	506	50	< 1
$^{197}Au^{50+}$	695	3	3

Table 3.1: Lifetimes and intensities that have been achieved for exemplary ions through electron-cooling stacking. The incoherent tune shift is the limiting factor for the intensity reached for beams with masses below A =35. From [Art12].

repetition rate is proportional to the inverse cooling time T_C. The achievable beam intensity is limited by the limited lifetime of the ion beam. Still, an intensity multiplication factor of up to 4000 can be reached, resulting in maximum beam currents of about 1 mA (see table 3.1).

Lifetime of the stored ion beam

The lifetime τ of the ion beam is defined over the exponential decay of the number of stored ions $N = N_0 e^{-t/\tau}$. After the time τ, the number N of ions is reduced by the factor e^{-1}. The lifetime is limited mostly by interactions of the stored ions with the electrons in the cooler and with residual gas ions. In the residual gas there are three main processes: Coulomb scattering, electron capture and electron stripping. The cross sections of these processes differ, but every process can be the dominating ion loss channel, depending on the ion charge state and energy. The lifetime of bare ions is mostly limited by electron capture, whereas a singly charged ion is more likely stripped. All cross sections increase with increasing mass number of the residual gas atom, so the lifetime is especially dependent on the concentration of heavier gas atoms. When ρ is the residual gas atom density, σ the cross section of the considered process and v_P is the velocity of the ion, the lifetime τ with respect to that process is calculated as $\tau^{-1} = \sigma \cdot \rho \cdot v_P$.

The lifetimes of some ion beams stored in the TSR are listed in table 3.1.
As a very good vacuum is crucial for the lifetime of the stored beam, the TSR is equipped with approximately 30 ion getter pumps and approximately 40 titan sublimation pumps. The ion getter pumps have a speed of 60 l/s each. In the electron cooler, two ion getter pumps with a speed of 400 l/s are installed, and additionally NEG pumps ST 707 (SAES Getters) are utilized. The whole vacuum system has to be baked out at a temperature of 300°C. A vacuum in the range of 10^{-11} mbar is reached.

3.4.4 The radio frequency resonator

It is possible to bunch the stored ion beam, i.e. to form ion 'packages' with a length of only about a few ns. The bunching is achieved by a ferrite loaded radio frequency (rf) resonator implemented into the fourth straight section of the TSR. The frequency range is 0.45 – 9 MHz, and the maximum rf voltage is $U_{rf,max} = 5\,\mathrm{kV}$.
When the voltage of the rf resonator is ramped up, the ions circulating in the ring form short longitudinal ion bunches. The resonator frequency f_{rf} has to be a multiple of the ions circulation frequency f_0, i.e. $f_{rf} = h \cdot f_0$, where h is the harmonic number which gives the number of bunches in the ring. The bunch length σ_B is decreasing with increasing resonator voltage U_{rf}, but the decrease is limited because the ions interact with the space charge field of the ion beam. Therefore, the bunch length increases with increasing beam intensity I_P. This results in $\sigma_B \propto \sqrt[3]{\frac{I_P}{h^2\beta^2 U_{rf}}}$, where β is the beam velocity in units of the speed of light c [Bas09]. For low beam intensities and high resonator voltages, very short bunches with a length of about a ns can be achieved. The ions perform synchrotron oscillations in longitudinal direction around the centre of the bunch. The frequency f_{synch} is proportional to $\sqrt{U_{rf}}$, and typically in the range of 1 kHz, which is three orders of magnitude slower than the betatron oscillation in transverse direction.
By varying the ferrite's permeability, the frequency of the resonator is changed and the ions are accelerated, see e.g. [Blu89, Bas09]. When the ion velocity increases, also the magnetic fields of the bending magnets in the TSR have to be ramped up. For instance, the energy of an pre-electron-cooled $^{12}C^{6+}$ beam can be increased by a factor 5 with an acceleration efficiency of 98%. For decelerating the same beam, and thereby reducing the energy by a factor ≤ 7, the efficiency is about 90% [Art12].

3.4.5 Beam diagnostics system

The beam diagnostics system is also placed on the fourth straight section of the TSR. The beam position is measured by eight pick-up position monitors, which basically consist of two metallic

plates each. The beam induces a voltage on both plates, and the voltage difference is proportional to the beam's distance to the pick-up centre. To measure not only the position but also the transverse density distribution of the stored beam, two beam profile monitor (BPM) units are employed. In the beam profile monitors, two parallel plates are installed and a high voltage perpendicular to the beam direction is applied. When the beam passes between the plates, it ionizes residual gas atoms and molecules. The electric field draws these ions onto a position sensitive detector mounted on one of the plates. As the number of ionized atoms is proportional to the density of the projectile ion beam, a projection of the beam density on the detector is obtained. One BPM measures the beam in the vertical and the other in the horizontal direction. The beam sizes displayed in figure 3.13 are obtained by the horizontal BPM.
A current transformer is used to measure the stored beam intensity with a resolution of 1μA. For currents smaller than 1μA, a current pick-up has to be used, but that is possible only for bunched and electron-cooled ion beams. The revolution frequency and the longitudinal momentum spread is measured by a Schottky pick-up.

Detector for charge changed projectiles

Some atomic processes in the experimental section of the TSR lead to a change of the charge state of a projectile ion. Due to the different Lorentz force acting on the charge changed ions, they are bent in a different radius in the bending magnets after the experimental straight section and leave the closed orbit of the stored beam. In order to detect these ions, a scintillator detector system is implemented in that section.
When reactions are investigated where the projectile ion gains or loses one or more electrons, the timing information of the charge changed projectiles' impact on the detector can be used as a trigger signal for the data acquisition.

3.5 The combination of the TSR and the Reaction Microscope

As already mentioned, the combination of a Reaction Microscope with the heavy ion storage ring TSR has major advantages, e.g. the small projectile beam size, small beam emittance and energy spread, and the possibility to 'bunch' the ion beam.
To be implemented into the TSR, the Reaction Microscope has to comply with certain requirements.
First of all, there are restrictions on the geometry, as no part of the spectrometer should block the stored ion beam. For that reason, the electron and recoil ion detectors can not be mounted directly on the spectrometer axis, which is equal to the ion beam direction. The recoil ion

detector is therefore positioned below the ion beam. This position is advantageous, because the target atoms already have a downward velocity component due to the expansion from the supersonic gas jet. The electron detector is positioned on the same height as the ion beam, but displaced sideways from the spectrometer axis. The electrons are guided towards the centre of the detector by the magnetic Helmholtz field, which for that reason is tilted by a few degrees respectively to the projectile beam.
The downward offset of the recoil ions can be increased by adjusting the voltages applied to the spectrometer plates. The recoil ion and electron momentum resolution is worsened with increasing offset of the detectors to the spectrometer symmetry axis. Therefore, the detectors are placed as close to the stored projectile beam as possible.

In section 3.4.3 the reduction of the beam size during electron cooling is described. Before it is electron-cooled, the injected beam extends over some cm, and the detectors have to keep that distance from the beam centre in order to let the beam pass. The cooled ion beam has a extension of about a mm, allowing the detectors to move much closer. Therefore, both recoil ion and electron detector are mounted on a manipulator operated with a stepping motor with a moving range of 10 cm. The movement of the detectors is connected to a trigger signal, which starts the injection of ions into the storage ring.
Thus, a fully automatic injection procedure is maintained: When triggered, the detectors move to a position with larger distance to the closed orbit of the ion beam. After a delay of a few seconds in which that movement takes place, the ion beam is injected into the ring. It is cooled within a few seconds, and the detectors move back to their positions close to the ion beam. Additionally, the data acquisition is suppressed during the moving period by the trigger signal. The signal can be given manually or by a pulse generator. The time between injections is chosen according to the lifetimes of the stored ion beam.
In practice, the recoil ion detector could often remain at one position, whereas the electron detector was typically moved about 4 cm, because the horizontal extension of the beam during injection is much larger than the vertical one.

A good vacuum is crucial for the lifetime of the stored ion beam. Also, electron capture from residual gas atoms lead to background hits on the detector for charge changed projectiles. Therefore, the rise of background pressure in the ring due to the gas target has to be restricted. A crucial limit is that the thickness of the gas target is at least ten times higher than the thickness of the background gas [SCS+97]. With the circumference of the TSR of 55.4 m, and an extension of 5 mm of the gas target, the density of the target has to be at least about 10^6 times higher than the background density.

A description of the supersonic gas jet can be found in section 3.1.1. A background pressure in the range of 10^{-10} mbar in the reaction region was maintained by the implementation of two additional pumping stages between the expansion volume of the gas jet and the reaction chamber. Moreover, each of the two stages was equipped with an adjustable collimator, allowing for the preparation of an even better localized target beam (see figure 3.1).

The combination of the Reaction Microscope and the TSR allows to measure the extension of the target jet, the target thickness N_t, and also the target density n_t.
The target thickness is given by

$$N_t = \int_0^l n_t ds \ , \tag{3.15}$$

where l is the extension of the gas target in x-direction.
The stored ion beam can be moved horizontally in the TSR, because a change in the magnetic field of the bending dipole magnets results in a change of the transverse beam position x_P, with $\Delta x_P = -D\frac{\Delta B_{dip}}{B_{dip}}$, where D is the dispersion (see chapter 3.4). By tuning the magnets and horizontally shifting the projectile beam, the gas target is scanned (see figure 3.14). With increasing overlap of the stored ion beam with the gas target, the count rate R_{exp} on the recoil ion detector increases with

$$R_{exp} = \sigma_I N_t M f_0 = \sigma N_t I_P, \tag{3.16}$$

where σ_I is the cross section of processes ionizing the target atoms, M is the number of stored ions and f_0 is the revolution frequency, and $I_P = M f_0$ is the beam current. The number of stored ions M constantly decreases due to the limited lifetime of the ion beam. Therefore, R_{exp} has to be normalized with the count rate R_{BPM} on the Beam Profile Monitor, which also depends on M but is independent of the target thickness, and

$$\frac{R_{exp}}{R_{BPM}} \propto \int_0^l n_t ds \ . \tag{3.17}$$

The measured ratio $\frac{R_{exp}}{R_{BPM}}$ for a neon gas target is displayed in figure 3.14. The measured extension of the target beam in the direction transverse to the projectile beam is about 4 mm, and a correction for the ion beam size of about 1 mm results in a horizontal target extension of about 3 mm.

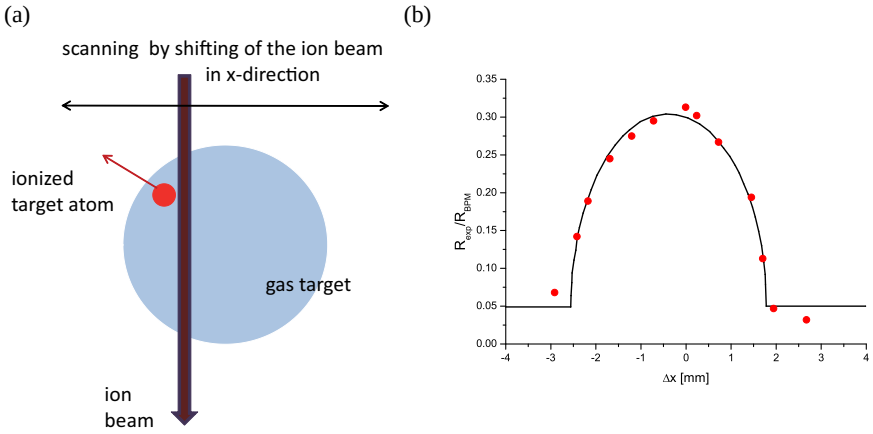

Figure 3.14: (a) To scan the thickness of the target jet, the projectile beam position is varied horizontally . The number of atoms ionized in the target is proportional to the target thickness, and to the count rate R_{exp} on the ion detector. The frequency f_0 is changing with the beam position, which influences the measured count rate. For normalization, the ratio R_{exp}/R_{BPM} of the count rate on the ion detector to the count rate on the BPM is considered. In (b), this ratio is plotted over the horizontal offset Δx of the projectile beam.

When a circular cross section of the target beam with a radius r_T is assumed, it is expected that the target thickness can be expressed by a hyperbolic function, $\frac{R_{exp}}{R_{BPM}} \propto \sqrt{r_T^2 - (x_P - x_{P0})^2}$. In figure 3.14, this hyperbolic fit is added to the measured data, and very good agreement is found.

The total lifetime T_g of the projectile beam which passes a gas target is a result of the life time limitation due to the background atoms in the TSR and the life time limitation due to the interaction with the gas target:

$$\frac{1}{T_g} = \frac{1}{T_t} + \frac{1}{T_b}, \tag{3.18}$$

where T_b is the lifetime of a stored ion beam which does not cross the target beam. For the measurement of T_b the ion beam is shifted to the outside of the target beam. T_t would be the lifetime of a ion beam which exclusively interacts with the target. From measurements of T_b and T_g, T_t can be calculated and the target thickness N_t is obtained by

$$\frac{1}{T_t} = N_t \sigma_{cap} f_0 \ . \tag{3.19}$$

A measurement of a Neon gas target was performed with a $^{12}C^{6+}$ ion beam of 50 MeV energy, which corresponds to $f_0 = 510\,\text{kHz}$. The electron capture cross section for C^{6+}+Ne collisions at this energy is $\sigma_{cap} \approx 5.5 \cdot 10^{-19} cm^2$. The measured lifetimes were $T_b = 197\,\text{s}$ and $T_g = 184\,\text{s}$, resulting in $T_t = 2788\,\text{s}$ and $N_t = 1.3 \cdot 10^9 \frac{1}{\text{cm}^2}$. Assuming an target extension of about 3 mm in the beam direction, a target density of

$$n_t = 4.3 \cdot 10^9 \frac{1}{\text{cm}^3}$$

is calculated.
However, the target density strongly depends on the operation parameters of the gas jet (especially on the pre-pressure). For the helium target a typical density about one order of magnitude higher was estimated by measuring the impact pressure in the beam dump.

4 Elements of atomic collision theory

There are various theoretical methods for studying atomic collisions, which can be subdivided in perturbative and non-perturbative methods. The latter ones include, for instance, different coupled-channel approaches, numerical solutions of the corresponding Schrödinger equations on a grid, and exterior complex scaling methods. There exist also different perturbative methods, which are normally applied when the interaction between the colliding subsystems is relatively weak. In what follows in this sections, some of the perturbative methods shall be briefly discuss.

4.1 The transition amplitude

We start with deriving general expressions for the transition amplitude. Let us consider a quantum system which is characterized by the state vector Ψ_i^+. This state describes the development of the system forward in time from its asymptotic (at $t \to -\infty$) state Φ_i. According to the basics of quantum mechanics, the amplitude for the transition of the system from the initial state Φ_i to its final (at $t \to +\infty$) state Φ'_f is given by

$$A_{fi} = \lim_{t\to\infty} \langle \Phi'_f | \Psi_i^+ \rangle \ . \tag{4.1}$$

One has to mention, however, that it can be quite difficult to calculate the transition amplitude using the above formula. An expression for the transition amplitude, which is often more convenient in practical calculations, can be obtained as follows. Using the identity

$$\int_{-\infty}^{\infty} dt \frac{d}{dt} \langle \Phi'_f | \Psi_i^+ \rangle = \langle \Phi'_f | \Psi_i^+ \rangle |_{-\infty}^{\infty} \tag{4.2}$$

$$= \lim_{t\to\infty} \langle \Phi'_f | \Psi_i^+ \rangle - \lim_{t\to-\infty} \langle \Phi'_f | \Psi_i^+ \rangle \tag{4.3}$$

and assuming that the initial and final asymptotic states are orthogonal to each other,

$$\lim_{t\to-\infty} \langle \Phi'_f | \Psi_i^+ \rangle = 0 \, , \tag{4.4}$$

the transition amplitude can be rewritten as

$$A_{fi} = \int_{-\infty}^{\infty} dt \frac{d}{dt} \langle \Phi'_f | \Psi_i^+ \rangle \ . \tag{4.5}$$

Ψ_i^+ is a solution of the full Schrödinger equation

$$i\frac{\partial}{\partial t}\Psi_i^+ = H\Psi_i^+ \, , \tag{4.6}$$

where H is the total Hamiltonian of our system. On the other hand, the asymptotic state Φ'_f is a solution of the equation

$$i\frac{\partial}{\partial t}\Phi'_f = H'_0\Phi'_f \, , \tag{4.7}$$

where H'_0 is the Hamiltonian for the final asymptotic channel.
Replacing in expression (4.5) the time derivatives with the corresponding parts on the righthand side of equations (4.6) and (4.7), we obtain

$$\begin{aligned} A_{fi} &= -i \int_{-\infty}^{\infty} dt \, \langle \Phi'_f | (H - H'_0) | \Psi_i^+ \rangle \\ &= -i \int_{-\infty}^{\infty} dt \, \langle \Phi'_f | V' | \Psi_i^+ \rangle \ , \end{aligned} \tag{4.8}$$

where V' is that part of the total Hamiltonian H which is not included in the definition of the state Φ'_f. If H and H'_0 do not depend explicitly on time, the only time-dependence of the corresponding state vectors Ψ_i^+ and Φ'_f is contained in the exponential factors, i.e.

$$\begin{aligned} |\Psi_i^+\rangle &= e^{-iE_i t} |\psi_i\rangle \\ |\Phi'_f\rangle &= e^{-iE_f t} |\phi'_f\rangle \ . \end{aligned} \tag{4.9}$$

where E_i and E_f are the initial and final energies and ψ_i and ϕ'_f are time-independent. Then one can easily perform the integration over time in equation (4.8) and obtain

$$A_{fi} = -2\pi i T^{fi} \delta(E_f - E_i), \tag{4.10}$$

where

$$T_{fi} = \langle \phi'_f | V' | \psi_i^+ \rangle \tag{4.11}$$

is the T-matrix and the δ-function in (4.10) describes the energy conservation in the transition process.
Note that the amplitude (4.10) and the T-matrix (4.11) are given in the so called post-form. The prior-form for these quantities is obtained by considering the state $\Psi_f^-(t)$ which develops from the state Φ'_f backwards in time and projecting it on the initial state Φ_i:

$$A_{fi} = \lim_{t \to -\infty} \langle \Psi_f^- | \Phi_i \rangle \ , \tag{4.12}$$

Starting with equation (4.12) and following the lines similar to those which were used to derive the post-form expressions, one can show that in the prior-form one has

$$A_{fi} = -2\pi i T^{if} \delta(E_f - E_i) \ . \tag{4.13}$$

In this expression,

$$T_{fi} = \langle \psi_f^- | V | \phi_i \rangle \ , \tag{4.14}$$

where ψ_f^- and ϕ_i are the time-independent parts of the vectors Ψ_f and Φ_i, respectively, and V is that part of the total Hamiltonian which is not included in the state Φ_i.
The equations (4.10)-(4.11) and (4.13)-(4.14)) present formally exact expressions for the post and prior transition amplitudes and are equivalent. In practice, since the exact form of the states Ψ_i^+ and Φ_f is as a rule not known, one has to use some approximations for them. As a result, the calculated transition amplitude becomes not exact, and the equivalence of the post and prior form may be violated. The main problem is posed by finding a suitable approximation for the states of the complete system. An analytical calculation is impossible already for simple collision systems including a hydrogen target, and many approximation methods have been developed.

4.2 The Born approximation

From the Schrödinger equation $(E - H)|\psi\rangle = 0$ and $H = H_0 + V$ it follows that

$$(E - H_0)|\psi\rangle = V|\psi\rangle \ . \tag{4.15}$$

The formal solutions of this equation is given by

$$\begin{aligned} |\psi^{\pm}\rangle &= |\phi\rangle + \lim_{\epsilon\to 0} \frac{1}{E - H_0 \pm i\epsilon} V |\psi^{\pm}\rangle \\ &= |\phi\rangle + G_0^{\pm} V |\psi^{\pm}\rangle \end{aligned} \tag{4.16}$$

with the free Green operator

$$G_0^{\pm} = \lim_{\epsilon\to 0} \frac{1}{E - H_0 \pm i\epsilon} \ . \tag{4.17}$$

When there is no perturbation, $V = 0$, the eigenstate $|\psi^{\pm}\rangle$ of the complete Hamilton operator H is equal to $|\phi\rangle$. When $V \neq 0$ but small, one can solve the Lippmann-Schwinger-equation (4.16) by iterations:

$$\begin{aligned} |\psi_i^{(0)+}\rangle &= |\phi_i\rangle \\ |\psi_i^{(1)+}\rangle &= |\phi_i\rangle + G_0^{+} V |\phi_i\rangle \\ |\psi_i^{(2)+}\rangle &= |\phi_i\rangle + G_0^{+} V |\phi_i\rangle + G_0^{+} V G_0^{+} V |\phi_i\rangle \\ |\psi_i^{(3)+}\rangle &= ... \end{aligned} \tag{4.18}$$

Using this iteration for obtaining, for example, the post-form of the T-matrix (4.11) one can get

$$T_{fi} = \langle\phi_f'|V|\phi_i\rangle + \langle\phi_f'|VG_0^{+}V|\phi_i\rangle + \langle\phi_f'|VG_0^{+}VG_0^{+}V'|\phi_i\rangle + \ . \tag{4.19}$$

From here, the transition matrix element A_{fi} and thereby the cross section ot the transition can be obtained. The iteration is proceeding in a power series of V and is expected to converge for sufficiently small V, i.e. for small perturbations. In case when the potential V describes the interaction between the undistorted projectile and target subsystems, the expression (4.19) represents the so called Born series.

In an illustrative example of a collision between a proton (projectile) and a hydrogen atom (target), this interaction V can be subdivided into two parts, $V = V_1 + V_2$, where V_1 is the interaction between the projectile and the target nucleus, and V_2 the interaction between the projectile and the target electron. Keeping only the first term of the expansion (4.19), which corresponds to the calculation in the first Born approximation, yields

$$T_{1B}^{fi} = \langle\phi_f'|V|\phi_i\rangle \, . \tag{4.20}$$

In the example under consideration, that is

$$T_{1B}^{fi} = \langle \phi'_f | V_1 | \phi_i \rangle + \langle \phi'_f | V_2 | \phi_i \rangle \,. \tag{4.21}$$

The above expression shows that the transitions happen either by a single interaction between the projectile and target nucleus or by a single interaction between the projectile and the target electron.
The first Born approximation is not always sufficient, especially for higher perturbations. In such a case one can try to improve the treatment by considering also the second term in the series (4.19),

$$T_{2B}^{fi} = \langle \phi'_f | V G_0^+ V' | \phi_i \rangle \;\; ... \tag{4.22}$$

In our case, when $V = V_1 + V_2$, it follows that

$$\begin{aligned} T_{2B}^{fi} &= \langle \phi'_f | (V_1 + V_2) G_0^+ (V_1 + V_2) | \phi_i \rangle \\ &= \langle \phi'_f | V_1 G_0^+ V_1 + V_2 G_0^+ V_1 + V_1 G_0^+ V_2 + V_2 G_0^+ V_2) | \phi_i \rangle \;\; . \end{aligned} \tag{4.23}$$

The first term in this expression describes the transition which happens due to the projectile interacting twice with the target nucleus. The next two terms correspond to the transition caused by the interaction between the projectile and the target nucleus and the target electron. The last term describes the case when the projectile interacts twice with the electron. Between the interaction, the projectile and the target are propagating freely, which is described by the Green operator G_0^+.

4.2.1 Single ionization in the first Born approximation

In case of a target atom with l electrons, the Hamilton operator can be written as

$$H = H_0 + V = H_P + H_T + V \tag{4.24}$$

with

$$V = \frac{Z_P Z_T}{R} - \sum_l \frac{Z_P}{|\mathbf{R} - \mathbf{r}_l|} \;, \tag{4.25}$$

where Z_P and Z_T are the charge states of the projectile ion and the target nucleus, R is the internuclear distance, $\mathbf{R}$ is the position of the projectile ion and $\mathbf{r}_l$ are the positions of the target electrons. In the case of single ionization, the Hamilton operator in the final state can

be separated into the same target and projectile systems as in the initial state, and $H_0 = H_0'$ and $V = V'$. When $|\varphi^{i,f}\rangle$ is the initial and final sate of the target system, respectively, and the projectile with momentum $\mathbf{p}_p^{i,f}$ is described by a plane wave, the eigenstates of the unperturbed system before and after the collision are given by

$$|\phi^{i,f}\rangle = |\varphi^{i,f}, \mathbf{p}_p^{i,f}\rangle = (2\pi)^{-3/2} e^{i\mathbf{p}_p^{i,f}\mathbf{R}} |\varphi^{i,f}\rangle \ . \tag{4.26}$$

Inserting these states into equation (4.20) gives the T-matrix $T_{1B,SI}^{fi}$ for single ionization in the first Born approximation for single ionization,

$$T_{1B,SI}^{fi} = \frac{1}{(2\pi)^3} \int d^3\mathbf{R} d^3\mathbf{r} e^{i(\mathbf{p}_p^i - \mathbf{p}_p^f)\mathbf{R}} \varphi_f(\mathbf{r}) \left(\frac{Z_P Z_T}{R} - \sum_l \frac{Z_P}{|\mathbf{R} - \mathbf{r}_l|} \right) \varphi_i(\mathbf{r}) \ . \tag{4.27}$$

With the momentum transfer $\mathbf{q} = \mathbf{P}_P^i - \mathbf{P}_P^f$ an integration over $\mathbf{R}$ results in

$$T_{1B,SI}^{fi} = \frac{Z_P}{2\pi^2 q^2} \left\langle \varphi_f \left| Z_T - \sum_l e^{i\mathbf{q}\mathbf{r}_l} \right| \varphi_i \right\rangle \ . \tag{4.28}$$

The initial and the final state of the target system $|\varphi^{i,f}\rangle$ are both eigenstates of the Hamilton operator H_T which have to be orthogonal, and equation (4.28) simplifies to

$$T_{1B,SI}^{fi} = \frac{Z_P}{2\pi^2 q^2} \left\langle \varphi_f \left| \sum_l e^{i\mathbf{q}\mathbf{r}_l} \right| \varphi_i \right\rangle \ . \tag{4.29}$$

With that equation, the T-matrix of the transition can be calculated for a known initial bound state φ_i and final continuum state φ_f of the unperturbed target system. For the hydrogen atom the exact description of these states is known, the initial state is the 1s-state φ_{1s}^H, and the final state is given by a Coulomb-wave. In the case of target atoms with more than one electron, it is a common approach to consider the target to be hydrogen-like, and assume an effective charge $Z_{T,eff}$. The charge of the projectile ions appears only in the prefactor of equation (4.28), and from $\sigma_{i\to f} = |T^{fi}|^2$ it follows that $\sigma_{i\to f} \propto Z_P^2$. Therefore, the cross section in the first Born approximation is independent of the sign of the projectile charge.
Second order contributions are added in form of the T-matrix T_{2B}^{fi} in the second Born approximation. As $T_{2B,SI}^{fi} \propto Z_P^2$, the cross section for single ionization is

$$\sigma_{i\to f} \propto |T_{1B,SI}^{fi} + T_{2B,SI}^{fi}|^2 = \alpha_1^{fi} Z_P^2 + \alpha_2^{fi} Z_P^3 + \alpha_3^{fi} Z_P^4 \ , \tag{4.30}$$

where the coefficients α^{fi} derive from the calculations of $T^{fi}_{1B,SI}$ and $T^{fi}_{2B,SI}$. The Z_P^3-term originates from interferences between the first and second order processes and the cross section now depends on the sign of the projectile charge.

4.2.2 Electron capture in the Oppenheimer-Brinkman-Kramers approximation

In the final state of electron capture processes, the electron is in a bound state of the projectile ion, and therefore $H_0' \neq H_0$. The perturbation in the final state is posed by the target ion, and

$$V' = +\frac{Z_P Z_T}{R} - \frac{Z_T}{r} \ . \tag{4.31}$$

For electron capture, the first term in equation (4.28), which represents the nuclear-nuclear interaction, does not vanish, because now the initial and the final unperturbed states are not necessarily orthogonal.[1] For high projectile velocities, the trajectory of the projectile ion is not altered significantly by the repulsive nuclear-nuclear interaction. The scattering angle is very small, usually smaller than 10^{-4} rad. The probability for the projectile to capture a target electron is hardly influenced by that slight change of trajectory, and therefore the effect of the nuclear-nuclear interaction on the total cross section is negligible (but plays an important role in the derivation of cross sections differential in scattering angle).

In the Oppenheimer-Brinkman-Kramers (OBK) approximation [Opp28, BK30], the nuclear-nuclear interaction is neglected, and the corresponding T-matrix in the first approximation reads

$$T^{fi}_{OBK} = \langle \phi_f' | - \frac{Z_T}{r} | \phi_i \rangle \ , \tag{4.32}$$

where ϕ_i describes the incident projectile and the electron bound in the target, and ϕ_f corresponds to the outgoing projectile carrying away the captured electron. Performing a calculation with expression (4.32), one can show that for asymptomatically high projectile velocities ($v_P \gg Z_T$, $v_P \gg Z_P$), the cross section for capture from the target ground ($1s$) state into states of the projectile with a principal quantum number n, reads [MC70, Opp28]

$$\sigma_{OBK}(1s \to n) \underset{v_p \to \infty}{\sim} \frac{2^{18}(Z_P Z_T)^5}{5 n^3 v_p^{12}} \ . \tag{4.33}$$

The OBK approximated predicts that the dependence of the capture cross section on the projectile charge is higher than that of the cross section for single ionization. Note that the result

[1] They are not solutions of the same Hamilton operator, as they are in single ionization processes.

obtained in the OBK approximation turned out to be not very accurate: even at very high velocities, it still significantly overestimates the experimentally measured capture cross sections.

4.3 Distorted wave calculations

In the Born approximation, the perturbative expansion is made using the undistorted states of the projectile and the target subsystems. This becomes a very serious shortcoming when the projectile-target interaction is not small. For instance, when the projectile ion has high charge or low velocity, the Born approximation does not converge or converges only slowly, and becomes impractical. In such a case, distorted wave approaches represent a good alternative. The basic idea of these approaches is to build a perturbative expansion based not on free states of the projectile and target subsystems, but on so called distorted states of these subsystems, which already partially include the interaction between the projectile and the target.
Here, the Hamilton operator of the complete system is written

$$H = H_0 + U + W \tag{4.34}$$

$$= H_0' + U' + W' \ , \tag{4.35}$$

where U (U') is the distortion potential for the initial (final) reaction channel and W (W') are the corresponding remaining perturbations. By a suitable choice of the distortion potentials W (W') the residual perturbations can be made much smaller than the perturbations which appear in the Born approximation. The eigenstates of the complete system are

$$(H_0 + U + W)\,|\psi_i^+\rangle = E\,|\psi_i^+\rangle \tag{4.36}$$

and

$$(H_0' + U' + W')\,|\psi_f^-\rangle = E\,|\psi_f^-\rangle \ . \tag{4.37}$$

In the initial state and final state, the Hamilton operators are

$$H = H_0 + U \ \text{ and} \tag{4.38}$$

$$H = H_0' + U' \ , \tag{4.39}$$

respectively, and the distorted eigenstates are

$$(H_0 + U)\,|\chi_i^+\rangle = E\,|\chi_i^+\rangle \quad \text{and} \tag{4.40}$$

$$(H_0' + U')\,|\chi_f^-\rangle = E\,|\chi_f^-\rangle \ . \tag{4.41}$$

The post form of the T-matrix is given by

$$T^{fi} = \langle\chi_f^-|W'^{\dagger}|\psi_i^+\rangle + \langle\chi_f^-|V - W'^{\dagger}|\phi_i\rangle \ , \tag{4.42}$$

as can be found in [MC70]. The contribution of the second term is usually very small, and it is neglected in most calculations. $|\psi_i^+\rangle$ can be approached iteratively in orders of the perturbation W' from the unperturbed state $|\chi_i^+\rangle$. In the first order, the resulting T-matrix reads

$$T_{fi} = \langle\chi_f^-|W'^{\dagger}|\chi_i^+\rangle \ . \tag{4.43}$$

This equation contains the distorted initial and final states $|\chi_i^+\rangle$ and $|\chi_f^-\rangle$, and the perturbation potential W'. There are two ways to approach the problem posed here. In order calculate with (4.43), one needs to know the distorted states and the perturbation W'. Either the distortion potential U is defined and the states $|\chi_i^+\rangle$ and $|\chi_f^-\rangle$ are obtained from equations (4.40) and (4.41), or the states $|\chi_i^+\rangle$ and $|\chi_f^-\rangle$ are defined directly. To obtain the T-matrix from equation (4.43), it has to be known how the perturbation operator W' acts on the state $|\chi_f^-\rangle$. From equation (4.41), it can be derived that

$$W'\,|\chi_f^-\rangle = (H_0' + U' + W' - E)\,|\chi_f^-\rangle = (H - E)\,|\chi_f^-\rangle \ . \tag{4.44}$$

After that transformation, the separation of V' into U' and W' does not have to be known. The challenge is to find the expressions for $|\chi_i^+\rangle$ and $|\chi_f^-\rangle$ which give the best results.
Among the distorted wave models which are frequently used in atomic collision physics are the continuum-distorted-wave (CDW) approximation [Che64] and closely related to it continuum-distorted-wave-eikonal-initial-state (CDW-EIS) [CM83] and symmetric eikonal (SE) approximations [MR84].

4.4 Semi-classical approximation

Up to now, we were treating all the particles constituting the projectile and target subsystems quantum-mechanically. However, masses of the nuclei are orders of magnitude larger than the electron mass, taking this fact into account, a so called semi-classical approximation is often

used for considering ion-atom collisions. In this approximation, only electrons are described as quantum particles while the nuclei are considered classically. It is also assumed that in the collision these heavy particles move along given classical trajectories. In such an approach the electrons move in external time-dependent fields generated by the heavy particles. The potentials in the corresponding time-dependent Schrödinger equation explicitly depend on time and the energy of the electronic subsystem is not conserved.
In the semi-classical approximation, the post-form of the transition amplitude is given by an expression which is formally very similar to equation (4.8),

$$A_{fi} = -i \int_{-\infty}^{\infty} dt \, \langle \Phi'_f | V' | \Psi_i^+ \rangle \ . \tag{4.45}$$

The meaning of Φ'_f, Ψ_i^+, and V' however, is now different. Namely, Ψ_i^+ is the solution of the full Schrödinger equation for the electrons and Φ'_f is the state describing the electron in the final channel in which the interaction V' is not taken into account. A similar expression holds for the prior-form of the transition amplitude. Since, as was already mentioned, the interactions in the semi-classical approximation are explicitly time-dependent, the dependence of the states Φ'_f and Ψ_i^+ on time is no longer given by simple exponential factors and the integration over time in equation (4.45) can not be performed so easily as in the full quantum treatment.

4.4.1 A simple model for transfer ionization at asymptotic high collision velocities

In the context of this work, the transfer ionization process in which one of the target electron is captured and another one is emitted, is of special interest. Different mechanisms contribute to this process (see section 2.5). One mechanism for transfer ionization, the electron-electron transfer ionization (eeTI) process, was proposed only recently [VNU08] and could be confirmed experimentally in the data presented in chapter 5.
In this mechanism, the electron-electron interaction plays a crucial role and it dominates the transfer ionization process at sufficiently high collision velocities and low charged projectiles. The simplest theoretical treatment of the eeTI process starts with the approximate transition amplitude

$$A_{fi} = -i \int_{-\infty}^{\infty} dt \, \langle \Psi_f(t) | V' | \Psi_i(t) \rangle \ , \tag{4.46}$$

where V' in this case is the Coulomb interaction between the electrons and $\Psi_i(t)$ and $\Psi_f(t)$ are the initial and final undistorted electron states. The coordinates of the two electrons with respect to the target nucleus are $\mathbf{r}_1$ and $\mathbf{r}_2$. The projectile nucleus moves along a straight line trajectory $\mathbf{R}(t) = \mathbf{b} + \mathbf{v}_P(t)$, where $\mathbf{b}$ is the impact parameter. With respect to the projectile nucleus, the electron coordinates are $\mathbf{s}_1 = \mathbf{r}_1 - \mathbf{R}(t)$ and $\mathbf{s}_2 = \mathbf{r}_2 - \mathbf{R}(t)$.
In an OBK-like treatment, the initial and final two electron states are approximated by

$$\Psi_i(t) = \varphi_i(\mathbf{r}_1, \mathbf{r}_2) e^{-iE_i t} \tag{4.47}$$

and

$$\Psi_f(t) = \frac{1}{\sqrt{2}} \left[\chi_f(\mathbf{s}_1) e^{iv_P \mathbf{r}_1} \phi_f(\mathbf{r}_2) + \chi_f(\mathbf{s}_2) e^{iv_P \mathbf{r}_2} \phi_f(\mathbf{r}_1) \right] \cdot e^{-i(E_{f,1}+E_{f,2})t} \cdot e^{-i\frac{v_P^2}{2}t} \ . \tag{4.48}$$

In this expressions, φ_i is the unperturbed two-electron atomic state with the internal energy E_i. Further, ϕ_f describes the emitted electron, which moves in the field of the recoil target ion with the energy $E_{f,1}$, χ_f is a bound state of the electron captured by the projectile, with has the internal energy $E_{f,2}$, and $e^{iv_P \mathbf{r}_j - i\frac{v_P^2}{2}t}$ is the so called translational factor. Considering capture from a helium target, the initial unperturbed atomic state is expressed by [VNU08]

$$\varphi_i(\mathbf{r}_1, \mathbf{r}_2) = A_i \left(e^{-\alpha r_1 - \beta r_2} + e^{-\alpha r_2 - \beta r_1} \right) e^{\gamma r_{12}} \ , \tag{4.49}$$

with the electron-electron distance $r_{12} = |\mathbf{r}_1 - \mathbf{r}_2|$. A_i is a normalization factor, and the parameters α, β and γ allow for an adjustment of the state. A complete ignorance of any electron-electron interaction in the initial atomic state would further lead to $\alpha = \beta = 2$, because in such an approximation each electron would see the full, unshielded charge of the target nucleus. Quite a good approximation for the initial atomic state can be obtained by setting $\alpha = 2.21$, $\beta = 1.44$ and $\gamma = 0.207$.
In the high velocity limit ($v_P \to \infty$), the eeTI cross section is given by

$$\sigma_{eeTI} \underset{v_P \to \infty}{\propto} \frac{Z_P^5 Z_T^3}{v_P^{12}} \ . \tag{4.50}$$

The OBK-like approximation does not represent the best choice for the eeTI mechanism. Better results can be obtained by taking into account the distortion of the initial electronic state within the CDW model. This also enables one to combine in a unified treatment the eeTI and the Thomas TI mechanisms.

To conclude our brief discussion of transfer ionization, one can note the following: At higher perturbations, the total TI cross section is dominated by the independent TI process. In the latter, one of the target electrons is ionized and another one is captured in two subsequent, "independent" interactions with the projectile ion. In a theoretical consideration, the cross sections for the single capture and the single ionization events can be calculated separately, and the final amplitude of the TI process is obtained by a multiplication of the transition amplitudes of the single processes in the impact parameter space.

5 Transfer ionization in collisions of O^{7+} and Li^{3+} with helium

In recent years, many experiments have focused on the investigation of atomic collision processes with two active electrons, e.g. double ionization (e.g. [SCK+09, SMS+00, FMD+03, DKS+01]), double capture (e.g. [SVB07, STJJ09]), and transfer ionization (e.g. [MDK+01, SJR+05]). These two-electron transitions are of special interest because they offer an access to the investigation of electron-electron correlations.
A comparison of the angular distribution of electron emission in single and double ionization revealed striking similarities [FSMU04], in so far as the angular distribution of the sum momentum of the two electrons emitted during double ionization shows a double lobe structure similar to single ionization (see figure 2.3).
In a transfer ionization (TI) process, only one target electron is emitted into the continuum. In that respect, the final state of TI bears a closer resemblance to the final state of single ionization than double ionization does. However, it turns out that the electron emission characteristics in TI strongly depends on the mechanism resulting in the ejection of the electron. Considering a two-step process, where one electron is captured and the other one ejected in separate, independent interactions with the projectile, one would expect strong similarities to single ionization. For correlated mechanisms, in contrast, such as the Thomas TI and the eeTI already discussed in chapter 2, the electron final momentum distribution is expected to strongly deviate from single ionization. Thus, transfer ionization is particularly suited to study the influence of electronic correlation.

5.1 O^{7+} on helium collisions

The transfer ionization process was investigated in collisions of O^{7+} projectile ions with helium target atoms. The projectile beam energy was 1 MeV/u, which corresponds to a velocity of $v_P = 6.3$ a.u.. The charged collision fragments are extracted by an electric field of about 5.5 V/cm, which results in full acceptance of electrons with a longitudinal momentum larger than -2 a.u., whereas a magnetic Helmholtz-field of about 15 G results in an acceptance of electrons with a

Shell	binding energy [eV]	binding energy [a.u.]	Q-value [a.u.]
K	739	27.2	24.3
L	171	6.3	3.4
M	75	2.8	-0.1
N	41	1.5	-1.4

Table 5.1: The binding energies of different shells in the O^{6+} ion are reflected in the Q-value of the transfer ionization process.

transverse momentum of up to 2 a.u.. The transverse momentum resolution for the recoil ions is about 0.3 - 0.4 a.u. (FWHM), the longitudinal resolution is ~ 0.15 a.u.
The charge changed projectiles are detected by a scintillation detector implemented in the TSR. Therefore, triple coincidences of charge-changed projectiles, He^{2+} recoil ions and electrons can be recorded, identifying the TI process.

5.1.1 The electron transfer characteristics

One of the active electrons in a TI collision is transferred to the projectile ion. As in single capture events, the capture into different states of the ion is possible. The different binding energies of these states result in different Q-values of the collision (see table 5.1).[1] In figure 5.1, the cross section is displayed as a function of the electron energy level in the final state (negative of the binding energy) and the transverse momentum transfer. Two clearly separated lines are visible. Capture into the L-shell is clearly separated from capture into higher shells of the oxygen projectile ion. Since the resolution should be nearly constant, the different widths of the two lines indicate that more than one transition contributes to the broader line. Indeed in the projection of the lines on the binding energy-axis, a shoulder on the broader peak appears, which indicates that the peak consists of two or even more overlapping peaks originating from capture into the M-shell and higher shells, which can not be resolved.
The transverse momentum distribution of the recoil ions is displayed in figure 5.1(b) for capture into the L-shell and for capture into higher shells. The capture into higher shells has larger contributions at small transverse momenta, which, crudely speaking, correspond to large impact parameters *b*. For capture into the L-shell, in contrast, the cross sections fall off significantly slower with increasing $P^f_{R\perp}$ indicating that here smaller *b* play a more important role.

[1] The sum of the binding energies of the two helium target electrons is 79 eV = 2.9 a.u..

(a) (b)

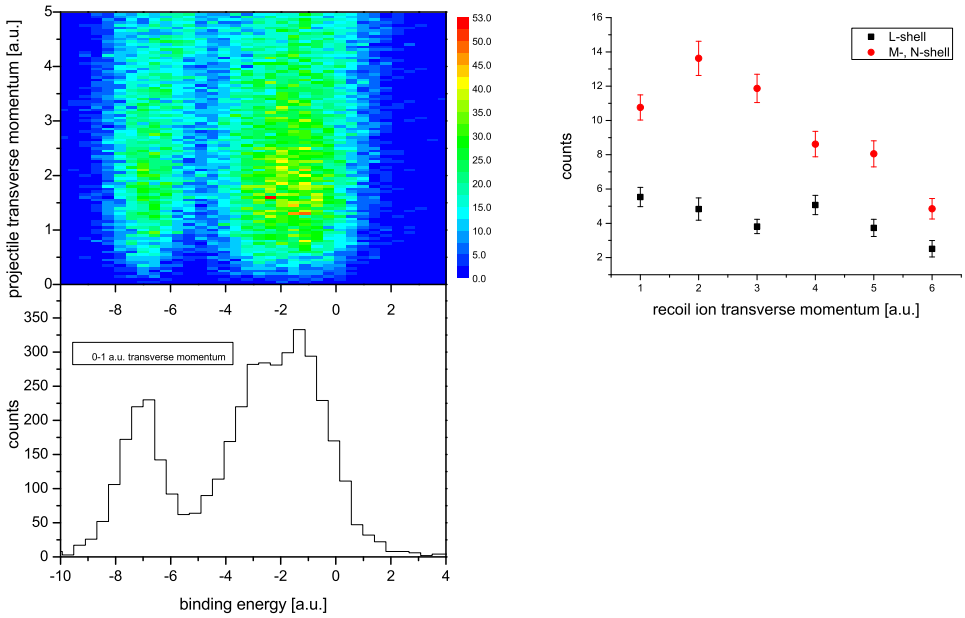

Figure 5.1: (a) The distribution of measured binding energies in the transfer ionization process. The smaller peak can be assigned to capture into the L-shell, the broader peak is a superposition of M-shell capture and capture into higher shells. The contribution of the L- shell capture and capture into higher shells changes with the transverse momentum transfer. (b) The distribution of the L-shell and higher shell cross section plotted against the transverse momentum transfer.

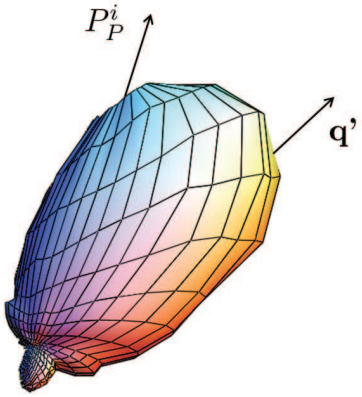

Figure 5.2: Three-dimensional angular distribution of the ejected electrons in transfer ionization of helium in 1 MeV/u O^{7+} on helium collisions. This plot represents an integration over all **q'** and electron energies. The arrow labelled **q'** schematically shows the direction of an average **q'**.

5.1.2 The electron emission characteristics

A three dimensional angular distribution of the electrons ejected in the TI process is shown in figure 5.2. The distribution bears a close resemblance to the SI process, as it displays a double lobe structure with a pronounced binary peak, i.e. a preferential emission of the electrons approximately in the direction of **q'**. Here, the final state momentum of the captured electron $\mathbf{P}^f_{e\,cap} = v_P$ is accounted for in the definition of $\mathbf{q'} = \mathbf{P}^f_R + \mathbf{P}^f_{e\,ion} + v_P$. Most electrons are emitted in the forward hemisphere due to the post-collision interaction (PCI) between the two nuclei. As the perturbation $\eta \approx 1.1$ is high, the independent TI is expected to be the clearly dominant TI process.

The correlated TI processes hardly contribute to the forward emission of the electrons. In the Thomas TI process, the electrons are ejected perpendicular to the projectile beam direction, and in the eeTI process, an emission mostly opposite to the beam direction is expected (see section 2.5). In figure 5.2, a small fraction of electrons is emitted backwards. It will be seen that this contribution can not directly be associated with the eeTI electron emission, as it might be due to the recoil peak occurring in the independent TI process.

5.1.3 The independent TI process

To further compare the independent TI and the SI process, the cross section as a function of the relative emission angle of the electron and the recoil ion in the plane transversal to the projec-

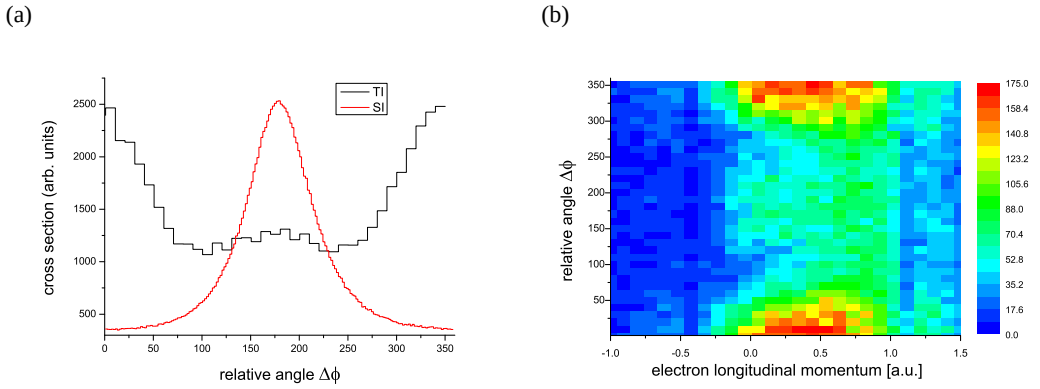

Figure 5.3: (a) Recoil ion and electron are ejected under the relative angle $\Delta\phi = \phi_R - \phi_e$ in the azimuthal plane, where large qualitative differences between single ionization and transfer ionization processes are observed. In SI processes, the back to back emission is strongly preferred, whereas in TI processes, the particles are mainly emitted under the same angle. (b) The distribution of $\Delta\phi$ over the longitudinal momentum of the electron. The lines of lower intensity at about $P^f_{e\|} \approx -0.4$ a.u. and ≈ 1.1 a.u. are due to the location of a wiggle at these momenta. At a wiggle position, no angular information on the electron can be obtained (see section 3.1).

tile beam direction (= the azimuthal plane) is studied, where large differences are noticed (see figure 5.3). In SI, the distribution of the relative azimuthal emission angle $\Delta\phi = \phi_R - \phi_e$ has a maximum at 180°, i.e. the recoil ion and the electron are emitted back to back with a strong preference. In contrast, the electrons in a TI process are predominantly ejected in the same direction as the recoil ion, with $\Delta\phi = 0° = 360°$, even though there is a smaller contribution at $\Delta\phi = 180°$.
In figure 5.3(b), $\Delta\phi$ is plotted against the longitudinal momentum of the emitted electron $P^f_{e\|}$. Independent of $\Delta\phi$ data occur almost exclusively at positive longitudinal momenta. When capture into the L-shell and capture into higher shells were considered separately, qualitatively the same spectra were obtained. As will be shown in the next section a very different behaviour is observed for the eeTI process.

To gain a better understanding of the collision dynamics, the experimental cross sections are compared to cross sections obtained by different theoretical approaches for TI (see chapter 4). In the independent TI process, the single ionization and the single capture (SC) process can be considered separately. The SC step is either calculated in the OBK or the CDW models. These approaches differ in so far as the distortion of the initial state by the projectile ion, and the distortion of the final state by the recoil ion are only considered in the CDW calculation. Accordingly, the SI step is modelled in the first Born approximation or in the CDW-EIS cal-

culation, where only the latter includes the distorting effect of the projectile ion on the target system. The nuclear-nuclear interaction can optionally be included.
The distribution of the relative angle $\Delta\phi$ and the longitudinal electron momenta $P_{e\|}$ is computed for all combinations of theoretical methods. The results are shown in figure 5.4. As the effect of the distortion or the nuclear-nuclear interaction is neglected in some models, a comparison of the calculated cross sections might give insight into which effects are mainly responsible for the distribution observed in the experiment.
The calculations are performed assuming capture into the 2p0 state of the oxygen projectile, which according to theory has the largest cross section of all L-shell states. Moreover, the shape of the spectra does not differ significantly when capture into other L-shell states is assumed.
The distortion effect in the capture channel can be observed by comparing the spectra obtained by OBK- and by CDW-calculations. The distortion effects tend to enhance the back to back emission of recoil ion and electron in the azimuthal plane even further, whereas they have little influence on the longitudinal electron momentum. Overall, the effect of the distortion is not very strong.
In contrast, the ionization step is much more sensitive to the distortion of the final electron state by the projectile ion. In the CDW-EIS calculation, this distortion pulls the electron in forward direction, and the positive longitudinal electron momentum increases. This effect is known as the post collision interaction (PCI).
Moreover, in the spectra where the nucleus-nucleus interaction is neglected, the distortion of the target system by the projectile ion in the SI process leads to a severe change in $\Delta\phi$. Now, the collision fragments are predominantly emitted in the same direction, $\Delta\phi = 0°$, which is in agreement with the experimental data. In the spectra including the nuclear-nuclear interaction, the opposite trend can be observed: Now significant contributions at $\Delta\phi = 180°$ are observed, although the maxima at $\Delta\phi = 0°, 360°$ remain stronger.
The most important component in theory for the qualitative reproduction of the measured data is apparently the effect of the post collision interaction on the ejected electron.
Overall, the most complete model including the CDW capture and the CDW-EIS single ionization, and the nuclear-nuclear interaction, is in good qualitative agreement with the measured data. The shift of the back to back emission of the collision fragments to slightly larger longitudinal electron momenta is reproduced, although this contribution is overestimated by the calculation.

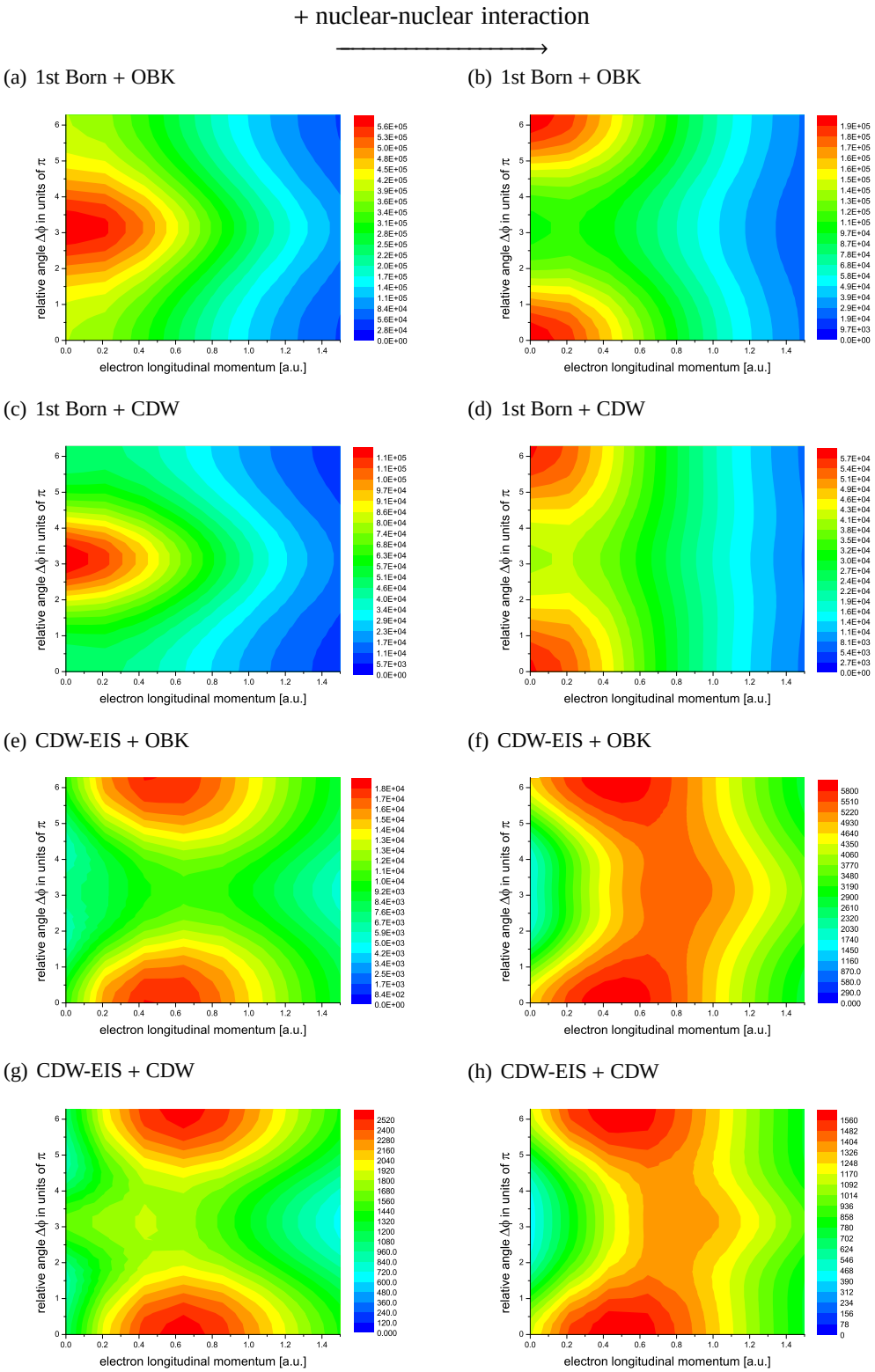

Figure 5.4: The distribution of the cross section over the longitudinal momentum of the ejected electron and the relative angle in the ejection of electron and recoil ion in independent transfer ionization processes of 1 MeV/u O^{7+} + He collisions is computed for different combinations of theoretical models. For details see text.

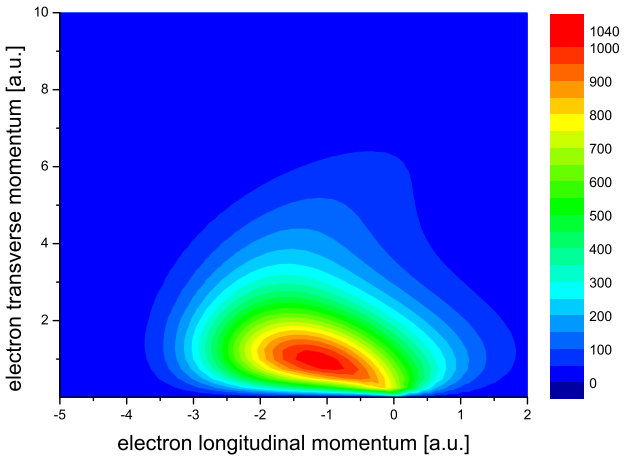

Figure 5.5: The final momentum distribution of electrons ejected in eeTI and Thomas TI processes in 0^{7+} on helium collisions with $v_P = 6.3$ a.u.. The contributions of the two correlated processes can not be separated.

5.1.4 Correlated transfer ionization processes

In the correlated TI processes, the projectile ion interacts only once with the target system, capturing an electron. The second target electron is ejected due to an electron-electron correlation. The Thomas TI and the newly proposed eeTI process are described in more detail in section 2.5.2. Briefly, in the Thomas TI, the electron is preferentially ejected transversal to the projectile beam direction, whereas in eeTI, electron emission is strongly focused backwards. Therefore, the two correlated processes can generally be distinguished in the final state momentum distribution of the ejected electrons (see figure 2.7 in section 2.5.2). But because of the large perturbation $\eta = 1.1$ of the collision system investigated here, according to theory the contributions of the two correlated TI mechanisms can no longer be separated in the momentum distribution, which is shown in figure 5.5. Here, the contributions from eeTI are dominant and the Thomas TI only shows up as a tail at large transverse momenta.

In the correlated processes, the target nucleus can be considered merely a passive bystander. The recoil ion momentum in the final state is small[2] compared to the large recoil ion momentum in independent TI processes. Therefore, in an attempt to extract the correlated TI events in the measured data, only events were considered with a recoil ion momentum < 3 a.u..
The distribution of the longitudinal electron momentum of these events is shown in figure 5.6.

[2] In section 4.3, it was described that the momentum resulting from the excess energy of the captured electron in the projectile frame is not transferred only to the second electron, but partly also to the recoil ion. That part increases with Z_T and decreases with increasing v_P, but it is always noticeably smaller than the energy transferred to the emitted electron.

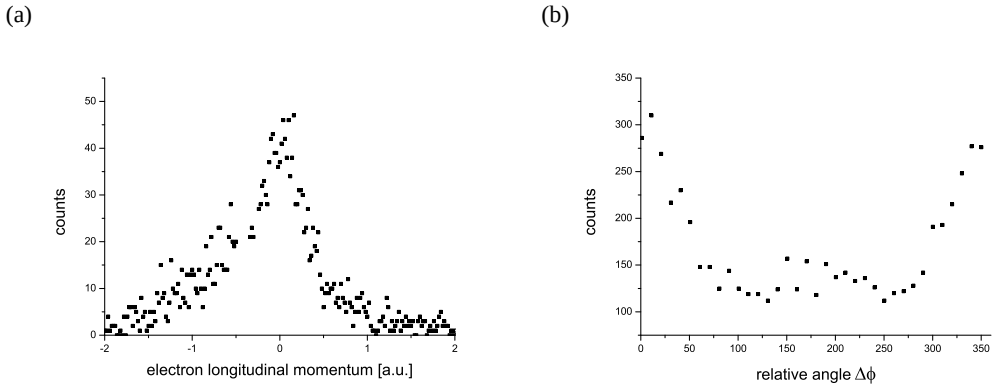

Figure 5.6: (a) The distribution of the longitudinal momentum of the ejected electrons in 100 MeV/u O7+ on He collisions, under the condition that $\mathbf{P}_R^f \leq 3$ a.u.. (b) The relative angle in the emission of electrons and recoil ions in the plane perpendicular to the projectile beam direction, under the same condition as (a).

There is clearly less contribution at positive electron momenta, the peak is at a longitudinal electron momentum of about 0 a.u., and there is a clear asymmetry favouring backward emission. A comparison with the theoretical calculation (figure 5.5) seems to suggest that the main contribution of the electrons from the correlated TI processes is expected in that range.
However, due to the kinematics of transfer ionization, the sum of the longitudinal momenta of recoil ion and electron is generally directed opposite to the projectile beam direction,

$$P_{R\|}^f + P_{e\|}^f = \frac{Q}{v_P} - \frac{v_P}{2} + \frac{E_e^f}{v_P} \ , \tag{5.1}$$

where $\frac{v_P}{2} = 3.16$ a.u. for the observed collision system. Therefore, the condition of small recoil ion momenta, $\mathbf{P}_R^f \leq 3$ a.u., artificially suppresses electrons with longitudinal momenta in the forward direction.
Moreover, the distribution of the relative angle $\Delta\phi$ in figure 5.6 displays roughly the same shape as for the data without a condition on the recoil momentum, compare figure 5.3, which is characteristic for uncorrelated processes (see section 5.1.3).
It can be concluded that no clear evidence for the presence of the eeTI process can be found in the O^{7+} data, although it can not be ruled out either. In any case it is safe to state that the contributions from correlated TI processes are very small compared to the uncorrelated process, as expected for this collision system.

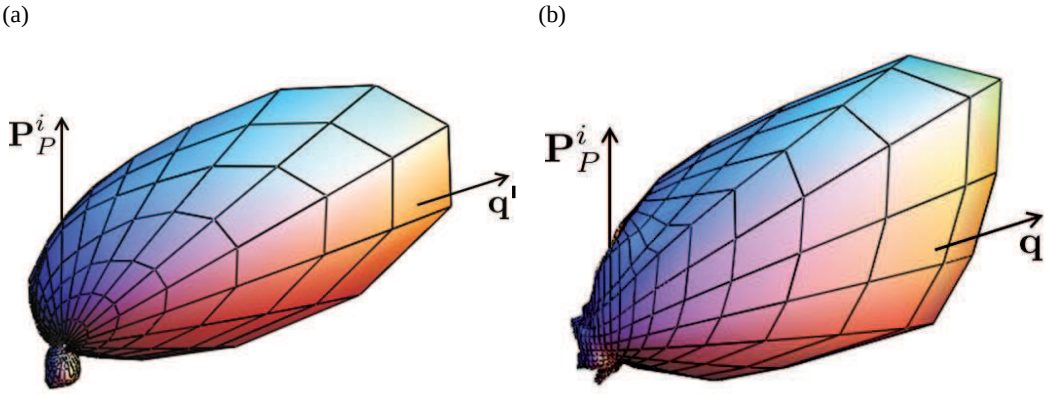

Figure 5.7: The calculated three dimensional angular distribution of the ejected electrons in 1 MeV/u Li^{3+} on helium collisions in (a) independent transfer ionization and (b) single ionization processes. Again, the plots represent an integration over all **q** or **q'** and electron energies.

5.2 Li^{3+} on helium collisions

To investigate correlated TI processes, a collision system with a smaller perturbation is chosen , i.e. a Li^{3+} projectile ion beam with an energy of 1 MeV/u, which corresponds to a perturbation of $\eta = \approx 0.5$ [SWG+12]. The collision fragments are guided onto the detectors by a electric field of about 18 V/cm and a magnetic field of 12 G. The rather high extraction voltage increases the acceptance of electrons with a large longitudinal momentum component in the backward direction, but restricts the recoil ion momentum resolution to 0.5 – 0.7 a.u.. The transversal electron momentum acceptance is about 2 a.u., and the electron momentum resolution is < 0.1 a.u. (FWHM). The TI events are identified by a true triple coincidence of an ejected electron, a doubly charged recoil ion and a detection of a charge-changed projectile ion.

Figure 5.7(a) shows the theoretical prediction of the three dimensional angular distribution of the electrons emitted via independent TI processes in Li^{3+} on He collisions.[3] As expected, it is very similar to the distribution calculated for SI events (figure 5.7(b)), which was calculated in the CDW-EIS model. In both plots a pronounced binary peak is visible.

In contrast, the three dimensional angular distribution in the experimental TI data (5.8(a)) displays a strong focusing of the elected electrons in the backward direction. There is only a relatively small binary peak visible. Because of theses severe discrepancies to the theoretical prediction for the independent TI process, the experimental data suggests that the independent

[3]The SI step is calculated with the CDW-EIS approach, the SC step with the CDW approach. The transition amplitudes of the two steps are convoluted to obtain the TI cross section. The nuclear-nuclear interaction is included by means of the eikonal phase.

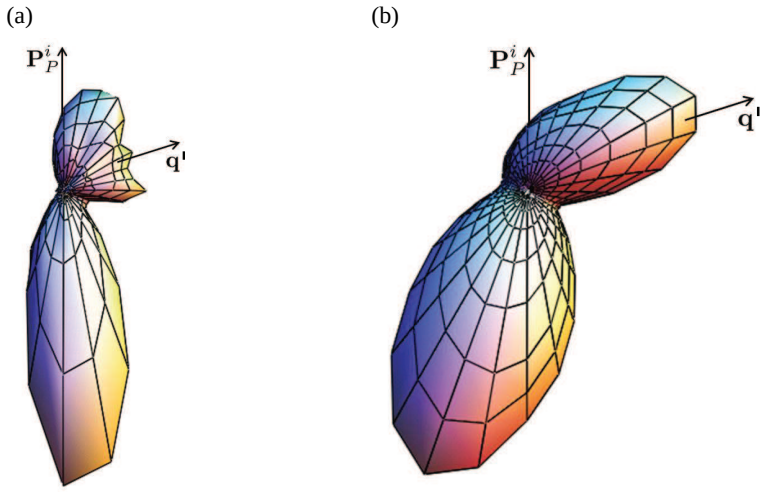

Figure 5.8: (a) The measured three dimensional angular distribution of the ejected electrons in 1 MeV/u Li^{3+} on helium collisions in transfer ionization processes. The data is integrated over all **q**, the arrow indicates an average momentum. (b) The calculated three dimensional angular distribution with incoherently added contributions of independent TI and eeTI.

TI process is not the main contribution to the TI cross section.

Of the correlated TI processes, neither the shake-off nor the Thomas process exhibits such a pronounced ejection of the electron opposite to the projectile beam direction. Also, their contribution to the total TI cross section at the present perturbation $\eta = 0.5$ is assumed to be very small. The emission of the electron in the direction of $-P_P^i$ is a clear signature of the eeTI process.

In another theoretical model [Voi08], the contribution from the eeTI is calculated and added incoherently to the independent TI contribution. Figure 5.8(b) shows the resulting plot of the electron angular distribution. There is qualitatively good agreement between figures 5.8(a) and 5.8(b). The pronounced peak in the direction of $-P_P^i$ and the weak binary peak are reproduced by theory. Some small discrepancies can be observed. In the experimental data, the polar angle θ_e of the electron emission with respect to P_P^i is extremely small for the backwards peak, whereas it is about 25°in the theoretical model. Also, the theoretical model overestimates the binary peak.

The measured relative angle $\Delta\phi = \phi_R - \phi_e$ between the direction of the recoil ion and the ejected electron in the plane perpendicular to P_P^i is displayed in figure 5.9(a). The collision fragments are mainly emitted into the same direction for positive longitudinal electron momenta (which can be associated with the independent TI), whereas for the backwards electrons due to eeTI processes, back to back emission is preferred. This behaviour is well reproduced by theory (see

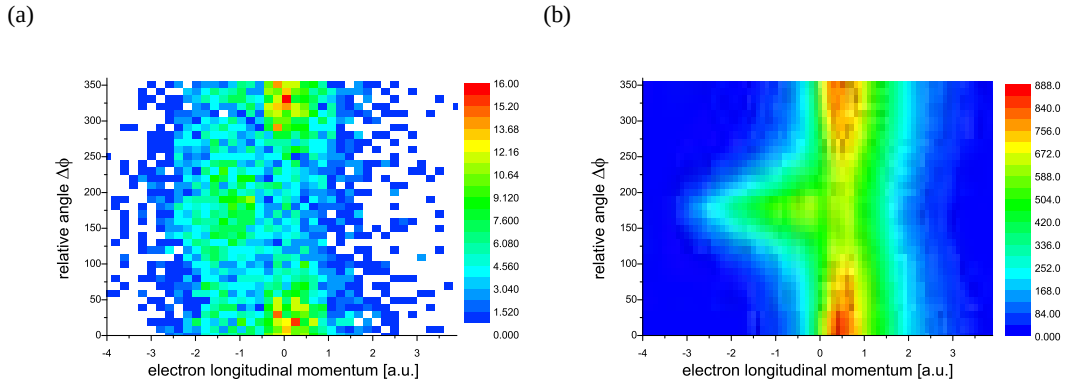

Figure 5.9: (a) The experimental distribution of the longitudinal electron momenta over the relative angle between the ejected electron and recoil ion in 1 MeV/u Li^{3+} on He collisions. (b) The theoretical distribution. In the model, the contribution of independent TI and eeTI are added incoherently. The graph is generated by a Monte Carlo event generator [SDN+07].

figure 5.9(b)).

5.3 Discussion

Transfer ionization processes were observed in O^{7+} and Li^{3+} collisions on neutral helium atoms. The collision energy was 1 MeV/u in both systems, resulting in perturbation parameters of $\eta = 1.1$ and 0.5, respectively. The independent TI process is found to clearly dominate at $\eta = 1.1$. A small fraction of electron was emitted in the backward hemisphere, but it could not unambiguously be associated with the eeTI process.

In the Li^{3+} on helium collision system, the eeTI process is found to be the main contribution to the total TI cross section, and could be clearly identified in the three dimensional angular distribution of the electron ejection. Thereby, the eeTI process was for the first time experimentally verified.

The relative angle of the collision fragments in the azimuthal plane could be reproduced by theory for both collision systems.

To further investigate the electron-electron correlation in transfer ionization processes, collisions of ions with more complex targets are of interest. Due to the different shells occupied in larger atoms, stronger and weaker electron-electron correlations could be observed in one collision system. Experiments on transfer ion ionization of a lithium target are currently under preparation [FGG+].

6 Charge transfer processes in Si^{14+} on helium collisions

6.1 Introduction

At large perturbations, electron transfer processes are usually quite important and can even become the dominant recoil ion production channel,[1] i.e. the capture cross section can exceed the cross section for target ionization. The understanding of electron capture processes is important in many fields of research [VMS+91, WAW+93, Mat95, Kal95], and because of their simple final state, they are an excellent test for theoretical models.
The non-radiative capture (NRC) cross section drops rapidly with increasing projectile velocity,[2] while radiative electron capture (REC) drops with a much smaller power. At very high projectile velocities, REC thereby becomes the dominant capture process. In the REC process, a target electron is captured by the projectile ion via the simultaneous emission of a photon. As REC can be thought of as the time inverse of photoionization, it is a very fundamental process and offers an access to the investigation of coupling of the charged particles to the radiation field. The photon emission in REC has been studied in some experiments, especially for capture into heavy ions like bare uranium (i.e. [SKM+95, SML+01]). The angular distribution of the emitted photons was studied (i.e. [SLB+99]), and light emitted in REC was found to be strongly polarized (see [SBF+04, SSB+07]).

In former studies, the REC photons were detected in coincidence with the charge-changed projectile ion, whereas the recoiling target ion was not detected. In our experiments, we attempted for the first time to detect the recoil ion in coincidence with both the photon and the projectile, and to obtain kinematically complete data on the REC process.
For that purpose, a photon detector was implemented into the Reaction Microscope (see section 3.2). It should be emphasized that this is an extremely challenging experiment due to the very

[1] However, in the studies discussed in this chapter we are far away from this scenario because of the large projectile velocity.
[2] with v_P^{-12} and v_P^{-11} for kinematic and Thomas capture, respectively

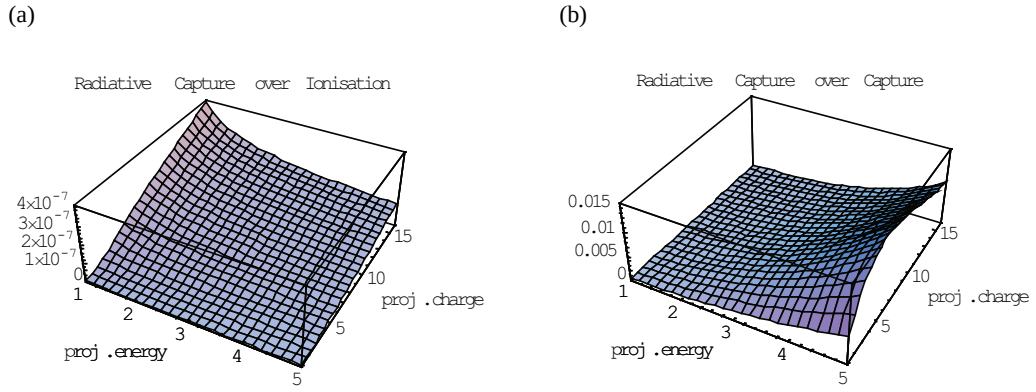

Figure 6.1: The cross section of radiative electron capture (REC) is small compared to other collision processes. (a) The ratio of the cross sections for REC and single ionization over a wide range of projectile charge states and energies in MeV/u. (b) The ratio of the cross section for REC and the total single capture cross section.

Process	Cross Section σ [cm^2]
Single Ionization	$1.2 \cdot 10^{-15}$
Single Capture	$4.8 \cdot 10^{-20}$
Radiative Electron Capture, K-shell	$3.0 \cdot 10^{-22}$
Radiative Electron Capture, L-shell	$2.4 \cdot 10^{-22}$
Radiative Electron Capture, M-shell	$6.6 \cdot 10^{-23}$

Table 6.1: The cross sections for different atomic processes in a $^{28}Si^{14+}$ collision on a helium target at a collision energy of 3.57 MeV/u.

small REC cross sections, that in our case are about 7 orders of magnitude smaller than those of competing target ionizing pathways. As will be detailed in the following, we indeed succeeded to observe triple and quadruple coincidences, including photons. However, due to the limited statistics and the high background it was not possible to unambiguously identify photons emitted in a REC process.

We observed charge transfer processes in the collision of 3.57 MeV/u $^{28}Si^{14+}$ projectile ions ($v_P \approx 12$ a.u.) on helium atoms. The collision fragments were extracted by an electric field of ≈ 14.5 V/cm. Due to the strong extraction field, the recoil ion momentum resolution was only about 0.5 a.u. (FWHM).

In order not to expose the recoil ion detector to the high rate of single ionization events, the

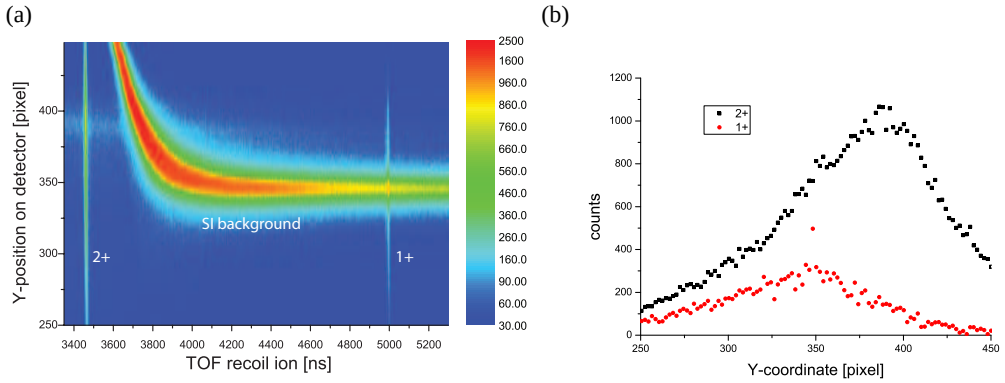

Figure 6.2: (a) The y-position on the detector, i.e. the vertical position of the recoil ion impact, is plotted against the time of flight of the recoil ion. The He^{1+} and He^{2+} recoil ions in time coincidence with a charge-changed projectiles can be seen as vertical lines. Suppression of background ions was achieved by a switching of the electric field in the drift region. (b) The expansion of the He^{1+} and He^{2+} contributions over the detector are similar in width. The detected He^{2+} ions outnumber the He^{1+} ions by a factor of ≈ 3.8.

potential of the drift region was switched: The lower part of the drift region was grounded, whereas the upper part was on a negative potential of -160V, causing the recoil ions to pass above the detector. The detection of a charge-changed projectile ion triggered a fast switch signal, which raised the lower voltage to -160V, and allowed the recoil ions to reach the detector (see figure 6.2). The recoil ions were thus recorded in a coincidence measurement with the charge-changed projectile ion. For transfer ionization processes, true triple coincidences of the charge-changed projectile ion, the double charged recoil ion and the electron were recorded.

Figure 6.2(a) displays the y-position of the recoil ion impact on the detector over the time of flight. The two vertical lines are due to He^{1+} and He^{2+} ions in coincidence with a charge-changed projectile, i.e. to recoil ions of single capture and transfer ionization processes. The curved line, which becomes horizontal at large recoil ion TOFs is due to the single ionization background. The curvature is due to the switching of the potential in the drift region. In figure 6.2(b), the vertical extensions of the He^{1+}-peak and the He^{2+}-peak after subtraction of the background are shown. The widths of both peaks do not differ significantly, indicating that the transverse momentum transfer is similar in the SC and TI processes observed here. The ratio of the peaks is $\frac{He^{2+}}{He^{1+}} \approx 3.8$. Considering possible dead time effects, this ratio gives an upper limit for the ratio of transfer ionization to single ionization processes.

Shell	binding energy [keV]	Q-value [a.u.]	photon energy [keV]	wavelength [Å]
K	2.67	97.2	4.61	2.69
L	0.67	23.7	2.61	4.75
M	0.30	10.1	2.24	5.54
N	0.17	5.3	2.11	5.88

Table 6.2: Binding energies and Q-values for Si^{14+} + He capture processes, where the initial binding energy of the electron in the helium atom is considered in the Q-value. Also photon energies and corresponding wavelengths for radiative electron capture into different shells of the Si^{14+} projectile are listed.

6.2 Single electron capture

The reaction equation of the single electron capture process reads

$$Si^{14+} + He \rightarrow Si^{13+} + He^{+} \ .$$

In non-radiative capture processes, the discrete Q-value of the reaction, i.e. the change of binding energies between the initial and final states, is directly related to the final longitudinal momentum of the recoil ion. In table 6.2 the binding energies of different shells in the Si^{13+} ion and the Q-values of the capture reactions are listed.

The longitudinal recoil ion momentum distribution displays separate peaks for capture into the L-shell and capture into higher shells (figure 6.3(a)). The ratio of the peaks depends on the transverse momentum of the recoil ions. The capture into the L-shell gains more relative importance with increasing $P_{R\perp}$, i.e. on average at smaller impact parameters (figure 6.3(b)). The capture into M-, N- and higher shells displays a maximum at a transversal momentum of about 6 a.u., whereas the L-shell capture distribution over the transverse momenta is broader, with a less pronounced maximum at about 8 – 9 a.u..

Capture into the K-shell of the Si^{14+} projectile has a smaller cross section than L-shell capture. Additionally, even smaller impact parameters are required, which results in higher transverse momenta of the recoil ions. A significant fraction of recoil ions from K-shell capture did therefore not even hit the detector. In the experimental data presented here, the intensity of recoil ions originating in K-shell capture and hitting the detector was so small that it could not be distinguished from the background.

(a) (b)

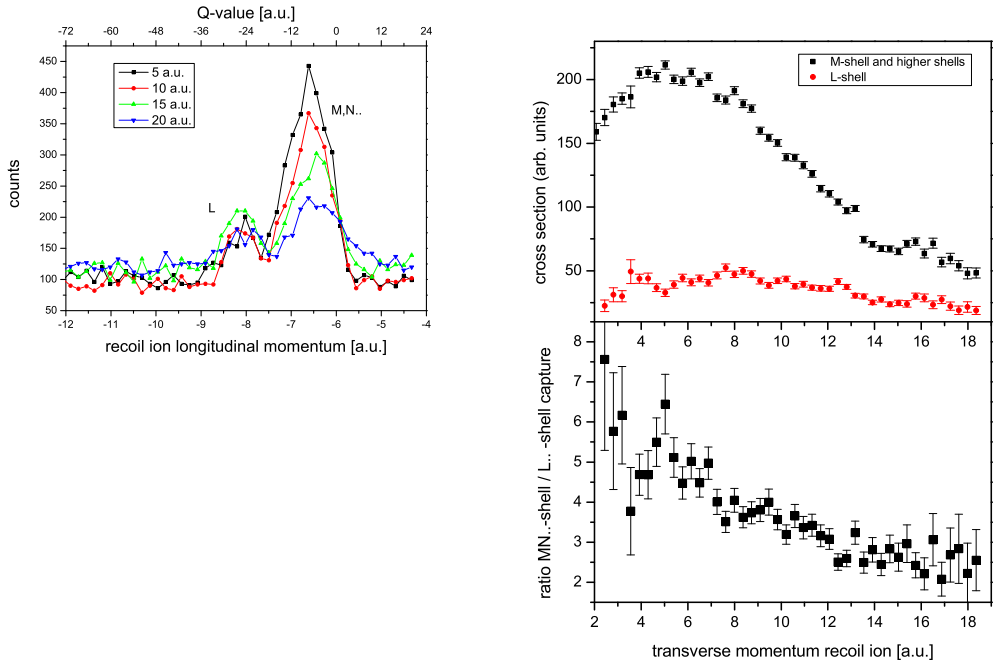

Figure 6.3: (a) The measured longitudinal recoil ion momenta correspond to different Q-values of the reaction. The two peaks can be assigned to capture into the L-shell and capture into higher shells. Their ratio differs for the transverse recoil ion momenta of 5, 10, 15 or 20 a.u.. In (b), the cross section (in arb. units) of the capture into different shells and their ratio is plotted against the transverse recoil ion momentum.

Shell	photon energy [keV]	wavelength [Å]
L to K	2.00	6.20
M to K	2.37	5.23
N to K	2.50	4.96
M to L	0.37	33.51
N to L	0.50	24.80

Table 6.3: Photon energies and photon wavelengths for radiative decay of a Si^{13+} ion.

6.2.1 Electron capture with photon coincidence

In electron capture events, different mechanisms may lead to the emission of a photon. In a REC process, a photon is emitted with the excess energy, i.e. with the kinetic energy of the target electron in the projectile frame plus the difference in initial and final binding energies. At $v_P = 12$ a.u., the kinetic energy of the target electron in the projectile frame is ~ 1.96 keV. In table 6.2 the energies and wavelengths of the emitted REC photons are listed for the capture into different shells of the Si^{14+} projectile.
A photon might also be emitted during de-excitation of an excited projectile ion. This decay is very likely to occur, because in the observed collision system, kinematic capture into the M-shell and even higher shells is preferred to kinematic capture into the ground state. Energies and wavelengths of photons originating in the decay of an excited state of a Si^{13+} ion are listed in table 6.3. They are in the same range as the energies of photons emitted in an REC process.
The triple coincidence spectrum of the charge-changed projectile, the recoil ion, and the photon is shown in figure 6.4. On the x-axis, the time of flight of the photons relative to the projectile ion is plotted,[3] and the recoil ion time of flight relative to the projectile is plotted on the y-axis. Two lines are clearly visible in the spectrum. The vertical line is due to double coincidences of a photon and a charge-changed projectile ion, and the tilted line starting at the upper left corner is due to double coincidences of photons and recoil ions, with the random detection of a projectile ion. The recoil ions which contribute to the tilted line originate mainly in single ionization processes, where the longitudinal recoil ion momentum is generally very small compared to the large negative momentum of recoil ions in kinematic capture collisions. As recoil ions with a negative longitudinal momentum component are moving towards the ion detector, the recoil ions of kinematic capture processes have a shorter time of flight. A closer look at the vertical line in figure 6.4 reveals that a peak is visible at a recoil time of flight of

[3] The time of ~ 415 ns is not the real time of flight of the photons, but the time difference of the signals from the photon and the projectile detector.

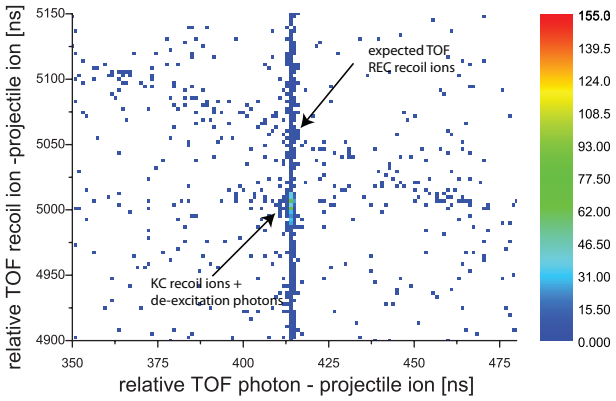

Figure 6.4: The coincidence spectrum of photons, recoil ions, and charge-changed projectiles. The vertical line corresponds to coincidences of photons and projectiles, the tilted line is due to double coincidences of recoil ions and photons. A horizontal line at around 5000 ns is barely visible, it is due to double coincidences of recoil ions and projectile ions. At the crossing of this line with the vertical line the true triple coincidences are located. There is a vertical offset of the triple coincidence spot to the point where the tilted line intersects. This offset is caused by the fact that recoil ions from single ionization events have a small longitudinal momentum, whereas the recoil ion longitudinal momentum is large in single capture events.

about 5000 ns, whereas the crossing of the two lines occurs at about 5050 ns. According to the considerations above, the peak can be assigned to kinematic capture processes into an excited state of the projectile ion followed by radiative decay.
In the radiative capture process, the recoil ion is merely a bystander. Therefore, there is no significant momentum transfer to the recoil ion, and in the coincidence spectrum they should appear approximately at the point where the visible double coincidence lines cross. As the number of photon coincidences was very small, no REC recoil ions could be clearly identified.

The cross section dependence on the transverse recoil ion momentum for capture into the M- and higher shells, followed by photon emission, is displayed in figure 6.5. Only a small number of capture events into the L-shell with photon coincidence was recorded (43 events, and 174 events for capture into the M-shell and higher shells). The ratio of the M- and higher shell events to L-shell events is $\left(\frac{M+}{L}\right)_{all} = 2.45 \pm 0.25$ without photon coincidence, whereas the ratio for events with photon coincidences is $\left(\frac{M+}{L}\right)_{\gamma} = 4.05 \pm 1.6$. The large error is due to the low count rate. The different ratios can be explained by the fact that the M-shell has no metastable states, whereas the 2s state has a lifetime of about 16 ns [SB59]. In that time, the projectile ion travels about 42 cm, and the photon can no longer reach the photon detector. Additionally, excited M-shell states can decay by the emission of two photons (through an

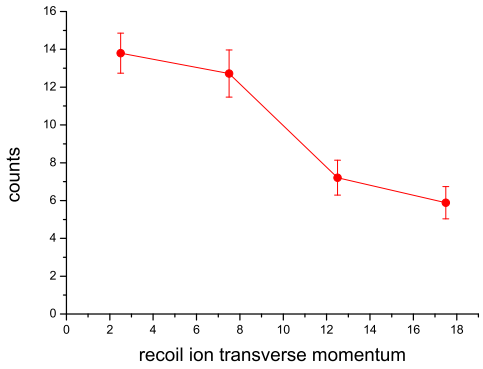

Figure 6.5: The cross section for capture into the M- or higher shells with photon coincidence.

intermediate L-shell state), which makes their detection more probable.

6.3 Transfer ionization

In our collision system, the transfer ionization cross section exceeds the cross section for single capture events, i.e. the electron transfer to the projectile ion is more likely to occur with the simultaneous emission of a second target electron. The reaction equation of the transfer ionization process reads

$$Si^{14+} + He \rightarrow Si^{13+} + He^{2+} + e^{-} \ .$$

There are three free particles in the final state; the electron, the recoil ion and the charge-changed projectile ion. The coincidence spectrum for these three particles is shown in figure 6.6. The vertical line is due to double coincidences between the recoil ion and the projectile ion. The horizontal line is due to double coincidences of the projectile ion and an electron. At the point where the two lines cross, the true triple coincidences due to transfer ionization are located. A third line is visible, starting in the upper left of the picture with a downwards tilt. This line is due to double coincidences of recoil ions and electrons with a random detection of a projectile ion.

For small electron momenta, the longitudinal momentum of the recoil ions is determined by the Q-value of the transfer ionization process. In figure 6.7(b) the number of events is plotted against the recoil ion longitudinal momentum for $|P^f_{e\|}| \leq 0.5$ a.u.. The peak of the distribution is located at $P^f_{R\|} \approx 6.2$ a.u., where the capture into the M-shell, the N-shell and higher shells is

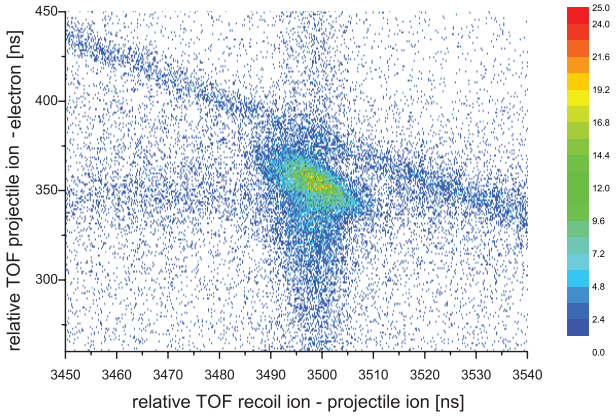

Figure 6.6: The triple coincidence spectrum of charge-changed projectiles, He^{2+} recoil ions and electrons in transfer ionization processes. The horizontal and the vertical line represent double coincidences of the projectile ion with recoil ions and electrons, respectively. The intersection of the lines mark the true triple coincidences. The double ionization background can be seen by the tilted line of recoil ion and electron coincidences. The offset of that line to the triple coincidence spot is due to the larger longitudinal momentum transfer to the recoil ion in transfer ionization processes.

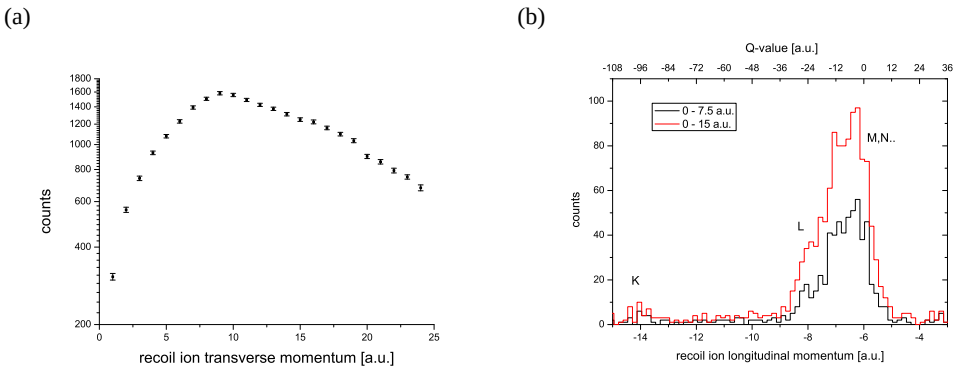

Figure 6.7: (a) The number of counts plotted against the transverse momentum of the recoil ion. As can be seen in (b), the capture into the different shells can not be resolved for the transfer ionization process. L-shell capture appears as a shoulder on the peak, which is slightly more pronounced if the transverse momentum of the recoil ions is restricted to $P^f_{R\perp} \leq 7.5\,\text{a.u.}$. A small peak can be observed at $P^f_{R\parallel} \approx 14\,\text{a.u.}$, where the contribution of K-shell capture is expected.

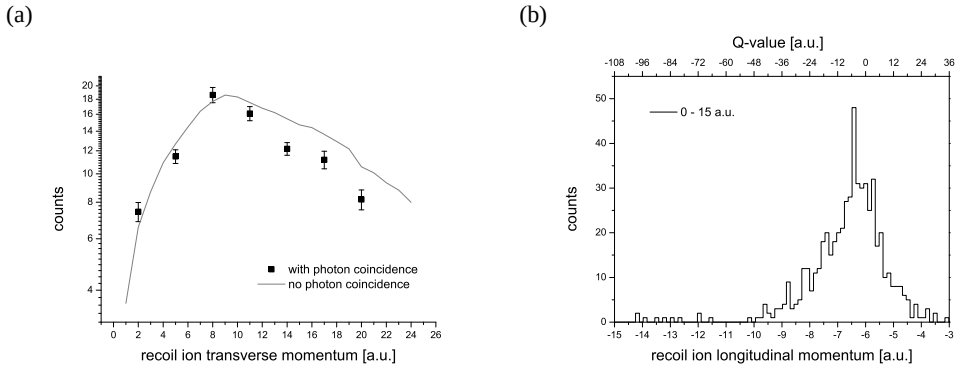

Figure 6.8: The same graphs are displayed as in figure 6.8, but this time with the condition of a coincident photon.

located. A pronounced shoulder is visible at $P^f_{R||} \approx 8$ a.u. and can be assigned to L-shell capture. Also, at $P^f_{R||} \approx 14$ a.u. a small peak is visible. At that position, the recoil ion originating from transfer ionization with capture into the K-shell is expected.

6.3.1 Transfer Ionization with photon coincidence

The measurement of transfer ionization events with the simultaneous emission of a photon requires the detection of quadruple coincidence of charge-changed projectile, recoil ion, electron and photon. The number of measured quadruple coincidences is plotted against the transverse momentum of the recoil ion in figure 6.8(a). The peak appears to be roughly in the same position as without photon coincidence. With increasing transverse momentum of the recoil ion, however, the cross section for events with photon coincidence drops more quickly. Large transverse momenta correspond to small impact parameters, where the L-shell contribution is relatively higher. Accordingly, the missing contribution of the 2s states has a relatively larger effect at higher transverse momenta. The distribution of the events with photon coincidence over the longitudinal momentum is displayed in figure 6.8(b). As expected, the small peak at $P^f_{R||} \approx 14$ a.u. is no longer present.

6.4 Discussion

To observe capture processes accompanied by photon emission in triple- (photon, projectile, recoil) and quadruple- (photon, projectile, recoil, electron) coincidence experiments is an extremely challenging task.

The experimental difficulties are twofold: First, the relative cross section of radiative electron

capture is extremely small, and a high background due to single ionization is expected. Second, photon detectors cover only a small fraction of the solid angle if they are not placed close to the reaction volume. In Reaction Microscopes, this is not possible, because the photon detector would distort the fields which guide the charged collision fragments to the detectors. In the frame of this thesis, an attempt to overcome these problems was made by first, a switching of the extraction field in the spectrometer to suppress the detection of single ionization background and second, using a large area photon detector equipped with a shielding setup to minimize field distortion. Still, with the available beamtime it was not possible to obtain sufficient statistics to resolve REC processes from the background.

Kinematic capture and transfer ionization processes were measured with the coincident detection photon emitted during decay of an excited projectile state. In the photon coincidence measurements, a relatively higher contribution of capture into the M- and higher shells was observed. This could be explained by considering the effect of the metastable L-shell state, which has a lifetime long enough for the excited projectile ion to leave the spectrometer region before decaying.

The setup could be improved by the implementation of an energy dispersive photon detector. By energy dispersive photon detection, it would be possible to distinguish REC photons from the high background. Further, a shift to higher charge states and lower velocities of the projectile ion (as available at the GSI in Darmstadt) would increase the ratio of REC to single ionization cross sections, which would simplify the detection of REC events.

7 Projectile beam coherence effects in ion-atom collisions

Even for relatively simple collision systems, the discrepancies between the theoretical models of ion-atom collisions and experimental data have not yet been fully resolved. Especially measured fully differential cross sections (FDCS), which became available for a large variety of collision systems in recent years, revealed the shortcomings of perturbative as well as non-perturbative theoretical models [MSJ$^+$02, MFF$^+$03, FPS$^+$06, MAMW10].

A first hint for a possible explanation for these discrepancies was provided by Schulz et al. [SFF$^+$07]. He described the single ionization process semi-classically, by a convolution of the first Born approximation with classical elastic nuclear scattering. Surprisingly, his results were in much better agreement with the experimental FDCS for single ionization than those of fully quantum mechanical calculations. This finding suggests that all fully quantum mechanical models share some fundamental problem which does not affect calculations treating the nuclear-nuclear interaction classically.

Indeed, there is one feature which all fully quantum mechanical treatments have in common; the incoming projectile ion wave is assumed to be fully coherent, i.e. the transverse coherence length of the projectile ion is considered infinite. In that assumption, the coherence length of the projectile wave is always larger than the size of the diffracting object, which can lead to interference effects between different amplitudes leading to the same final state, e.g. amplitudes with and without nuclear-nuclear interaction.

In experiments, the coherence length of the projectile beam is finite and often much smaller than the size of the target atom. In that case there might be no interference effects present in the measured FDCS, which will lead to discrepancies to the models. For projectile ions with a large coherence length, however, interference effects should be observable. In that case, the quantum mechanical calculations are expected to be in better agreement with the measured data than the semi-classical approach. For collisions of protons with H_2 molecules, the importance of accounting for the projectile coherence length in the analysis of atomic scattering cross sections has been demonstrated by Egodapitiya et al.[ESH$^+$11].

In the storage ring TSR, projectile beams with much longer coherence lengths than in single-pass experiments can be provided by electron cooling of the stored ion beam. Thus, collision experiments performed at the in-ring Reaction Microscope enable experiments with a coherent projectile and provide a good test for the considerations above.

7.1 The coherence length of a projectile ion beam

The transverse coherence length of a projectile ion beam can best be explained in an analogy to classical optics, where the coherence of light is a basic concept. Here, the coherence length can be understood as follows:
A diffracting object is placed at a distance L to a slit of width a (figure 7.1). According to Huygens principle, the propagation of a plane wave after the slit is a superposition of elementary spherical waves starting at each point of the slit. When the elementary waves reach the diffracting object, the path travelled by each wave differs according to their point of origin. After the distance L, the waves are diffracted on a two-centered object resembling a double slit, with the distance Δx between the centers. The path difference Δs of each wave to the two centers results in a phase difference

$$\Delta\phi = 2\pi\frac{\Delta s}{\lambda} \tag{7.1}$$

of the two diffracted parts. For a single elementary wave, i.e. for a point-like slit, this path difference leads to an interference pattern as shown in figure 7.1. For a finite width a of the slit, the interference patterns of all elementary waves are superimposed.
The maximal path difference between the elementary waves starting at the upper edge of the slit (purple in figure 7.1) and at the center (blue in figure 7.1) to the two diffraction centers is

$$\Delta s = \Delta x \cdot \sin\alpha \approx \Delta x\,\frac{a/2}{L}\ . \tag{7.2}$$

The interference pattern is only maintained up to a phase difference of $\Delta\phi < \pi$. Figure 7.1 displays two waves with $\Delta\phi = \pi$. At that phase difference, the interference effects exactly cancel each other. With equations (7.1) and (7.2), the maximal Δx for which interference is visible is the so called coherence length

$$\Delta x_{max} = \frac{L}{a}\,\lambda\ . \tag{7.3}$$

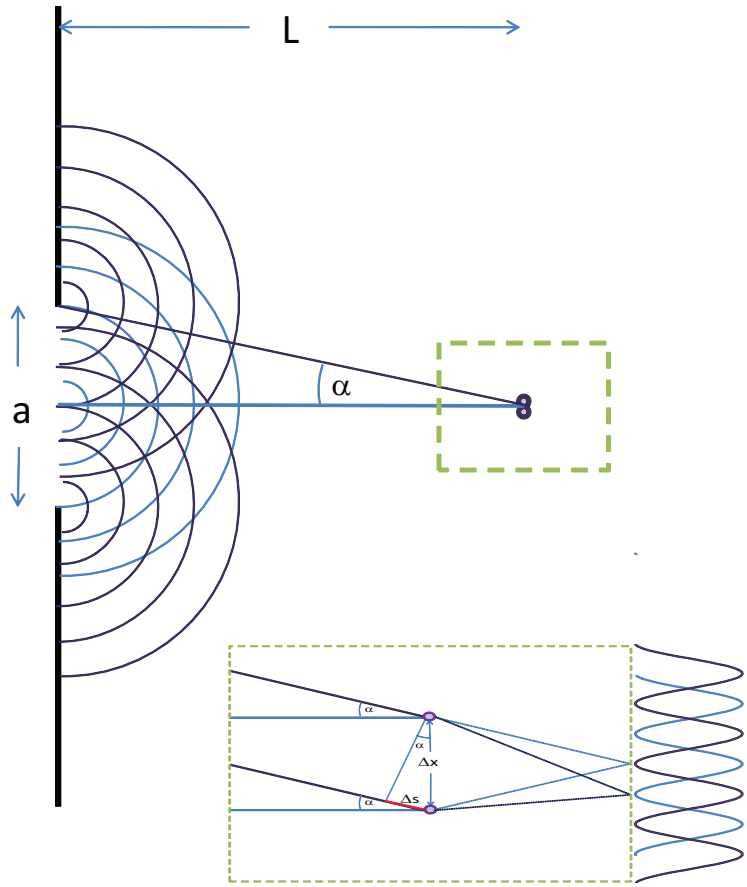

Figure 7.1: Light passes a single slit and is scattered on a two-centered object. The path difference Δs leads to an interference pattern for each single spherical elementary wave.

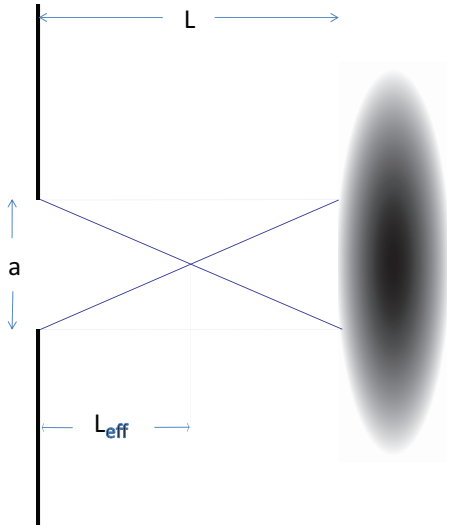

Figure 7.2: The target region illuminated by the projectile beam is essentially given by the width of the collimator. The effective distance is given by $L_{eff} = L/2$.

This equation expresses that for a given geometry and wavelength λ, interference effects are present up to the distance Δx of the two diffracting objects.

In an atomic analogy, we can consider a collision of a projectile ion with a di-atomic molecule, which takes the role of the double slit. An important difference is that the target gas region illuminated by the projectile beam has a finite extent, which is essentially given by the width of the slit (because the increase of the beamwidth due to divergence is negligible), and therefore an effective distance $L_{eff} = \frac{L}{2}$ has to be considered (see figure 7.2). For a massive projectile, the Broglie wavelength is given by

$$\lambda_{DB} = \frac{h}{P_{P\|}} \ , \tag{7.4}$$

where $P_{P\|}$ is the longitudinal momentum of the projectile and h is the Planck constant. When an ion beam passes a collimator of width a and is diffracted in the target region, the ratio $\frac{L_{eff}}{a}$ corresponds to the ratio $\frac{P_{P\|}}{\Delta P_{Px}}$ of the longitudinal momentum to the transverse momentum spread of the ions which reach the diffracting object. For the ion beam, equation (7.3) can be transformed to

$$\Delta x_{max} = \frac{1}{2} \frac{P_{P\|}}{\Delta P_{Px}} \frac{h}{P_{P\|}} \tag{7.5}$$

or

$$\Delta x_{max} \cdot \Delta P_{P\,x} = \frac{1}{2}\,h\ , \tag{7.6}$$

i.e. the coherence length of a projectile ion beam is directly related to its transverse momentum spread. In single pass experiments, the transverse momentum of the diffracted projectile ions is restricted by a collimator of width a, resembling the slit in the optical analogy.
The projectile ion beam stored in the TSR, however, is electron cooled. As the electron cooled ion beam has a small beam size ($< 1\,$mm) and a small transverse momentum spread, a collimator is obsolete. In that case, the transverse momentum spread can not be obtained from the collimator geometry, but it can be accessed via a measurement of the spatial distribution of the stored ion beam as follows:
The stored ion beam occupies an ellipse in the phase space defined by x and x', where x is the displacement of the ion from the central orbit and $x' = \frac{dx(s)}{ds} = \frac{v_x}{v_P} = \frac{P_{P\,x}}{P_{P||}}$ is the slope of the ion orbit (for details, see section 3.4). The area of that ellipse $A = \pi \cdot x_{max} \cdot x'_{max}$ is determined by the emittance ϵ of the cooled beam, $A = \pi \cdot \epsilon$. It follows that

$$x_{max} \cdot x'_{max} = \epsilon\ . \tag{7.7}$$

The spatial distribution of the ion beam depends on the position s in the storage ring, which is expressed with the β-function[1] by $x_{max} = \sqrt{\beta(s) \cdot \epsilon}$, or

$$\epsilon = \frac{x_{max}^2}{\beta(s)}\ . \tag{7.8}$$

The combination of equations (7.7) and (7.8) gives

$$x'_{max} = \frac{x_{max}}{\beta(s)}\ . \tag{7.9}$$

With $x'_{max} = \frac{P_{P\,x\,max}}{P_{P||}}$ it is finally obtained that

$$x_{max} = \beta(s) \cdot \frac{P_{P\,x\,max}}{P_{P||}}\ . \tag{7.10}$$

The longitudinal momentum $P_{P||}$ is well known for a stored ion beam, as are the values of the β-function through the storage ring. The spatial distribution of the stored beam is measured at

[1] The β-function describes the variation of the beam size through the ring and has a fixed value at each position. It is explained in more detail in section 3.4

the beam profile monitors, and with equation (7.10) the momentum spread of the beam can be calculated.[2] Due to electron cooling, very small beam emittances are reached [Art12]. Thereby, large coherence lengths can be obtained, which are much larger than the size of a helium target atom (except for very large or heavy ions).

7.2 Single ionization of helium target atoms by a coherent proton projectile beam

A proton beam with an energy of 3 MeV, which corresponds to a velocity of $\approx$ 11 a.u. and a perturbation $\eta = \frac{Z_p}{v_p} \approx 0.1$, was intersected with an helium target beam [WSL$^+$12]. The emittance of the projectile beam is about 0.05 mm mrad, and the measured beam size was less than 1 mm. According to the considerations above, the coherence length of the beam is about 5 a.u., which is much larger than the size of a helium atom. Therefore, the beam is considered coherent. The charged collision fragments are extracted by an electric field in the acceleration region of 2 V/cm, and the strength of the Helmholtz field guiding the electrons is $\approx$ 11 G. Recoil ions and emitted electrons are detected in coincidence. The transverse momentum acceptance for the electrons of 1.8 a.u., with an estimated resolution of 0.2 a.u. (FWHM) in that direction, and 0.05 a.u. in the longitudinal direction. The estimated momentum resolution for the recoil ions is 0.4 a.u. in the transverse and 0.25 a.u. in the longitudinal direction.

FDCS for the collision system of 100 MeV/u C^{6+} impact on helium atoms were measured by Schulz et al. [SMF$^+$03], where they found significant discrepancies between the experimental FDCS and various quantum mechanical calculations. In C^{6+} collisions, the coherence length was about $\approx 10^{-3}$ a.u., which is much smaller than the size of an atom, and the beam can be considered incoherent. The perturbation for this system is the same as for the proton collision system described above, and therefore a very similar shape of the proton beam cross sections is expected, when the coherence length is not considered.
Indeed, if the particles are emitted in the projectile scattering plane the experimentally obtained cross sections are similar for both collision systems. But for electrons emitted outside this plane, significant differences can be observed.

Figure 7.4 shows the FDCS for both collision systems for electrons emitted in the azimuthal plane, i.e. perpendicular to the projectile beam direction (see figure 7.3). The kinetic energy of the electrons is 6.5 eV, and the total momentum transfer of the projectile ion is $q = 0.75$ a.u..

[2] The spatial distribution as well as the momentum distribution of the ion beam is Gaussian shaped. Therefore, the transverse momentum spread is typically expressed by the standard deviation of the distribution, σ_{P_x}.

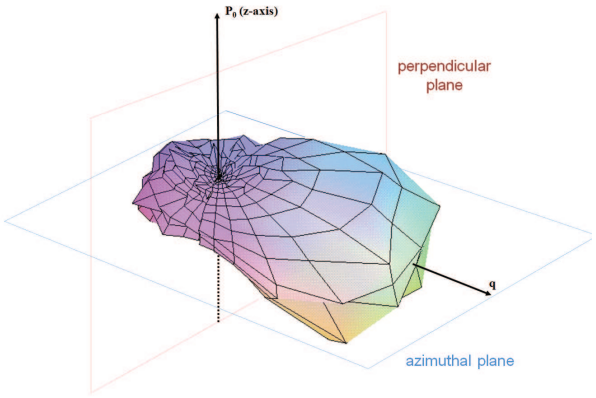

Figure 7.3: The three dimensional angular distribution of electrons emitted in the C^{6+} on He collision [SMF+03]. The azimuthal plane is the plane perpendicular to the initial momentum of the projectile. The so called perpendicular plane is the plane perpendicular to the momentum transfer **q**.

At the azimuthal angle of $\phi_e = 90°$ the electron is emitted in the direction of the momentum transfer **q**, whereas $\phi_e = 270°$ signifies the emission in the direction of $-\mathbf{q}$. At these positions, the well known binary peak and the recoil peak occur, where the recoil peak still has a comparably large contribution to the cross section at the small perturbation $\eta = 0.1$.
Especially in the proton collision data, the binary peak and the recoil peak are clearly separated by a pronounced minimum at about 180°. At that position, there is only a weak minimum in the C^{6+} data, and the recoil peak is barely separated from the binary peak. Also, the widths of the peaks are broader in the C^{6+} collisions.
A comparison of the results with the 3DW model[3] and the first Born approximation convoluted with classical elastic scattering [SFF+07] is included in figure 7.4. The 3DW calculation, which treats the C^{6+} projectile beam as a coherent wave, reveals severe qualitative discrepancies to the experimental C^{6+} data. Especially the dip at 180° is overestimated in the calculation. A comparison of the 3DW model to the proton data, however, shows a much better agreement. The semi-classical approach including elastic scattering of the nuclei, on the other hand, fails to qualitatively reproduce the shape of the coherent proton beam FDCS, but is in very good agreement with the FDCS obtained with the incoherent C^{6+} beam.
Therefore, it can be concluded that while the interaction with an incoherent projectile beam is better reproduced by the semi-classical calculation, indeed the preparation of a coherent projectile beam enables the acquisition of fully differential cross sections which are in better

[3] I.e. the three body DW approximation.

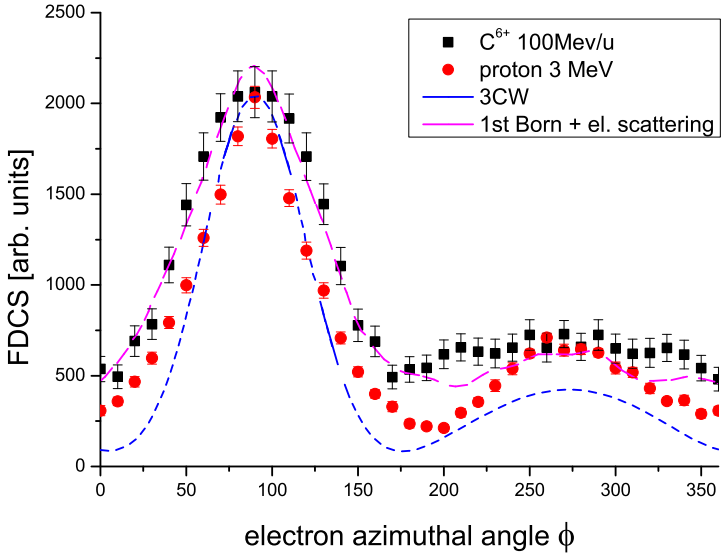

Figure 7.4: The fully differential TI cross sections for electrons emitted in the azimuthal plane in 3 MeV proton and 100 MeV/u C^{6+} on helium. The coherent proton beam cross section is in better agreement to the fully quantum mechanical 3DW calculation, whereas the incoherent C^{6+} beam cross section is better resembled by a classical treatment of the nuclear-nuclear scattering.

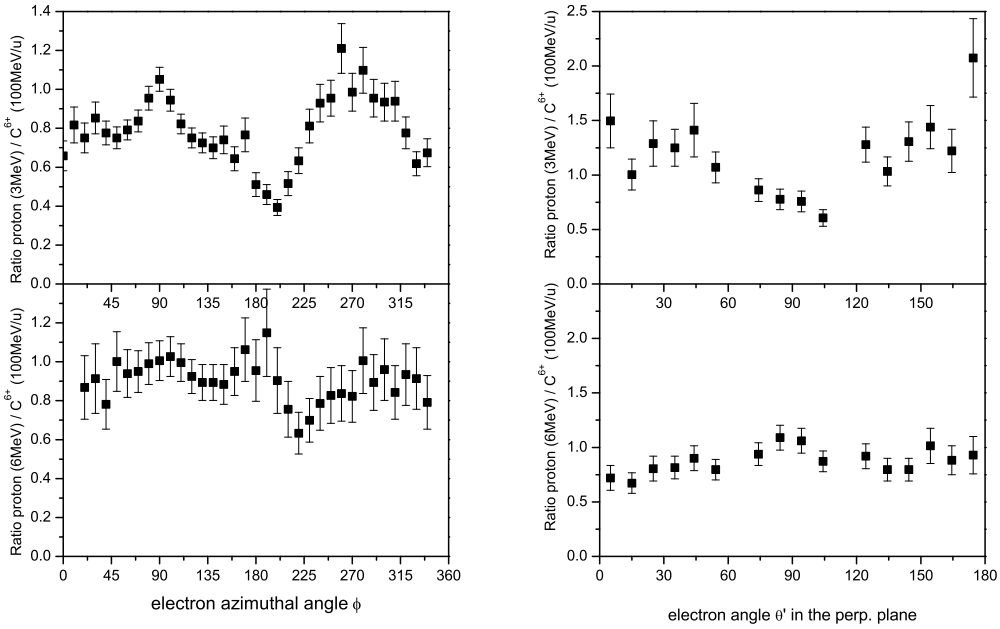

Figure 7.5: The ratio of the coherent 3 MeV proton beam cross section and the incoherent 100 MeV/u C^{6+} beam cross section (a) in the azimuthal plane and (b) in the perpendicular plane. In both planes, oscillations can be observed.

agreement with the 3DW model assuming a coherent projectile beam.

The cross section for a coherent beam can be expressed as the cross section for an incoherent beam multiplied by the interference term IT. When the assumptions are made that the proton beam is fully coherent, and that the C^{6+} beam is fully incoherent, and that the incoherent cross sections of both projectiles are very similar, the interference term IT can be approximated by the cross section ratio of the proton beam relative to the C^{6+} beam.

In figure 7.5, the cross section ratios for the 3 MeV proton beam and the 100 MeV/u C^{6+} beam are shown in the upper panels. An oscillating structure is observed both over the azimuthal electron emission angle ϕ_e and over the electron emission angle θ'_e in the plane perpendicular to **q**.

Fischer et al. ([FSMU04]) measured the FDCS of the single ionization process for a 6 MeV proton beam colliding with a helium target atom. The perturbation parameter is slightly smaller due to the higher energy, $\eta = 0.065$, but a significant change of cross section is not expected for such small values of η. The coherence length of the beam was $\Delta x_c \approx 0.05$ a.u., which is much

smaller than the size of an atom. Therefore, the 6 MeV proton beam can be considered fully incoherent. The cross section ratio for the 6 MeV proton beam and the 100 MeV/u C^{6+} beam is a ratio of two incoherent cross sections, and should not exhibit interference effects. In figure 7.5, these ratios of the two incoherent beams are displayed in the lower panels. The experimentally obtained distributions are not perfectly flat, but the structure is clearly much less pronounced compared to the ratio of coherent to incoherent cross section.

7.3 Discussion

The presence of interference effects can more intuitively be understood for molecular targets, i.e. H_2 molecules, because the two atomic centers resemble a double slit in the optical analogy, where the two resulting reactions paths interfere. In the case of the collision of a coherent projectile beam with an atomic target, the nature of the coherence is more complex.
In the fully quantum mechanical description of single ionization, first order processes only account for the electron-projectile interaction. The nuclear-nuclear interaction is included starting from second order perturbation theory, where an interference term between first and second order processes contributes to the total cross section (see equation (4.30) in chapter 4). For incoherent beams where no interference occurs, this term results in artificial contributions to the cross section. Now it can be understood why the seemingly incomplete semi-classical approach by Schulz et al. was better suited to describe the incoherent beam cross sections.
A semi-classical simplification might be helpful for a conception of the nature of the interference: Due to the long range of the Coulomb force, a large range of impact parameters contributes to the single ionization cross section. A first order and a second order mechanism with different impact parameters might result in the same final state [Sar10]. If the coherence length of the projectile beam covers the impact parameter distribution of both mechanisms, their amplitudes interfere.
The distance between the impact parameters plays a similar role as the internuclear distance in the H_2 molecule and the distance between the double slits Δx in the optical analogy. If the projectile is seen as an incoming wave-packet, the phase shift between the interfering amplitudes for a given scattering angle depends on the impact parameter separation, just as the phase shift depended on Δx in the optical analogy (see equations (7.1) and (7.2)). For a given path difference, the phase shift depends on the momentum (on the De Broglie wavelength) of the emitted electron, which explains the oscillations in the interference effects over the electron emission angle.

In conclusion, the experimental FDCS of single ionization of a helium target by a coherent proton projectile beam were obtained. These FDCS are in much better agreement to the fully quantum mechanical model than experimental FDCS of former experiments with incoherent projectile beams.
The ratio of coherent to incoherent cross sections reveals an oscillating structure over the angle of electron emission in the azimuthal and perpendicular plane. That oscillation is absent in the ratio of incoherent to incoherent cross sections.
The results of the experiment indicate that the projectile coherence length is an important parameter in the dynamics of ion-atom collisions. Until now, the finite coherence length of the projectile beam has been completely overlooked in the theoretical understanding of ion-atom collisions. Thereby, artificial interference effects are -at least to a certain extent- an explanation of the puzzling discrepancies between theoretical models and experimental FDCS. Further studies and refined theoretical descriptions are needed to investigate the nature of the interference, and the effect of the beam coherence length on collision dynamics and cross sections.

8 Conclusion

In the framework of this thesis, a Reaction Microscope was successfully implemented into the heavy ion cooler storage ring TSR at the Max-Planck-Institut für Kernphysik. An electron cooled ion beam has advantageous properties for the investigation of ion-atom collisions. The stored ions cycle in the ring and repeatedly pass the target region. Thereby, high beam intensities are reachable, and good statistics can be obtained in relatively short measuring time even for collision processes with a small cross section, like electron capture or transfer ionization. Furthermore, the electron-cooled beam features a very low emittance, i.e. a small spatial extension and a small momentum spread. The small size of the ion beam permits a well defined interaction region, which in turn allows for a good resolution of the measured recoil ion and electron momenta. Moreover, the transverse momentum spread is directly related to the coherence length of the projectile beam. In typical single pass experiments, where the transverse momentum spread is defined by collimators, the coherence length of the projectiles can be much smaller than the size of a helium atom. Due to the low emittance of the stored beams in the TSR, it was possible to obtain beams whose coherence length was much larger than the size of the target atom. Therefore, we were able to investigate for the first time the effect of the projectile coherence on the dynamics of collisionally induced ionization of target atoms.
In this work, we focused on three collision processes: Transfer ionization, electron capture, and single ionization.

In order to investigate the mechanisms of transfer ionization, we chose two collision systems with a different perturbation. Generally speaking, transfer ionization processes can be divided into two categories; First, the independent process, where the projectile ion captures one electron and ionizes another in two independent, subsequent interactions. And second, the correlated processes, where the finally ejected target electron is emitted due to electronic correlation. Only recently such a correlated process has been proposed [VNU08], which has been completely overlooked in decades of research.
For 1 MeV/u O^{7+} projectiles with a high perturbation ($\eta \approx 1.1$), as expected the independent transfer ionization process clearly dominates over the correlated processes. The electrons were with a strong preference emitted in the forward direction, which is a result of the post collision

interaction. In a theoretical model based on the continuum distorted wave approximation, the cross sections could qualitatively be reproduced.
The perturbation of 1 MeV/u Li^{3+} projectiles is lower ($\eta \approx 0.5$), and here the newly proposed electron-electron transfer ionization process was expected to significantly contribute to the cross section. Indeed, electron emission was found to be strongly focused in the backward direction, which is a predicted feature of the electron-electron transfer ionization process. Therefore, in this experiment clear evidence of the electron-electron transfer ionization was provided.

In the single electron capture measurements, we attempted to obtain kinematically complete data on radiative electron capture. This is an extremely challenging experiment, as the cross section for radiative capture is several orders of magnitude smaller than the cross section for kinematic capture or target ionization. A photon spectrometer was implemented into the Reaction Microscope, and triple coincidences between charge-changed projectiles, recoiling target ions and photons were recorded. For transfer ionization events, when the capture process was accompanied by a simultaneous emission of a second target electron, even quadruple coincidences were observed. However, due to the limited statistics and high background, in the framework of this thesis it was not possible to unambiguously identify radiative capture processes. The detected photons were found to originate predominantly from capture processes to excited states of the projectile ions, which decay radiatively. The relative contribution of the populated states was found to be affected strongly by the photon coincidences. This can be explained by different lifetimes of the populated states which might decay after leaving the spectrometer region.

Single ionization, which was the third process under investigation within this thesis, is perhaps the most-studied reaction in ion-atom collisions. However, discrepancies between theoretical and experimental fully differential cross sections (FDCS) exist even for rather simple collision systems, and have puzzled researchers for almost a decade now. One feature which is shared by all fully quantum mechanical calculations is the assumption of an infinite coherence length of the projectile beam. In collision experiments, in contrast, the coherence length is finite and, as already mentioned, generally much smaller than the target atom. We measured fully differential cross sections for single ionization processes with a coherent 3 MeV proton projectile and obtained significantly better agreement with the theoretical calculations. On the other hand, severe discrepancies were observed in comparison to FDCS which were measured with a incoherent beam of the same perturbation ($\eta = 0.1$). The influence of the projectile coherence length has not been included in any theoretical model. Herein, a possible explanation is offered

for the long puzzling discrepancies between experimental FDCS and quantum mechanical calculations.
Further studies will be necessary to understand the exact nature of the interference effects in coherent collision systems, and especially an inclusion of the beam coherence into theoretical models is clearly required.

The success of first experiments with a Reaction Microscope in the TSR motivated the development and implementation of a next generation Reaction Microscope, in which the stored ion beam is intersected with a laser cooled target. Presently, the target atoms prepared in the magneto optical trap are lithium atoms. As both weaker and stronger electron-electron correlations than in helium are expected between the electrons in different shells of the lithium atom, it is a well suited target atom to investigate the effect of electronic correlations on, for instance, transfer ionization cross sections.

Bibliography

[ACK+97] M Abdallah, CL Cocke, S Kravis, EC Montenegro, and R Moshammer. Recent recoil ion momentum spectroscopy experiments at KSU. In *APPLICATION OF ACCELERATORS IN RESEARCH AND INDUSTRY - PROCEEDINGS OF THE FOURTEENTH INTERNATIONAL CONFERENCE, PTS 1 AND 2*, number 392 in AIP CONFERENCE PROCEEDINGS, pages 209–212. American Institute of Physics, New York, 1997.

[Art12] S Artikova. *Low Energy Ions in the Heavy Ion Cooler Storage Ring TSR*. PhD thesis, University Heidelberg, 2012.

[Bas09] R Bastert. Erzeugung kurzer Ionenpulse in einem Speicherring. diploma thesis, University Heidelberg, 2009.

[BBF+88] P Baumann, M Blum, A Friedrich, C Geyer, and M Grieser. The Heidelberg Heavy-ion Test Storage Ring TSR. *Nuclear instruments & methods in physics research. Section A, Accelerators, spectrometers, detectors and associated equipment*, 268(2-3):531–537, 1988.

[Bet30] H Bethe. Zur Theorie des Durchgangs schneller Korpuskularstrahlen durch Materie. *Annalen der Physik*, 397(3):325, 1930.

[Beu00] M Beutelspacher. *Systematische Untersuchungen zur Elektronenkühlung am Heidelberger Schwerionenspeicherring TSR*. PhD thesis, University Heidelberg, 2000.

[BFKS02] I Bray, DV Fursa, AS Kheifets, and AT Stelbovics. Electrons and photons colliding with atoms development and application of the convergent close-coupling method. *Journal of physics. B, Atomic, molecular and optical physics*, 35(15):R117–R146, 2002.

[BGN+03] M Beutelspacher, M Grieser, K Noda, D Schwalm, and A Wolf. Dispersive electron cooling experiments at the heavy ion storage ring TSR. *Nuclear instruments*

& *methods in physics research. Section A, Accelerators, spectrometers, detectors and associated equipment*, 512(3):459–469, 2003.

[BK30] HC Brinkman and HA Kramers. The theory of the collection of electrons by means of alpha-particles. *Proceedings of the Section of sciences Koninklijke Nederlandse akademie van wetenschappen*, 33(6/10):973–984, 1930.

[Blu89] M Blum. *Entwicklung einer neuartigen Synchrotron-Beschleunigungskavität*. PhD thesis, University Heidelberg, 1989.

[BT79] JS Briggs and K Taulbjerg. Charge-transfer by a double-scattering mechanism involving target electrons. *Journal of physics. B, Atomic, molecular and optical physics*, 12(15):2565–2573, 1979.

[CDF+96] A Cassimi, S Duponchel, X Flechard, P Jardin, and P Sortais. State-selective electron capture in low velocity multiply charged ion-helium collisions. *Physical review letters*, 76(20):3679–3682, 1996.

[CEM87] JH Chappell, E Everman, and SS Murray. Surface characteristics and quantum efficiency measurements of csi-coated microchannel plates. *Nuclear instruments & methods in physics research. Section A, Accelerators, spectrometers, detectors and associated equipment*, 260(2-3):483–490, 1987.

[Che64] IM Cheshire. Continuum distorted wave approximation - resonant charge transfer by fast protons in atomic hydrogen. *Proceedings of the Physical Society of London*, 84(5371):89, 1964.

[CM83] DSF Crothers and JF McCann. Ionization of atoms by ion impact. *Journal of physics. B, Atomic, molecular and optical physics*, 16(17):3229–3242, 1983.

[CMD94] MA Coplan, JH Moore, and JP Doering. (e,2e) spectroscopy. *Reviews of modern physics*, 66(3):985–1014, 1994.

[CVB+05] G Da Costa, F Vurpillot, A Bostel, M Bouet, and B Deconihout. Design of a delay-line position-sensitive detector with improved performance. *Review of scientific instruments*, 76(1), 2005.

[DKS+01] A Dorn, A Kheifets, CD Schröter, B Najjari, C Höhr, R Moshammer, and J Ullrich. Double ionization of helium by electron-impact: complete pictures of the four-body breakup dynamics. *Physical review letters*, 86(17):3755–8, 2001.

[DMJ+00] R Dörner, V Mergel, O Jagutzki, L Spielberger, J Ullrich, R Moshammer, and H Schmidt-Böcking. Cold target recoil ion momentum spectroscopy : a ' momentum microscope ' to view atomic collision dynamics. *Physics Reports*, 330(2-3):95–192, 2000.

[DNS+07] M Dürr, B Najjari, M Schulz, A Dorn, and R Moshammer. Analysis of experimental data for ion-impact single ionization of helium with Monte Carlo event generators based on quantum theory. *Physical review. A*, 75(6), 2007.

[Dri55] R M Drisko. PhD thesis, Carnegie Institute of Technology, 1955.

[EM95] J Eichler and WE Meyerhof. *Relativistic atomic collisions*. Academic Press, 1995.

[ES07] J Eichler and Th Stöhlker. Radiative electron capture in relativistic ion-atom collisions and the photoelectric effect in hydrogen-like high-Z systems. *Physics reports*, 439(1-2):1–99, 2007.

[ESH+11] KN Egodapitiya, S Sharma, A Hasan, AC LaForge, and DH Madison. Manipulating atomic fragmentation processes by controlling the projectile coherence. *Physical review letters*, 106(15), 2011.

[EST09] T Elkafrawy, A Simon, and J A Tanis. X-ray processes associated with projectile charge changing in 1 MeV/u collisions of O 5+ on Ar. *Journal of physics. Conference series*, 194(8), 2009.

[FBP+84] GW Fraser, MA Barstow, JF Pearson, MJ Whiteley, and M Lewis. The soft X-ray detection efficiency of coated microchannel plates. *Nuclear Instruments and Methods in Physics Research*, 224(1–2):272 – 286, 1984.

[FFT12] C Froese-Fischer and G Tachiev. MCHF/MCDHF Collection, Version 2. Available online at http://physics.nist.gov/mchf, last visited april 2012.

[FGG+] D Fischer, D Globig, J Goullon, M Grieser, and R Hubele. Ion-lithium collision dynamics studied with an in-ring MOTReMi. to be published.

[Fis03] D Fischer. *Mehr-Teilchen-Dynamik in der Einfach- und Doppelionisation von Helium durch geladene Projektile*. PhD thesis, University Heidelberg, 2003.

[FIS05] S Fritzsche, P Indelicato, and Th Stöhlker. Relativistic quantum dynamics in strong fields: photon emission from heavy, few-electron ions. *Journal of physics. B, Atomic, molecular and optical physics*, 38(9):S707–S726, 2005.

[FMD+03] D Fischer, R Moshammer, A Dorn, JRC Lopez Urrutia, B Feuerstein, H Kollmus, C Höhr, C D Schröter, S Hagmann, R Mann, B Bapat, and J Ullrich. Projectile-charge sign dependence of four-particle dynamics in helium double ionization. *Physical review letters*, 90(24):243201, 2003.

[FMS+03] D Fischer, R Moshammer, M Schulz, A Voitkiv, and J Ullrich. Fully differential cross sections for the single ionization of helium by ion impact. *Journal of physics. B, Atomic, molecular and optical physics*, 36(17):3555–3567, 2003.

[FO04] J Fiol and RE Olson. Three- and four-body dynamics in fast heavy ion-atom ionization. *Journal of physics. B, Atomic, molecular and optical physics*, 37(19):3947–3960, 2004.

[FOO06] J Fiol, S Otranto, and RE Olson. Critical comparison between theory and experiment for C6++He fully differential ionization cross sections. *Journal of physics. B, Atomic, molecular and optical physics*, 39(14):L285–L290, 2006.

[FPL87] GW Fraser, JF Pearson, and JE Lees. Cesium bromide X-ray photocathodes. *Nuclear instruments & methods in physics research. Section A, Accelerators, spectrometers, detectors and associated equipment*, 256(2):401–405, 1987.

[FPS+06] M Foster, JL Peacher, M Schulz, DH Madison, and Z Chen. Unexpected higher-order effects in charged particle impact ionization at high energies. *Physical review letters*, 97(9):093202, 2006.

[Fra83] GW Fraser. The characterisation of soft x-ray photocathodes in the wavelength band 1–300 Å: I. lead glass, lithium fluoride and magnesium fluoride. *Nuclear Instruments and Methods in Physics Research*, 206(1–2):251 – 263, 1983.

[FSC+06] D Fischer, K Stochkel, H Cederquist, H Zettergren, and P Reinhed. Experimental separation of the Thomas charge-transfer process in high-velocity p-He collisions. *Physical review. A*, 73(5), 2006.

[FSMU04] D Fischer, M Schulz, R Moshammer, and J Ullrich. Comparative study of single and double ionization of helium by ion impact. *Journal of physics. B, Atomic, molecular and optical physics*, 37(5):1103–1111, 2004.

[GH92] R Gayet and J Hanssen. Transfer and excitation in ion atom collisions at high-impact velocities - a unified continuum distorted-wave treatment of resonant and

nonresonant modes in a 4-body approach .1. theory. *Journal of physics. B, Atomic, molecular and optical physics*, 25(4):825–837, 1992.

[GIKN89] H Grote, FC Iselin, E Keil, and J Niederer. The MAD program. pages 1292–4 vol.2. 1989.

[GSM+09] M Gudmundsson, HT Schmidt, D Misra, D Fischer, and H Cederquist. Electron-transfer to H + and He 2+ from He at high velocities. *Journal of physics. Conference series*, 194(8), 2009.

[HLC98] KA Hanold, AK Luong, and RE Continetti. Complete kinematic measurement of three-body reaction dynamics: Dissociative photodetachment of O-6(-) at 532 nm. *The Journal of chemical physics*, 109(21):9215–9218, 1998.

[HPCS83] E Horsdal-Pedersen, CL Cocke, and M Stockli. Experimental observation of the Thomas peak in high-velocity electron capture by protons from He. *Physical review letters*, 50(24):1910–1913, 1983.

[HWS+72] Schnopper HW, HE Wegner, AR Sohval, K Kalata, and HD Betz. Evidence for radiative electron-capture by fast, highly stripped heavy-ions. *Physical review letters*, 29(4):898–&, 1972.

[IM91] P Indelicato and PJ Mohr. Quantum electrodynamic effects in atomic structure. *Theoretical Chemistry Accounts: Theory, Computation, and Modeling (Theoretica Chimica Acta)*, 80:207–214, 1991. 10.1007/BF01119620.

[Isl94] RC Isler. An overview of charge-exchange spectroscopy as a plasma diagnostic. *Plasma Physics and Controlled Fusion*, 36(2):171–208, 1994.

[Jö98] P Jönsson. On the status and perspectives of MCDF calculations and measurements of transition data in the Be isoelectronic sequence. *Journal of physics. B, Atomic, molecular and optical physics*, 31(16):3497, 1998.

[KADJ95] T Kambara, JZ Tangand Y Awaya, BD Depaola, and O Jagutzki. 3-dimensional recoil-ion momentum analyses in 8.7 MeV O7+-He collisions. *Journal of physics. B, Atomic, molecular and optical physics*, 28(21):4593–4606, 1995.

[Kal95] TR Kallman. X-ray diagnostics of cosmic photoionized plasmas. In *ATOMIC PROCESSES IN PLASMAS*, number 322 in AIP CONFERENCE PROCEEDINGS, pages 36–52. American Institute of Physics, New York, 1995.

[Lan07] C Langbrandtner. Experimente zur Ionisation von atomarem Wasserstoff im Ionenstoß. diploma thesis, University Heidelberg, 2007.

[LB02] A Lahmam-Bennani. Thirty years of experimental electron-electron (e,2e) coincidence studies: achievements and perspectives. *Journal of electron spectroscopy and related phenomena*, 123(2-3):365–376, 2002.

[LFP+96] JE Lees, GW Fraser, SE Pearce, JF Pearson, and VN Shchemelev. Thermally annealed soft X-ray photocathodes. *Nuclear instruments & methods in physics research. Section A, Accelerators, spectrometers, detectors and associated equipment*, 381(2-3):453–61, 1996.

[MAMW10] M McGovern, D Assafrao, JR Mohallem, and C Whelan. Coincidence studies of He ionized by C(6+), Au(24+), and Au(53+). *Physical review. A*, 81(4), 2010.

[Mat95] DL Matthews. Review of x-ray lasers. *Nuclear instruments & methods in physics research. Section B, Beam interactions with materials and atoms*, 98(1-4):91–94, 1995.

[MBB+95] JH McGuire, N Berrah, RJ BAartlett, JAR Samson, and JA Tanis. The ratio of cross-sections for double to single ionization of helium by high-energy photons and charged-particles. *Journal of physics. B, Atomic, molecular and optical physics*, 28(6):913–940, 1995.

[MC70] RC McDowell and JP Coleman. *Introduction to the theory of ion-atom collisions*. North-Holland Pub. Co., 1970.

[MCH72] JW McConkey, A Crowe, and MA Hender. Differential cross-sections in electron-impact ionization of atoms and molecules. *Physical review letters*, 29(1):1–&, 1972.

[MDAS88] JH McGuire, NC Deb, Y Aktas, and NC Sil. Shakeover probability for electron-capture. *Physical review. A*, 38(7):3333–3338, 1988.

[MDK+01] V Mergel, R Dorner, K Khayyat, M Achler, T Weber, R Drner, O Jagutzki, H J Lüdde, CL Cocke, and H Schmidt-Böcking. Strong correlations in the He ground state momentum wave function observed in the fully differential momentum distributions for the p + He transfer ionization process. *Physical review letters*, 86(11):2257–2260, 2001.

[MFF+03] DH Madison, D Fischer, M Foster, M Schulz, R Moshammer, S Jones, and J Ullrich. Probing scattering wave functions close to the nucleus. *Physical review letters*, 91(25):253201, 2003.

[MMB+03] X Ma, PH Mokler, F Bosch, A Gumberidze, and C Kozhuharov. Electron-electron interaction studied in strong central fields by resonant transfer and excitation with H-like U ions. *Physical review. A*, 68(4), 2003.

[MR84] JM Maidagan and RD Rivarola. A symmetric eikonal-type approximation for electron-capture in ion-atom collisions. *Journal of physics. B, Atomic, molecular and optical physics*, 17(12):2477–2487, 1984.

[MSJ+02] D Madison, M Schulz, S Jones, M Foster, and R Moshammer. Comparison of theoretical and absolute experimental fully differential cross sections for ion-atom impact ionization. *Journal of physics. B, Atomic, molecular and optical physics*, 35(15):3297–3314, 2002.

[MSS06] DR Marsh, OHW Siegmund, and JM Stock. Progress on high-efficiency photocathodes for soft x-ray, EUV, and FUV photon detection. *Proc. SPIE*, 51 (1993), 2006.

[MUU+94] R Moshammer, J Ullrich, M Unverzagt, W Schmitt, and P Jardin. Low-energy electrons and their dynamical correlation with recoil ions for single ionization of helium by fast, heavy-ion impact. *Physical review letters*, 73(25):3371–3374, 1994.

[MUU+96] R Moshammer, J Ullrich, M Unverzagt, W Schmitt, and P Jardin. The dynamics of target ionization by fast highly charged projectiles. *Nuclear instruments & methods in physics research. Section B, Beam interactions with materials and atoms*, 107(1-4):62–66, 1996.

[MWW+97] EC Montenegro, KL Wong, W Wu, P Richard, I Ben-Itzhak, CL Cocke, R Moshammer, JP Giese, YD Wang, and CD Lin. Projectile charge-state dependence of transfer ionization to single capture ratio in collisions of multiply charged ions with He. *Phys. Rev. A*, 55:2009–2014, Mar 1997.

[OGB+87] RE Olson, TJ Gay, HG Berry, EB Hale, and VD Irby. Saddle-point electrons in ionizing ion-atom collisions. *Physical review letters*, 59(1):36–39, 1987.

[Opp28] JR Oppenheimer. On the quantum theory of the capture of electrons. *Physical review*, 31(3):0349–0356, 1928.

[RBF+11] X Ren, I Bray, DV Fursa, J Colgan, MS Pindzola, T Pflüger, A Senftleben, S Xu, A Dorn, and J Ullrich. Electron-impact ionization of helium: A comprehensive experiment benchmarks theory. *Phys. Rev. A*, 83:052711, May 2011.

[RBIM99] TN Rescigno, M Baertschy, WA Isaacs, and CW McCurdy. Collisional breakup in a quantum system of three charged particles. *Science*, 286(5449):2474–2479, 1999.

[RGHH74] R Repnow, M Goldschmidt, K Haberkantand KD Hildenbrand, and G Hortig. Heidelberg MP Tandem Vandegraaff. *Nuclear instruments and methods*, 122(1-2):179–189, 1974.

[RWL95] VD Rodriguez, YD Wang, and CD Lin. Theory of longitudinal recoil-ion momentum distribution in ion-atom ionization. *Physical review. A*, 52(1):R9–R12, 1995.

[Sar10] L Sarkadi. Classical trajectory Monte Carlo model calculations for ionization of atomic hydrogen by 75-keV proton impact. *Physical review. A*, 82(5), 2010.

[SB59] J Shapiro and G Breit. Metastability of 2*s* states of hydrogenic atoms. *Phys. Rev.*, 113:179–181, Jan 1959.

[SBB+90] M Steck, G Bisoffi, M Blum, A Friedrich, and C Geyer. Electron cooling of heavy-ions. *Nuclear instruments & methods in physics research. Section A, Accelerators, spectrometers, detectors and associated equipment*, 287(1-2):324–327, 1990.

[SBF+04] Th Stöhlker, D Banas, S Fritzsche, A Gumberidze, and C Kozhuharov. Angular correlation and polarization studies for Radiative Electron Capture into high-Z ions. *Physica scripta*, T110:384–388, 2004.

[SBMD+03] H Schmidt-Böcking, V Mergel, R Dorner, CL Cocke, and O Jagutzki. Revealing the non-s(2) contributions in the momentum wave function of ground-state He. *Europhysics letters*, 62(4):477–483, 2003.

[SCK+09] M Schulz, M F Ciappina, T Kirchner, D Fischer, and R Moshammer. Role of elastic projectile-electron scattering in double ionization of helium by fast proton impact. *Physical review. A*, 79(4), 2009.

[Sco88] G Scoles. *Atomic and Molecular Beam Methods*. Number Bd. 1 in Atomic and Molecular Beam Methods. Oxford University Press, 1988.

[SCS+97] HT Schmidt, H Cederquist, R Schuch, L Bagge, and A Kallberg. A design study for an internal gas-jet target for the heavy-ion storage ring cryring. *Hyperfine interactions*, 108(1-3):339–354, 1997.

[SDN+07] M Schulz, M Duerr, B Najjari, R Moshammer, and J Ullrich. Reconciliation of measured fully differential single ionization data with the first born approximation convoluted with elastic scattering. *Physical review. A*, 76(3), 2007.

[SDR10] N Stolterfoht, RD DuBois, and RD Rivarola. *Electron Emission in Heavy Ion-Atom Collisions*. Springer Series on Atomic, Optical, and Plasma Physics. Springer, 2010.

[SEH+88] OH Siegmund, E Everman, J Hull, M Lampton, and JV Vallerga. Soft X-ray and extreme ultraviolet quantum detection efficiency of potassium chloride photocathode layers on microchannel plates. *Applied optics*, 27(20):4323–4330, 1988.

[Sel10] M Sell. Entwicklung, Aufbau und Test eines ortsempfindlichen Teilchendetektors zur Untersuchung von Stößen zwischen Ionen und lasergekühlten Atomen. bachelor thesis, University Heidelberg, 2010.

[SES+87] OH Siegmund, E Everman, J Sokolowski, M Lampton, and JV Vallerga. Ultraviolet quantum detection efficiency of potassium bromide as an opaque photocathode applied to microchannel plates. *Applied optics*, 26(17):3607–3614, 1987.

[SFF+07] M Schulz, D Fischer, T Ferger, R Moshammer, and J Ullrich. Four-particle dalitz plots to visualize atomic break-up processes. *Journal of physics. B, Atomic, molecular and optical physics*, 40(15):3091–3099, 2007.

[SFS+02] HT Schmidt, A Fardi, R Schuch, H Zettergren, SH Schwartz, H Cederquist, L Bagge, H Danared, A Källberg, J Jensen, V Mergel, L Schmidt, H Schmidt-Böcking, and CL Cocke. Double-to-single target ionization ratio for electron capture in fast p-He collisions. *Physical review letters*, 89(16):163201, 2002.

[SJR+05] HT Schmidt, J Jensen, P Reinhed, R Schuch, and K Stochkel. Recoil-ion momentum distributions for transfer ionization in fast proton-He collisions. *Physical review. A*, 72(1), 2005.

[SKM+95] Th Stöhlker, C Kozhuharov, PH Mokler, A Warczak, and F Bosch. Radiative electron-capture studied in relativistic heavy-ion atom collisions. *Physical review. A*, 51(3):2098–2111, 1995.

[SLB+99] Th Stöhlker, T Ludziejewski, F Bosch, RW Dunford, and C Kozhuharov. Angular distribution studies for the time-reversed photoionization process in hydrogenlike uranium: The identification of spin-flip transitions. *Physical review letters*, 82(16):3232–3235, 1999.

[SLEV88] OH Siegmund, M Lampton, DE Everman, and JV Vallerga. Soft X-ray and extreme ultraviolet quantum detection efficiency of potassium bromide photocathode layers on microchannel plates. *Applied optics*, 27(8):1568–1573, 1988.

[SLRH91] OHW Siegmund, M Lampton, R Raffanti, and W Herrick. High-resolution delay-line readouts for microchannel plates. *Nuclear instruments & methods in physics research. Section A, Accelerators, spectrometers, detectors and associated equipment*, 310(1-2):311–316, 1991.

[SMF+03] M Schulz, R Moshammer, D Fischer, H Kollmus, DH Madison, S Jones, and J Ullrich. Three-dimensional imaging of atomic four-body processes. *Nature*, 422(6927):48–50, 2003.

[SMK+99] W Schmitt, R Moshammer, H Kollmus, S Hagmann, and R Mann. Ultra-low energy electrons from fast heavy-ion helium collisions: The target-cusp? *Physica scripta. T*, T80B:335–337, 1999.

[SML+01] Th Stöhlker, X Ma, T Ludziejewski, F Bosch, HF Beyer, O Brinzanescu, RW Dunford, J Eichler, S Hagmann, A Ichihara, C Kozhuharov, A Krmer, D Liesen, PH Mokler, Z Stachura, P Swiat, and A Warczak. Near-threshold photoionization of hydrogenlike uranium studied in ion-atom collisions via the time-reversed process. *Physical review letters*, 86(6):983–986, 2001.

[SMM+01] M Schulz, R Moshammer, DH Madison, RE Olson, and P Marchalant. Triply differential single ionization cross sections in coplanar and non-coplanar geometry for fast heavy ion-atom collisions. *Journal of physics. B, Atomic, molecular and optical physics*, 34(9):L305–L311, 2001.

[SMS+00] M Schulz, R Moshammer, W Schmitt, H Kollmus, and B Feuerstein. Electron correlations observed through intensity interferometry. *Physical review letters*, 84(5):863–866, 2000.

[SS79] R Shakeshaft and L Spruch. Mechanisms for charge-transfer (or for the capture of any light particle) at asymptotically high-impact velocities. *Reviews of modern physics*, 51(2):369–405, 1979.

[SSB+07] Th Stöhlker, U Spillmann, D Banas, HF Beyer, and JC Dousse. A 2D position sensitive germanium detector for spectroscopy and polarimetry of high-energetic X-rays. *Journal of physics. Conference series*, 58(1):411–14, 2007.

[SSG+83] AS Schlachter, JW Stearns, WG Graham, KH Berkner, and RV Pyle. Electron-capture for fast highly charged ions in gas targets - an empirical scaling rule. *Physical review. A*, 27(6):3372–3374, 1983.

[STJJ09] MS Schöffler, JN Titze, T Jahnke, and O Jagutzki. Collision dynamics in electron-capture processes with excitation. *Physical review. A*, 80(4), 2009.

[STJN09] MS Schöffler, J Titze, T Jahnke, and N Neumann. State-selective differential cross sections for single and double electron capture in He(+,2+)-He and p-He collisions. *Physical review. A*, 79(6), 2009.

[Sto30] M Stobbe. The quantum mechanics of photo-electrical processes. *Annalen der Physik*, 7(6):661–715, 1930.

[SVB07] M Schulz, T Vajnai, and JA Brand. Differential double capture cross sections in p plus He collisions. *Physical review. A*, 75(2), 2007.

[SWET10] A Simon, A Warczak, T ElKafrawy, and JA Tanis. Radiative double electron capture in collisions of O8+ ions with carbon. *Physical review letters*, 104(12):123001, 2010.

[SWG+12] M Schulz, X Wang, M Gundmundsson, K Schneider, and A Kelkar. Strongly enhanced backward emission of electrons in transfer and ionization. *Physical review letters*, 108(4), 2012.

[Tho27] LH Thomas. On the capture of electrons by swiftly moving electrified particles. *Proceedings of the Royal Society of London. Series A, Containing papers of a mathematical and physical character*, 114(768):561–576, 1927.

[UDL+91] J Ullrich, R Dörner, S Lencinas, O Jagutzki, and H Schmidt-Böcking. Recoil-ion momentum spectroscopy. *Nuclear instruments & methods in physics research. Section B, Beam interactions with materials and atoms*, 61(4):415–422, 1991.

[UMD+97] J Ullrich, R Moshammer, R Dorner, O Jagutzki, and V Mergel. Recoil-ion momentum spectroscopy. *Journal of physics. B, Atomic, molecular and optical physics*, 30(13):2917–2974, 1997.

[UMD+03] J Ullrich, R Moshammer, A Dorn, R Dorner, and LPH Schmidt. Recoil-ion and electron momentum spectroscopy: reaction-microscopes. *Reports on progress in physics*, 66(9):1463–1545, 2003.

[UMU+95] J Ullrich, R Moshammer, M Unverzagt, W Schmidt, and P Jardin. Ionization collision dynamics in 3.6 MeV/u Ni24+ on He encounters. *Nuclear instruments & methods in physics research. Section B, Beam interactions with materials and atoms*, 98(1-4):375–379, 1995.

[US03] J Ullrich and VP Shevelko. *Many-particle quantum dynamics in atomic and molecular fragmentation*. Springer series on atomic, optical, and plasma physics. Springer, Berlin, 2003.

[USBK88] J Ullrich, H Schmidt-Böcking, and C Kelbch. Determination of very small projectile scattering angles by measuring recoil-ion transverse velocities. *Nuclear instruments & methods in physics research. Section A, Accelerators, spectrometers, detectors and associated equipment*, 268(1):216–224, 1988.

[VK98] AB Voitkiv and AV Koval. Cross sections for hydrogen and helium ionization by impacts of fast highly charged ions. *Journal of physics. B, Atomic, molecular and optical physics*, 31(3):499–513, 1998.

[VMS+91] M VonHellermann, W Mandl, HP Summers, A Boileau, and R Hoekstra. Investigation of thermal and slowing-down alpha-particles on jet using charge-exchange spectroscopy. *Plasma Physics and Controlled Fusion*, 33(14):1805–1824, 1991.

[VNU08] AB Voitkiv, B Najjari, and J Ullrich. Mechanism for electron transfer in fast ion-atomic collisions. *Physical review letters*, 101(22), 2008.

[Voi08] AB Voitkiv. Electron-electron interaction and transfer ionization in fast ion-atom collisions. *Journal of physics. B, Atomic, molecular and optical physics*, 41(19), 2008.

[VSJ+86] H Vogt, R Schuch, E Justiniano, M Schulz, and W Schwab. Experimental test of higher-order electron-capture processes in collisions of fast protons with atomic-hydrogen. *Physical review letters*, 57(18):2256–2259, 1986.

[WAW+93] E Wolfrum, F Aumayr, D Wutte, HP Winter, and E Hintz. Fast lithium-beam spectroscopy of tokamak edge plasmas. *Review of scientific instruments*, 64(8):2285–2292, 1993.

[Wiz79] JL Wiza. Microchannel plate detectors. *Nuclear instruments and methods*, 162(1-3):587–601, 1979.

[WO96] CJ Wood and RE Olson. Three-body collision dynamics for single ionization of helium by protons and antiprotons. *Journal of physics. B, Atomic, molecular and optical physics*, 29(7):L257–L262, 1996.

[WPFB84] MJ Whiteley, JF Pearson, GW Fraser, and MA Barstow. The stability of csi-coated microchannel plate x-ray-detectors. *Nuclear instruments & methods in physics research. Section A, Accelerators, spectrometers, detectors and associated equipment*, 224(1-2):287–297, 1984.

[WSK+11] X Wang, K Schneider, A Kelkar, M Schulz, and B Najjari. Mutual projectile and target ionization in 1-MeV/amu N(4+) and N(5+) + He collisions. *Physical review. A*, 84(2), 2011.

[WSL+12] X Wang, K Schneider, A LaForge, A Kelkar, M Grieser, and R Moshammer. Projectile coherence effects in single ionization of He. 2012. to be published.

Acknowledgements

An dieser Stelle möchte ich mich bei all denen bedanken, ohne die diese Arbeit nicht möglich gewesen wäre. Allen voran danke ich meinem Betreuer Daniel Fischer für die Aufnahme in die Arbeitsgruppe, und für seine Sachkenntnis und Unterstützung. Besonders danke ich auch den Mitgliedern meiner Gruppe, Michael Schulz, Xincheng Wang, Aditiya Kelkar, Renate Hubele und allen anderen.

Ein großer Dank geht an Alexander Voitkiv für die theoretischen Rechnungen und die Geduld. Besonders bedanken möchte ich mich auch bei Manfred Grieser dafür, dass er mir unermüdlich den Speicherring erklärt hat. Bei allen Mitarbeitern am Beschleuniger und am TSR bedanke ich mich für die Möglichkeit, dort Experimente machen zu können. Auch danke ich den Mitarbeitern der Werkstatt und der Elektronik.

Ganz besonders danke ich meinen Bürokollegen und meinen Mit-Doktoranden Cristian Ott, Philipp Raith, Martin Laux, Michael Schuricke, Andreas Kaldun, und so vielen mehr für die gute Stimmung und die schöne Zeit. Ich danke allen Korrekturlesern dieser Arbeit!

Ein herzlicher Dank geht schließlich an meine Familie, meine Freunde und meine Mitbewohner!